Architectured Microstructres

The effect of localised laser treatment on the deformation behaviour of a Fe-Ni-C steel

M.R. van Seumeren



Architectured Microstructres

The effect of localised laser treatment on the deformation behaviour of a Fe-Ni-C steel

by

M.R. van Seumeren

to obtain the degree of Master of Science

at the Delft University of Technology,

to be defended publicly on Friday February 12, 2021 at 12:00 PM.

Student number:	4682963	
Project duration:	February 8, 2020 – February 12, 2021	
Thesis committee:	Dr. J. Hidalgo Garcia,	TU Delft, supervisor
	Prof. dr. M. J. Santofimia,	TU Delft, supervisor, chairwoman
	Dr. V. Popovich,	TU Delft
	K. Sedighiani,	TU Delft, Max-Plank-Institut fur Eisenforschung

An electronic version of this thesis is available at `http://repository.tudelft.nl/`.

TU Delft

Preface & Acknowledgements

This thesis investigates the deformation behaviour of an architectured microstructure created by localised heat treatment of a metastable austenitic steel using experiments and simulations. This work was carried out in fulfilment of the requirements for a Master of Science at Delft University of Technology in the period of February 2020 to February 2021.

This thesis was initiated as a follow up from a previous research started by Javier Hidalgo Garcia about the effect of local laser treatment on the microstructure of steel. Thereafter the project was started under daily supervision of Javier. I would like to thank him for the good discussions, guidance, help with the experiments, feedback and a lot more. His support was of immense value, for which I would like to offer my sincere gratitude. I would also like to thank Maria Santofimia Navarro for her role as supervisor and chairwoman of the Thesis Committee. Her in-depth comments on the thesis helped focussing the story into this final product.

Furthermore, I would like to thank various people at the Material Science laboratories, for the help and advice regarding the experimental procedures and characterization. First of all I would like to thank Jurriaan van Slingerland for helping me with the laser treatment and creating the samples. Secondly I would like to thank Elise Reinton for the help with the DIC and tensile experiments.

Lastly, I would like to thank Richard Huizinga for the help and advice with the computational simulations. His help and knowledge of DAMASK and his optimisation script helped enormous.

M.R. van Seumeren
Delft, February 2021

Abstract

The strength-ductility trade-off has been a long standing dilemma in material science. With the use of laser surface treatments, effort has been made in order to obtain a heterogeneous material with a well defined architectured microstructure to optimize this trade-off. In the present study, it is investigated how the deformation behaviour of Martensite/Austenite steel microstructures in a Fe-25Ni-0.2C alloy can be tailored by the creation of patterned microstructures with localized laser treatment. Due to these treatments strong variations in microstructure are observed. Two different patterns are created (i) a dotted diagonal pattern and (ii) a dotted horizontal pattern which are both evaluated using as-quenched and tempered martensite as base material. The deformation behaviour of the patterned microstructures is investigated using both experiments and simulations.

In the experimental approach characterization of the laser treated specimens is carried out using Optical Microscopy (OM) and micro-hardness measurements. The local deformation of the patterned microstructure is investigated using Digital Image Correlation (DIC). During deformation, strain partitioning is observed in the austenitic areas. In these areas mechanically induced martensitic transformation takes place, influencing the hardening of the material. The phase strength does not seem to influence the austenite stability in the analysed patterns, however it does show difference in hardness of the freshly formed martensite.

For the simulation, Crystal Plasticity Finite Element Modelling (CPFEM) is used to describe the plastic deformation of the patterned material. Both the local and overall behaviour are investigated and validated with the experimentally obtained results. The simulation can serve as a tool to identify patterns which show promising deformation behaviour.

Contents

List of Figures iii

List of Tables vii

1 Motivation and Background 1
1.1 Motivation . . . 1
1.2 State of the art . . . 3
1.2.1 Steel composites . . . 3
1.2.2 Topology design materials . . . 5
1.2.3 Laser treatment for solid state transformations . . . 7
1.2.4 Phases and transformations in Fe-Ni-C steels . . . 8
1.2.5 Reverse austenization . . . 10
1.2.6 Mechanical stability of austenite . . . 12
1.2.7 Tempering of martensite . . . 14
1.2.8 Crystal Plasticity . . . 15

2 Objectives and Structure 17
2.1 Approach by experiments . . . 17
2.2 Approach by simulations . . . 18
2.3 Selection of patterns . . . 18

3 Experimental research 19
3.1 Experimental Procedure . . . 19
3.1.1 Material . . . 19
3.1.2 Pattern creation . . . 19
3.1.3 Microstructural characterisation . . . 22
3.1.4 Mechanical testing . . . 22
3.2 Results . . . 26
3.2.1 Microstructural characterisation of laser treated specimens . . . 26
3.2.2 Hardness at LAZ in non-deformed specimens . . . 29
3.2.3 Overall deformation behaviour in the architectured structures . . . 31
3.2.4 Local deformation behaviour by DIC . . . 34
3.2.5 Mechanical stability of austenite . . . 36
3.2.6 Hardening of different phases . . . 38
3.3 Discussion . . . 39
3.3.1 Microstructure of the laser treated specimen . . . 39
3.3.2 Effect of pattern topology on the deformation . . . 41
3.3.3 Effect of phase strength . . . 44

4 Simulation experiments 47
4.1 Introduction . . . 47

4.2 Crystal plasticity simulations 47
4.2.1 Introduction to DAMASK software 47
4.2.2 Description of the RVE 52
4.2.3 Selection of the model parameters 55
4.2.4 Alternative simulation setups 55
4.3 Results & Discussion 59
4.3.1 Parameter definition 59
4.3.2 Parameter calibration 62
4.3.3 Small scale simulations 63
4.3.4 Large scale simulations 67

5 Comparison between experimental and simulated results 71
5.1 Local deformation 71
5.2 Overall deformation 73
5.3 Conclusion 74

6 Conclusions and Outlook 75

Bibliography 77

Appendices 87

A DIC result of the specimens 89

B Tensile test results of the specimens 93

List of Figures

1.1 Multilayer steel in which a) shows the cross section and b)the classification within the strength-elongation plot [11] 4
1.2 Ideas of composite geometries which can be obtained by decarburization according to B. Chehab et al. [15] 5
1.3 Results of topology optimization of the microstructure in which the material should be reinforced against horizontal stress as well as shear stress. Black: the material with higher stiffness, White: the material with lower stiffness [18] 6
1.4 2D-microstructure topology design for tailored stiffness and thermal conductivity. The value of η_c determines the ductility-conductivity trade-off with $\eta_c = 1.0$ is stiff material with low conductivity [20] 7
1.5 Schematics of laser surface treatment with both melting and solid state transformation [27] 8
1.6 Schematic visualization of a material wit a certain composition, showing the chemical free energy of austenite and martensite as a function of the temperature [38] 9
1.7 Martensite morphologies in Fe-Ni-C steel [98] 10
1.8 The A_s and A_f finish dependence on heating rate and carbon content with a) 0.05C b) 0.3C and c) 0.6C [41] 11
1.9 Schematic figure showing the effect of carbon content on the hardness of martensite and austenite [33] 14

2.1 Different patterns discussed in this thesis a)dotted diagonal pattern , b) dotted horizontal pattern, c) line structure 18

3.1 Equilibrium phase diagram of Fe-25Ni with variable carbon content obtained with Thermocalc [72] 20
3.2 Dimension created pattern by laser treatment a) dotted diagonal pattern b) dotted horizontal pattern 21
3.3 Hardness measurements on the QM sample laser treated on one side 23
3.4 Example of correction of QM/2 without the use of an extensometer with the reference of QM-1 25
3.5 DIC analysis setup 25
3.6 OM image where two main regions in the austenite can be distinguished: (i) fine grained region (ii) coarse grained region 26
3.7 Martensitic structure of the base material 27
3.8 Grain structures within the austenite 27
3.9 Penetration of austenite formation in the laser sample for specimen 1 (a), specimen 2 (b) and specimen 3 (c) according to table 3.2 28
3.10 Interpolated hardness map of QM of the single spot (a) along with the hardness values for the indices graphed (b) 29

3.11 Interpolated hardness map of QM (a) and TM (b) along with the hardness values for the indices graphed (c,d) . . . 30
3.12 True stress- True strain curves of the base material for the individual phases . 32
3.13 True stress- True strain curves of (a) as-quenched martensite specimens and (b) tempered martensite specimens . . . 33
3.14 DIC results of the QM for (a) the dotted diagonal pattern and (b) the dotted horizontal pattern with an overall strain of 0.055 . . . 34
3.15 DIC results of TM for (a) the dotted diagonal pattern and (b) the dotted horizontal pattern . . . 35
3.16 Fracture of the specimens: (a) QM/2, (b) QM-2 and (c) TM/1 . . . 36
3.17 The austenite phase fraction in the laser treated area as a result of (a) the local strain and (b) global strain . . . 36
3.18 OM images of the austenite dot which display martensitic transformation with different local strain values for a) 0, b) 0.042 and c) 0.162 . . . 38
3.19 DIC results of QM-3 at a overall strain of a)0.009, b)0.022 and c)0.055 . . . 42
3.20 Local strain vs. Global strain . . . 46

4.1 Microstructure used for simulating large structures including crystallographic orientations of each grain . . . 53
4.2 RVE for the dotted horizontal pattern (left) and dotted diagonal patter (right) 54
4.3 Scheme of different simulation routes to overcome limitations in the used simulation . . . 57
4.4 Visual interpretation of some parameters in the phenomenological model . . 61
4.5 Stress-strain curves simulated of the base material in comparison with the experimental curves . . . 62
4.6 DIC results line pattern previous research [80] . . . 64
4.7 Stress and strain partitioning simulation line pattern . . . 64
4.8 Stress and strain partitioning behaviour of a line pattern with an over exaggerated hard phase . . . 65
4.9 Stress and strain partitioning behaviour of a dotted horizontal pattern (top) and dotted diagonal pattern (bottom) . . . 66
4.10 Stress and strain partitioning behaviour of QM (a,c,e) and TM (b,d,f) of the patterned line (a,b), dotted diagonal patter (c,d) and dotted horizontal pattern (e,f) . . . 68
4.11 True Stress-True Strain curves from the simulated dotted diagonal and dotted horizontal patterns for both QM and TM along with the stress-strain curves of the base materials . . . 69

5.1 Comparison of local deformation behaviour of (a) the simulated and (b) DIC experimental results . . . 72
5.2 Comparison of the stress-strain curves of the experiments and simulations for both the dotted diagonal and dotted horizontal pattern of QM and TM . . 73

A.1 DIC results QM/1 . . . 89
A.2 DIC results QM/2 . . . 89
A.3 DIC results QM/3 . . . 89
A.4 DIC results QM-1 . . . 89

A.5 DIC results QM-2 89
A.6 DIC results QM-3 89
A.7 DIC results QM-4 90
A.8 DIC results TM/1 90
A.9 DIC results TM/2 90
A.10 DIC results TM/3 90
A.11 DIC results TM-1 90
A.12 DIC results TM-2 90
A.13 DIC results TM-3 91
A.14 DIC results TM-4 91

B.1 Tensile curves of all specimens 93

List of Tables

3.1 Composition of the alloy 19
3.2 Laser parameters for penetration tests 22
3.3 QM tensile specimens with corresponding maximum strain values 24
3.4 TM tensile specimens with corresponding maximum strain values 24
3.5 Microstructural features for the different specimens 28
3.6 Microhardness values of the individual phases for different specimens 39

4.1 Geometry file variables 48
4.2 Material file sections and variables 50
4.3 Simulation parameters for phenomenological model 56
4.4 Simulation parameters for QM, TM and austenite 60

1. Motivation and Background

1.1. Motivation

Generally, structural materials require high strength to sustain a desired shape and high ductility for easy forming. Additionally, a good combination of strength and ductility reflects their toughness which defines the energy the material can absorb upon deformation. Unfortunately, these properties are considered mutually exclusive: an increase in strength is inevitably accompanied by a sacrifice in ductility, resulting in a strength-ductility trade-off [1]. This trade-off has been a long standing dilemma in materials science. It has limited the potential of many structural materials, with steels in particular.

One of the approaches to overcome this challenge is the creation materials with heterogeneous microstructures, in which the size and geometry of the microstructural domains may vary widely. Microstructure heterogeneity can manifest by differences in grain sizes, textures, phases and composition, which creates microstructure domains with marked differences in properties [2]. These differences lead to deformation incompatibilities that cause high local elastic and plastic strain gradients resulting in the partitioning of stress and strain. In return, the mechanical performance of the material greatly improves. This microstructure design principle applies to Advanced High Strength Steels (AHSS) with multiple phase microstructures in which composition and phase mixture are carefully selected in order to achieve a range of strength, ductility and toughness properties.

The combination of a soft and a hard phases generally found in AHSS steels helps improving both the strength and ductility of the material. An example of these materials are Dual Phase (DP) steels [3] in which the soft ferrite phase was combined with the hard martensite phase. Even more interesting is the exploitation of producing an unstable combination of non-equilibrium phases such as martensite, bainite and austenite [4] for example Quenching & Partitioning (Q&P) steels [5] in which the soft austenite phase was combined with the hard martensite phase. These steels show great enhancement in the strain hardening of the material increasing their toughness significantly by making use of the mechanically induced transformation of the metastable austenite.

Another way to simultaneously improve strength and ductility, is by the creation of materials with topology designed periodical lattice structures [6]. These materials can combine multiple materials in different configurations and geometries in order to achieve desired properties. A prominent example are composites such as Fibre-Reinforced Plastics (FRP) which enhance the stiffness and strength of the plastic by addition of fibres, and the Sandwich structure composite which combine stiff faces with a light weight core in order to

achieve high flexural stiffness and strength. Topology design computational models are commonly used to get an optimal material distribution in order to improve the desired properties in the material. The outcomes of the models are material constituents distributions that are often in the form of hierarchical periodical structures.

The question arises if it is possible to combine heterogeneous and topology design strategies in order to obtain unique properties regarding the strength and ductility of the material. Hence, creating a material where the heterogeneity within the microstructure of the material can be applied within a hierarchical periodical structure, in particular by the combination of the martensitic and austenitic phases. This can result in enhanced hardening behaviour due to an optimal stress-strain partitioning and the contribution of the mechanically induced transformation within the metastable austenite[8]. Two main challenges arise during the development of this type of materials: (i) the creation of the microstructure and (ii) the understanding of the effect of the topology and phase composition of the microstructure on the mechanical behaviour of the material.

Austenitic metastable steels are interesting candidates to develop martensite/austenite patterned microstructures. In a previous wok it was demonstrated that patterned microstructures can be created in a Fe-Ni-C austenitic steel. First a fully martensitic microstructure was formed by cryogenic treatment. This microstructure was reverted by controlled laser treatments, which enables the occurrence of highly localized solid state transformation including martensite to austenite and tempering of martensite. Temperature and heating rate gradients results in a gradient microstructure with well defined domains at the microscale. However, effect of these combinations of different microstructure domains on the strength and ductility of these materials is not well understood other than the strength ratio between different phases plays a significant role in the development of local strain gradients during plastic deformation.

In order to fully understand the effect of the architectured microstructure on the deformation behaviour of the steel it is important to understand the role of topology, composition and strength on the stess/strain partitioning, hardening of different phases and austenite stability of the material. This objective can be achieved by two approaches: (i) experimentally or (ii) with the use of computational tools. The local deformation of steel phases can be experimentally investigated with the use of Digital Image Correlation (DIC), microhardness testing, Optical Microscopy (OM), X-ray Diffraction (XRD) and tensile testing. In order to speed up the design process, computational material simulations are often implemented. The goal of the computational material design is to apply the best scientific understanding to facilitate decisions regarding the optimal trade-offs that meet desired needs in the most time and resource efficient manner [9]. However the use of simulations is often accompanied by limitations due to simplifications made in the model, which makes it necessary to perform an experimental study along with it to verify the correctness of the assumptions made.

1.2. State of the art

In this section current academical advancements which can help identify observations made in this research are discussed. Fully steel composites and their effect on the properties of the material are discussed first. Next, the effects of different topologies on the behaviour of a composite material are discussed which will be the basis of pattern selection in this research. A general background on laser surface treatment is provided since it causes the solid state transformation of the Fe-Ni-C alloy object of study. Furthermore, relevant phase transformations in Fe-Ni-C steels are explained such as reverse austenization, the mechanically induced transformation and the tempering of martensite.

1.2.1. Steel composites

For centuries steel is used as a structural material in which a wide range of strength and ductility can be achieved by means of alloying or applying heat treatments. However, increasing the strength of the steel in many cases reduces the ductility and vice versa. In order to improve both properties of steels it is possible to use steel composites. Two main types of steel composites can be distinguished: (i) fully steel composites, in which the mechanical contrast between the constituent phases gives rise to composite behaviour, and (ii) steel-based multi-material composites [10]. Steel composites can function on different scales from millimetres to nanometres resulting in composites on the macroscopic and microscopic scale.

Damascus steels are often seen as the foundation and template for steel composites and were developed in the Middle East around A.D. 540. Damascus steels are ultra high carbon steels in which the distinct surface patterns result from a carbide banding phenomena produced by micro-segregation of minor amounts of carbide forming elements [12]. To be more precise, the pattern observed in Damascus steel is produced by the formation of aligned sheets of clustered cementite particles separated by sheets of pearlite [13]. This gave the steel unique properties since normally the higher carbon steels tend to be more brittle. Creating damascus steels could yield a strain to fracture of 10% while obtaining a tensile strength of 1068 MPa. This is therefore a good example of a steel in which the microstructure tailored in a certain pattern improves the desired mechanical properties.

Another example of a fully steel composite is given by T. Koseki et al. [11] which made a laminate structure by making use of hot roll-bonding of Type 304 austenite and Type 420 martensite, in which martensite functions as the hard phase and austenite as the soft in order to improve the strength as well as the ductility. These so called multilayer steels are shown in figure 1.1 as well as their classification in the strength elongation plot. With the use of in-situ neutron diffraction measurements in the research it is stated that stress is partitioned in both brittle and ductile layers. The martensitic layer deforms elastically bearing an increased portion of the applied stress, while the austenite yields at 400 MPa after which it starts to bear a larger fraction of the applied stress due to work hardening. Compared

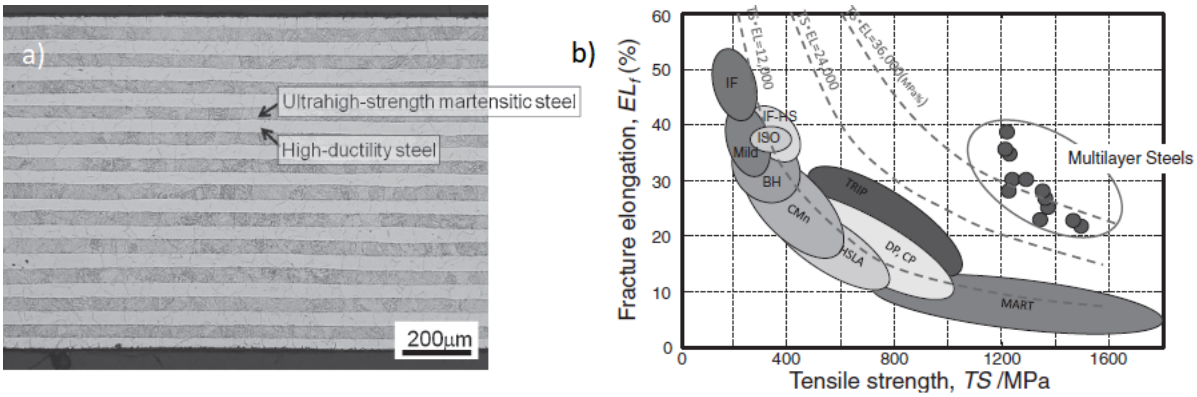


Figure 1.1: Multilayer steel in which a) shows the cross section and b)the classification within the strength-elongation plot [11]

with monolithic steels, these multilayer steels exhibit improved strength and deformation behaviour. Although these results seem very promising, two limitations should also be considered regarding this steel composite:

- In these materials the strength comes initially from the martensitic bands, but this is considering the structure is uni-directionally loaded parallel to the formed bands. Loading this structure in different directions introducing more shear can cause the material to behave differently and less ideally. Therefore these structures are limited in implementation.

- The producing of these structures using roll-bonding is rather complex and time/cost intensive. An example of this is in order to prevent carbon diffusion across the layers a thin layer of nickel need to be added between every layer. This won't be feasible for large scale production due to time and cost of the production.

Another way to create steels with architectured phases is described by O. Bouaziz et al. [14] and B. Chehab et al. [15] who suggest an approach to increase the strength as well as the elongation by means of creating so called Compositionally Graded Materials (CGMs). They both use a relatively cheap process by locally addition or removal of carbon via (de)carburizing atmospheres. Since carbon atoms are interstitial atoms this diffusional process can be commercially viable. In order to remove carbon without oxidizing the steel a H_2/H_2O mixture is used as decarburization gas. A ferrite layer forms at the surface and can grow into the austenite core. The depth of growth is controlled by the duration of the heat-treatment as well as by the carbon concentration. Upon quenching, a ferrite-martensite structure forms consisting of a soft and a hard phase for optimal mechanical properties.

An example of CGM geometries proposed by B. Chehab et al. [15] is displayed in figure 1.2. R. Roumina et al. [16] showed improved fracture strength and strain of a graded 300M steel compared to the homogeneous martensitic steels with the use of this method. Similar improvements are obtained by F. Lefevre-Schlick et al [17] which used a AISI 1070 steel. The problem with this approach is that although the (de)carburization process may be relatively cheap, for the more complex structures as are shown in Figure 1.2 extrinsic masks are necessary which protect the base material with the use of a Cu layer. The difficulty is

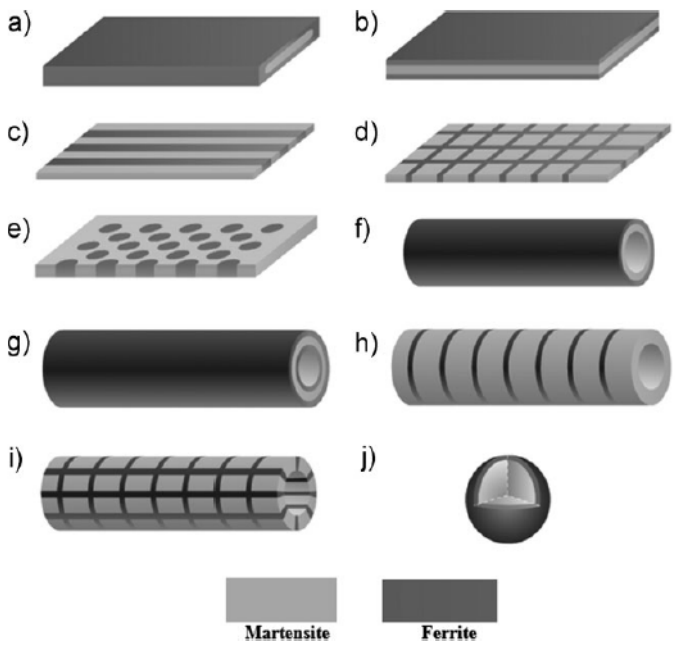


Figure 1.2: Ideas of composite geometries which can be obtained by decarburization according to B. Chehab et al. [15]

in applying and removing this mask without damaging the base material and therefore this technology is thought to be very complicated and costly but does provide very accurately defined patters [14].

1.2.2. Topology design materials

The mechanical behaviour of composite materials mainly depends on the geometrical properties of the microstructure, in which the non-linear plastic regime of the material can be considerably extended. The distribution of the materials as well as their shape and size are the main parameters controlling this behaviour [18]. Hence, in order to achieve a strong, tough or stiff material, the microstructural topology should be optimized. This can be effectively done by making use of computational models. Topology optimization transforms a problem of structural design into one of optimal material distribution in order to satisfy the demands of the design [19]. The optimization of the topology is also very dependent on the load condition of the structure due to the created stress fields and the anisotropy of most microstructures.

J. Kato et al. [18] showed that to optimize the topology in order to increase the stiffness of the material, the microstructure should consist of thick layers of stiffer material to be reinforced for the horizontal stresses. Diagonal reinforcement should be placed for shear stresses. This can be seen in figure 1.3 where the black material is the material with higher stiffness and the white is the material with lower stiffness.

N. de Kruijf et al. [20] studied the optimal topology while taking in consideration both the maximal conduction of the structure as well as the stiffness by using the Solid Isotropic Material with Penalization (SIMP) method, and found an optimum for both cases. The load

case is a fixed plate loaded at one end while fixed in the other. In the research the volume fraction of the phase with high stiffness and low conductivity is kept constant. The results of the microstructures can be seen in figure 1.4 where the blue colour is the stiff material with low conductivity and red is the material with low stiffness and high conductivity. $\eta_c = 1.0$ shows the case where only stiffness is taken in consideration in which a circular pattern of the low stiffness material is developed. This result is similar to the microstructure obtained by B. Xu et al. [21] using this similar SIMP method and load case.

X. Yan et al. [22] and J. Gao et al. [23] both improved the mechanical properties of the material while keeping a as low as possible weight fraction, to lower the overall density of the structure. They used Bi-directional Evolutionary Structural Optimization (BESO) and Energy Based Homogenization Method (EBHM) respectively to improve both the macro- and micro- structure of the material. Different complex shapes resulted from the simulations dependent on the initial microstructure and the load case.

Instead of obtaining a stiff material Z. Jia et al. [24] created different composite structures in order to optimize the strength and toughness. The best results for structural components was a layered lamellar structure where a hard and soft phase alternate. By using this structure they showed that an increase of 5 % in strength is possible while the toughness increases by sevenfold compared to the hard phase.

In summary, a dotted topology in which the dots are the softer phase, help increase the stiffness of the material. Whereas a layered lamellar structure is shown to increase the strength and ductility of the material and hence the toughness. However, it is important to notice that a dotted structure is an isotropic structure whereas the lamellar structure is not and has to be integrated correctly in the design in order to be exploited.

The use of topology design is shown to help determine the optimal shape for the material in order to utilize desired properties. However the producibility of the shape is often a limitation with the creation of the optimized topology. Therefore the optimization of topology is often done with computer simulations and theoretical approaches. In order for a topology design to be implemented a compromise between optimal topology, producibility and cost need to be found to determine the ideal implementation of topology design.

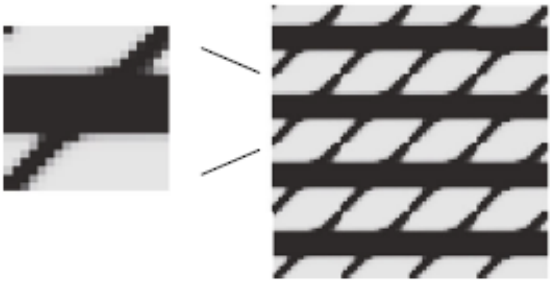


Figure 1.3: Results of topology optimization of the microstructure in which the material should be reinforced against horizontal stress as well as shear stress. Black: the material with higher stiffness, White: the material with lower stiffness [18]

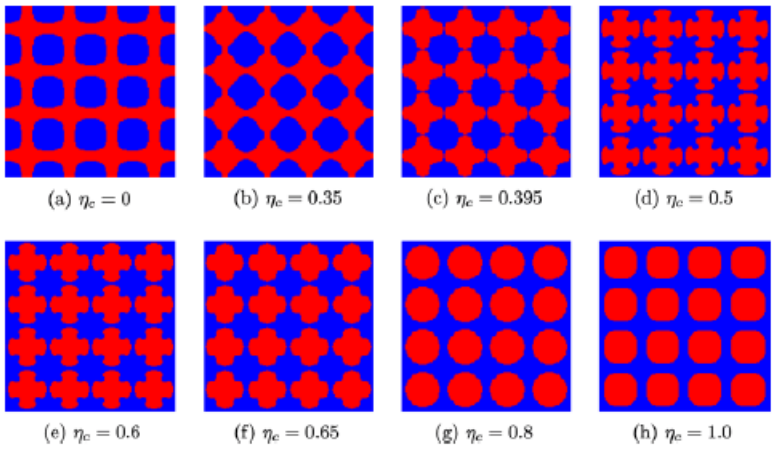


Figure 1.4: 2D-microstructure topology design for tailored stiffness and thermal conductivity. The value of η_c determines the ductility-conductivity trade-off with $\eta_c = 1.0$ is stiff material with low conductivity [20]

1.2.3. Laser treatment for solid state transformations

Laser treatment is vastly used in surface engineering because of the advantages over conventional surface treatment methods such as an increase in precision, fast processing and localized treatments. The treatment involves solid heating and phase change at the irradiated surface [25]. The initial goal of the laser heat treatment was selective surface hardening for wear reduction, however it is now also used to change metallurgical and mechanical properties [26]. During laser heat treatment the power distribution should give a uniform temperature over the area to be treated in order for well defined phase transformation. Several methods can be used in order to spread the laser beam such as defocusing, kaleidoscopes, segmented mirrors and special optics [26].

The laser surface treatment is schematically displayed in Figure 1.5 according to [27]. The treatment involves absorption of energy at the surface supplied by the laser. This heat can result in two main processes:

- non-melting laser treatment: The peak temperature caused by the laser does not exceed the melting temperature of the material. This causes temperature fields which are governed by the heat conduction in the bulk. Limited depth is achieved by this treatment causing microstructural changes due to solid state tranformation only at the surface of the material. Examples of these treatmens include transformation hardening and annealing [28] and local softening for improved formability [29].

- melting laser treatment: The laser does exceed the melting temperature of the material, the molten material transfer heat by both convection as well as conduction. Examples of this treatment are laser welding [30] and laser cladding [31] at which material is added in order to create surface layers with a different chemical composition, this process allows for design at microstructural level caused by the small localized fusion [31].

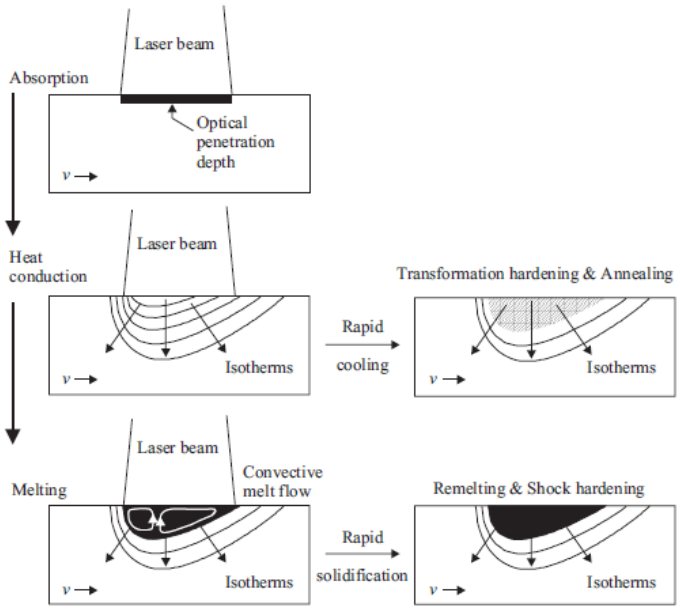


Figure 1.5: Schematics of laser surface treatment with both melting and solid state transformation [27]

1.2.4. Phases and transformations in Fe-Ni-C steels

Fe-Ni-C steels exhibit austenite at ambient temperature, and can be fully transformed in martensite by cryogenic treatment or as a result of the application of strain [32]. A detailed description of Fe-Ni-C microstructures is described next.

Austenite

Austenite is a Face Centred Cubic (FCC) phase in steel which is at equilibrium at temperatures above 727°C in the Iron-Carbon binary systems [33]. However by addition of austenite stabilizing elements such as Ni, Mn, and C, the phase can be made stable at ambient temperatures. The high addition of nickel causes the (meta)stability of austenite at ambient temperatures in Fe-Ni-C steels [34, 35]. In comparison to the martensite, the austenite is considered as the soft phase which provides formability. The TRIP effect can also take place within the austenite which gives additional strength and ductility by the formation of martensite under stress.

Martensite

Martensite is a Body Centred Cubic (BBC) or Body Centred Tetragonal (BCT) phase in steel, dependent on the carbon content. The martensitic phase transformation is a diffusionless phase transition with cooperative, homogeneous and crystallographically orientated movement of large groups of atoms [36]. The transformation from austenite into martensite happens through nucleation and growth since it is a first-order phase transition. Preferred nucleation sites of the martensite are lattice defects of the austenite phase. Because of the different specific volumes of both martensite and austenite, a significant lattice stress arises during the transformation. These lattice stresses are compensated by lattice invari-

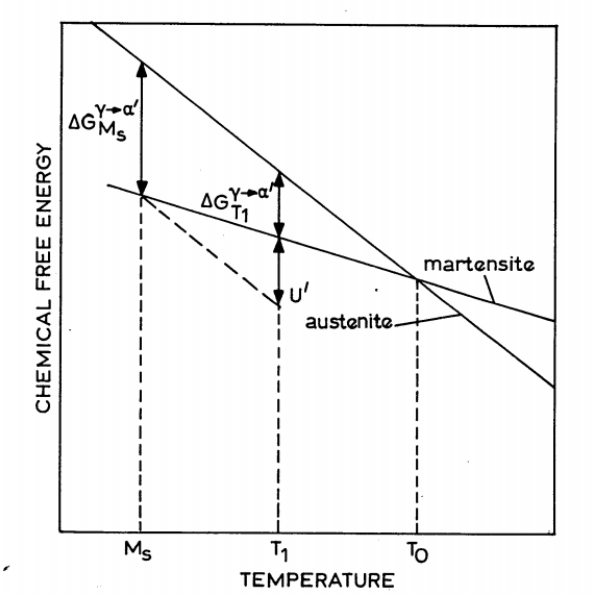


Figure 1.6: Schematic visualization of a material wit a certain composition, showing the chemical free energy of austenite and martensite as a function of the temperature [38]

ant deformation which can be the formation of lattice defects, dislocation glide and mechanical twinning [37]. A strong relation between the orientation of austenite and martensite exist. The three most common orienation relationships (ORs) are the Bain, Kurdjumov-Sachs (KS) and Nishiyama-Wassermann (NW) [37]. Due to these orientation relationships the martensite phase transformation can be fully reversible when there is a small difference in lattice constants and specific volumes between the initial and martensitic phase. This is known as the shape memory effect.

The nucleation and growth of martensite is triggered by the difference in Gibbs free energy between the phases. The equilibrium temperature (T_0) determines the temperature in which the chemical free energy of both phases is equal. If $T < T_0$ the free energy of martensite is lower than the austenite hence creating a driving force for diffusionless phase transformation as can be seen in figure 1.6. $\Delta G_{Ms}^{\gamma\to\alpha'}$ is the critical driving force needed for the start of the martensitic transformation. The temperature of undercooling needed for this critical driving force is called the martensitic start temperature (M_s) [38]. However it is possible for the martensitic transformation to occur at higher temperatures when a mechanical stress is applied. The mechanical driving force U' is added to the chemical driving force and the sum should be equal to $\Delta G_{Ms}^{\gamma\to\alpha'}$ in order for the martensitic transformation to happen as can be seen at T_1 in figure 1.6. U' is therefore the critical mechanical driving force necessary for the mechanical-induced martensitic transformation with a corresponding temperature which is refered to as M_s^σ. When the stress is increased beyond the critical

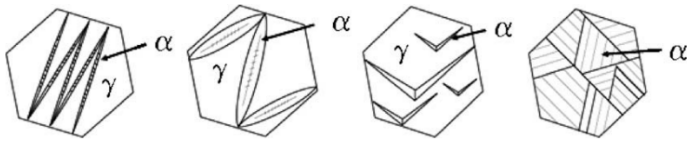
Martensite type	Plate	Lenticular	Butterfly	Lath
Shape				
Ni concentration in Fe–Ni alloy	High ◄			► Low
Formation temperature	Low ◄			► High
Substructure	Twins	Twins + dislocations	Twins + dislocations	Dislocations
Crystal orientation relationship	G–T	G–T, N–W or K–S	K–S or N–W	K–S
Habit plane	$\{3\ 10\ 15\}_\gamma$	$\{3\ 10\ 15\}_\gamma$ or $\{2\ 5\ 9\}_\gamma$	$\{2\ 2\ 5\}_\gamma$	$\{5\ 5\ 7\}_\gamma$ or $\{1\ 1\ 1\}_\gamma$

Figure 1.7: Martensite morphologies in Fe-Ni-C steel [98]

stress, the amount of martensite transformed is increased which is the same effect as the increase in martensite formation with an increased undercooling.

In Fe-Ni-C the martensite can have different morphologies dependent on the alloying content (Ni in particular) and formation temperature as described by Sato et al [98]. The different morphologies are shown in Figure 1.7. Each morphology exhibits difference in the crystallography of the transformation and has a substructure of dislocation, twins or a combination of both.

1.2.5. Reverse austenization

Martensite can further transform back to austenite upon reheating which is known as reverse austenization and is refered to as the γ-α-γ transformation. It is well known that the γ-α transformation results in 24 different orientations of α-martensite in each austenite grain of metastable Fe-Ni. When applying the reversed α-γ transformation, 24 orientations of austenite within a α-martensite grain can be obtained. This results in a possibility of $24^2 = 576$ orientations in a single grain with the γ-α-γ transformation [43]. Therefore this treatment can be used to refine the grain size, even to nanocrystaline size. However, several studies showed that the cooling and heating rate have a large influence. With medium to high cooling and heating rates initial orientations could be obtained instead of different orientations.

Shirazi et al [40] defined that there are two main mechanisms for reverse transformation which are dependent on the chemical composition and the heat treatment conditions: (i) thermally activated diffusional process and (ii) athermal displacive or martensitic process.

Diffusional reversion gives rise to austenite grains with low dislocation density and takes place at slower heating rates. The effect of the heating rate and carbon concentration of a Fe-Ni-C alloy on the transformation mechanism is well described in a paper written by Apple et al [41]. For the reverse transformation to austenite, an austenite start temperature A_s and an austenite finish temperature A_f is defined which are comparable to the A_{c1} and A_{c3} respectively for Fe-C alloys [42]. An example of the dependence of both the A_s and the

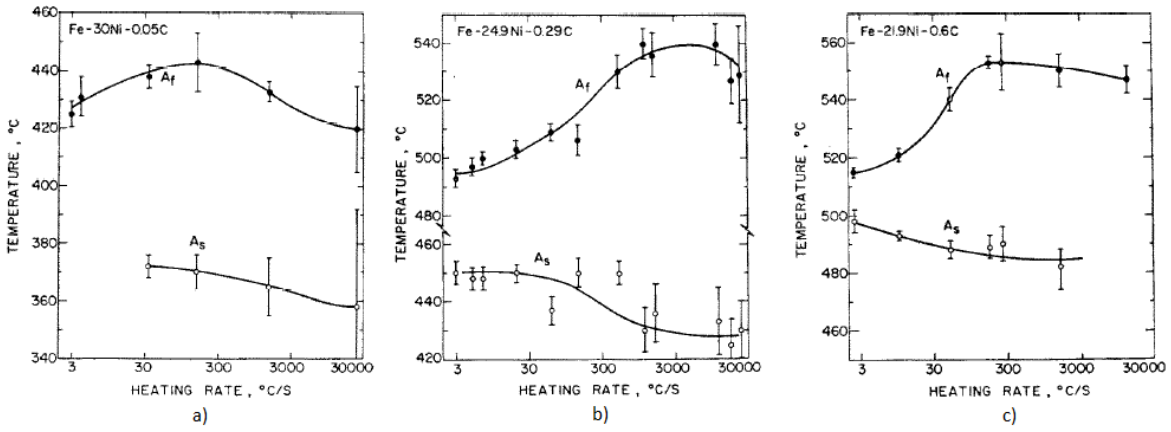


Figure 1.8: The A_s and A_f finish dependence on heating rate and carbon content with a) 0.05C b) 0.3C and c) 0.6C [41]

A_f on the heating rate can be seen in figure 1.8. In which the maximum of A_f is considered as a turning point for the diffusional to the displacive transformation process [41].

In contrast with diffusional reversion, displacive reversion produces austenite grains with high dislocation density and takes place at higher heating rates. With a sufficiently lower austenite start temperature A_s the diffusional reversion is suppressed. Since Ni is an austenite stabilizer it reduces the A_s temperature with increased content and therefore promotes the displacive reversion [40].

Sagaradze et al [43] used a maraging Fe-Ni based metastable austenite alloy to show that by fast cooling and heating (cooling in liquid nitrogen and heating with a rate of 150 K min^{-1}) it was possible to recover the orientation of the initial austenite. The γ-α-γ transformation caused a large increase in dislocation density in the austenite compared to the initial austenite phase. This is caused by three phenomena:

- The partial inheritance of dislocations from the α-martensite phase. The main dislocations in BCC-martensite have a Burgers vector of $\frac{1}{2}\langle 111\rangle_\alpha$, these dislocations become mobile dislocations $\frac{1}{2}\langle 110\rangle_\gamma$ well known in the FCC phase. However of all the slip, only four planes of the $\{110\}_\alpha$ become slip planes of the $\{111\}_\gamma$ during the transformation. This leads to all the other slip planes to turn in to normal planes where no slip occurs. For this reason screw dislocations of the type $\langle 111\rangle_\alpha$ in the plane $\{110\}_\alpha$ and $\{112\}_\alpha$ become immobile when they are inherited by the formed FCC phase which leads to additional strengthening of the austenite.

- The generation of new dislocation during the α-γ transformation which increases the dislocation density causing hardening of the material.

- The formation of a plate subgrain structure resulting from an incomplete reversibility of the transformations. The unrecovered plates which are formed with a different crystallographic orientation than the initial austenite causes a misorientation between the plates and the rest of the austenite results in hardening behaviour.

It was also shown in Sagaradze et al [43] that when using low heating rates (0.2 - 0.4 K min^{-1}) the α-γ transformation results in nano-crystals and hence do not have the same orientation as the initial austenite. It is therefore showed that the cooling and heating rate is of great importance for the reversibility of austenite.

Krauss et al [44] used a iron-33.5% Ni alloy to confirm that after reversal of the martensitic transformation the strength of the austenite increased significantly compared with the annealed austenite. According to him this is a consequence of the of the increase in dislocation density as well as the change of dislocation structure. In the annealed austenite the dislocation structure is relatively uncomplicated with dislocations which tend to be either straight or gently curved. While the austenite which is formed by reversed austenization contains high concentrations of tangled and jogged dislocation with dispersed loops. Also this author found that 'reversal twins' where formed, these twins also contain high concentrations of imperfections which contribute to the strengthening of the material.

1.2.6. Mechanical stability of austenite

A mechanisms which gives austenitic steel a significant enhancement of both strength and ductility through martensitic transformation during plastic deformation is called the Transformation-Induced-Plasticity (TRIP) effect. The transformation of austenite to martensite during deformation at, or close to, room temperature develops a carbon rich martensite phase, which substantially raises the strain-hardening rate and strengthens the material effectively [45]. The increasing strain-hardening rate causes the necking behaviour to occur at higher overall strains since a neck can only develop when there is more strain inside the neck than outside the neck. A higher strain rate requires more stress, hence dampens the strain rate difference and hinders the formation of the neck. Due to equilibrium of force, the region outside the neck is forced to deform as well as to harden to the stress needed, thus stabilizing the material and delaying necking [46].

In order to contribute to the increasing strength and ductility of the material, the austenite to martensite transformation need to happen within the plastic region of deformation. The stability of austenite determines at which point the transformation takes place. The transformation stability of austenite is affected by: the local carbon content in austenite [47, 48, 53, 54], the grain size [49, 52], the morphology [51, 52], the crystallographic orientation of the austenite with respect to the loading direction [53] and the constraining effect of phases surrounding the austenite [50]. Each of those factors is discussed briefly.

- The local composition in the austenite determines the chemical driving force for the transformation of retained austenite to martensite through its influence on the lattice parameter [52, 55, 56]. Elements such as Carbon, Manganese, Nitrogen and Nickel tend to stabilize austenite. In this research nickel plays an important role besides carbon since the material used for reversed austenization is a nickel based steel. The elemental content in austenite should be controlled carefully. Timokhina et al. [52] mentions that at low carbon content the austenite transforms to martensite more rapidly during plastic straining and does not contribute to an increase in elongation,

whereas high carbon contents result in incomplete transformation and also does not lead to an increase in elongation. This shows that the austenite stabilizing alloying elements have a large influence on the transformation behaviour.

- The grain size also has a severe effect on the stability of austenite. Smaller grain sizes causes more grain boundary surface which hinder dislocation movement and increase the strength of the steel according to the Hall-Petch relation [58, 59]. This increase in strength is also translated in an increase in austenite stability. The grain size also affects carbon diffusion and heterogeneities of elements in the big grains which in their turn control the stability. In TRIP steels the relatively slow carbon diffusion in austenite [57] cause larger grains to not fully partition the carbon among the grain therefore decreasing the stability of the austenite [60]. Grains which are too large (which depends on the material) therefore do not contribute to the increase in elongation and transform to martensite in early stages of the deformation. The grain size of austenite is determined by austenization time and temperature, and the activation of recovery and recrystallization mechanisms, which can also be in influence by heating rates.
- The effect of the morphology of the austenite grain is described by Xiong [51]. In the research it was shown that blocky austenite transformed to twin martensite at a much lower strain (2%) in comparison to film-like austenite (12%). The reason proposed for this result was the film-like austenite had a higher hydrostatic pressure exerted on itself, which was induced by the residual stress. This pressure could suppress the martensitic transformation as the process requires volume expansion.

- The crystallographic orientation of the austenite with respect to the loading direction has an influence on the stability of austenite. The martensitic transformation is described as a shear component in combination with an uni-axial tension (or compression) normal to its habit plane, and since the shear stress is maximal at 45°with respect to the loading direction, grains with their longest axis in this direction transform first. The austenite grains perpendicular to the tensile direction also transform at relatively high rate since the tensile stress component act along the longest axis of the largest possible cross-section, thereby resulting in the highest total tensile force [47]. R. Lehnert [54] showed that ϵ-martensite deformation takes place on the slip planes with the highest Schmid value calculated as followed:

$$m = cos(\phi)cos(\lambda) \tag{1.1}$$

  Where ϕ is the angle of the vector normal to the glide plane and the loading directions and λ is the angle of the glide direction with respect to the loading direction.

- The effect of constraining effect of phases surrounding the austenite. Due to the presence of martensite surrounding the austenite, there is a change in partitioning of the strain. Jacques et al. [61] explained with the help of Boa et al. [62] that a stronger matrix leads to a smaller mean-stress level within the austenite grains, and therefore increases the stability of the austenite and postpone the martensitic transformation. The strengthening of the matrix by martensite causes therefore a 'shielding'

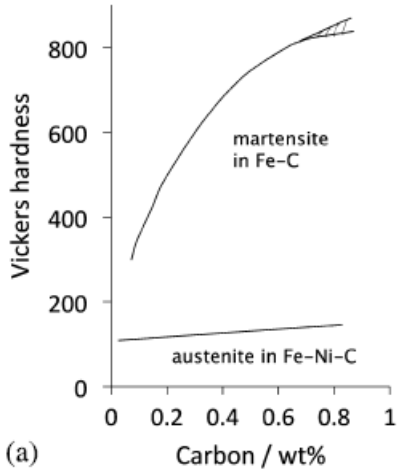


Figure 1.9: Schematic figure showing the effect of carbon content on the hardness of martensite and austenite [33]

effect that decreases the austenite transformation rate. Hidalgo et al. [50] showed that with tempered martensite with a lower yield strength, the austenite is less stable than with martensite with a higher yield strength. It is suggested that the distribution of dislocations in the martensite surrounding the austenite determines the ability of martensite to plastically deform to accommodate the volume expansion caused by the austentite to martensite transformation.

1.2.7. Tempering of martensite

Quenched martensite is characterized by its high strength, but also by its low toughness. This low toughness is the result of the lattice distortion caused by carbon atoms trapped in the octahedral sites of martensite, impurity atom segregation at austenite grain boundaries, carbide formation during quenching, and residual stress produced during quenching [63]. Tempering is a heat treatment which increases the toughness at the cost of losing strength. Before tempering martensite is unstable due to the supersaturation of carbon atoms in the bct crystal lattice, the strain energy associated with the fine dislocation structure, and the interfacial energy associated with the high density of lath or plate boundaries. The supersaturation of carbon provides the driving force for carbide formation, the high strain energy for recovery and the high interfacial energy for grain growth [63].

Due to the high dislocation density in the quenched martensite, sites are created for carbon atoms to segregate to, which also increase the driving force for carbide precipitation [64]. Precipitation of carbides causes a decrease in carbon content within the martensite leading to less lattice distortion and a decrease in the hardness of the martensite (Figure 1.9). Due to reduced stresses caused by the decrease in lattice distortion, dislocation glide is easier therefore the formability of the martensite increases, hence increasing the toughness.

The first stage of tempering in Fe-C martensites involves the precipitation of a transition carbide, which is typically in the range of 100°C and 250°C [65]. The formation of these carbides in Fe-Ni-C results in stress relief due to shape changes caused by the internal accommodation mechanism to achieve invariant plane strain [66]. Both Taylor et al. [66] and Kim et al. [67] take into account the possibility of spinodal decomposition (splitting the ferritic phase into a high and low carbon component) to occur prior the precipitation of transition carbides. This would increase favourable shape strain which relates to the high- and low-carbon bands, together with the associated interfacial energy, to aid the nucleation process of carbon precipitation[66]. The higher stages of tempering have to do with the transformation of the (retained) austenite into other phases, however high addition of austenite stabilizing elements delay the temperature at which this effect is observed.

1.2.8. Crystal Plasticity

Crystal plasticity is a continuum-based variational formulation for describing the elastic-plastic deformation of anisotropic heterogeneous crystalline matter. These approaches are important both for basic microstructure-based mechanical predictions as well as for engineering design and performance simulations involving anisotropic media [68].

Crystal plasticity phenomena can be directly linked with non-linear variational formulations. This provides a direct means for updating local crystallographic and hardening state of a material via integration of the evolution of equations for the crystal lattice orientation and the critical resolved shear stress [69]. A crystal plasticity model determines the plastic deformation at each integration point with the use of crystallographic slip and with the use of the rotation of the crystal lattice during deformation. Crystal plasticity uses normally space and time as independent variables and crystal orientation and accumulated slip as dependent variables [70].

Crystal plasticity is highly recommended for multiphase textured steels since it bridges the gap between polycrystalline texture and macroscopic mechanical properties. Multiple models with different constitutive laws can be used to increase the complexity of the simulation and hence take into account extra microstructural phenomena such as the TRIP mechanism [71]. Therefore it allows for optimization between computational speed and accuracy.

2. Objectives and Structure

Literature showed efforts made in order to obtain superior material properties by using heterogeneous material with a well defined architectured microstructure. This can result in a more advanced combination of both fracture elongation and tensile strength, in particular if there is a combination of austenite and martensite. With these aspects in mind, the main objective of this research is to investigate how the deformation behaviour of Martensite/Austenite steel microstructures in Fe-Ni-C alloys can be tailored by the creation of patterned microstructures with localized laser treatment. To answer this objective two different approaches have been considered: (i) experiments and (ii) simulations. Both are discussed in separate chapters after which their outcome is compared and evaluated.

2.1. Approach by experiments

This approach is focused first on creating a microstructure consisting of an austenitic phased pattern in a martensitic matrix. The austenite is considered as the soft phase with additional strengthening mechanism described as the TRIP-effect, whereas martensite is the hard phase which gives the steel the desired strength. The martensitic phase is created with the use of a cryogenic treatment on the metastable austenite phase, after which the patterned microstructure is created by means of localized laser treatment which causes solid state transformation of the martensite into austenite. In order to have metastable austenite at room temperature a Fe-25Ni-0.2C steel is used. Laser parameters are optimized to achieve full penetration through the thickness of the specimens.

Experimental techniques such as optical microscopy (OM), microhardness tests and phase analysis software are used to characterize the microstructural changes obtained by the material due to the local heat treatment, such as grain size, recrystallization, decarburization, grain boundary shape etc.

Digital Image Correlation (DIC) experiments are used to further clarify the deformation behaviour of individual phases experienced by the material during loading. The effects of the different patterns on this local deformation is further investigated. The TRIP-effect is expected to take place in the austenite and the influence of local deformation, tempering, and the microstructural features is examined. Investigating the microhardness of individual phases further identify the effect of the deformation on the mechanical behaviour of the steel. Finally the stress-strain response of each architectured microstructure is analysed and compared to the stress-strain response of the base material. With these results

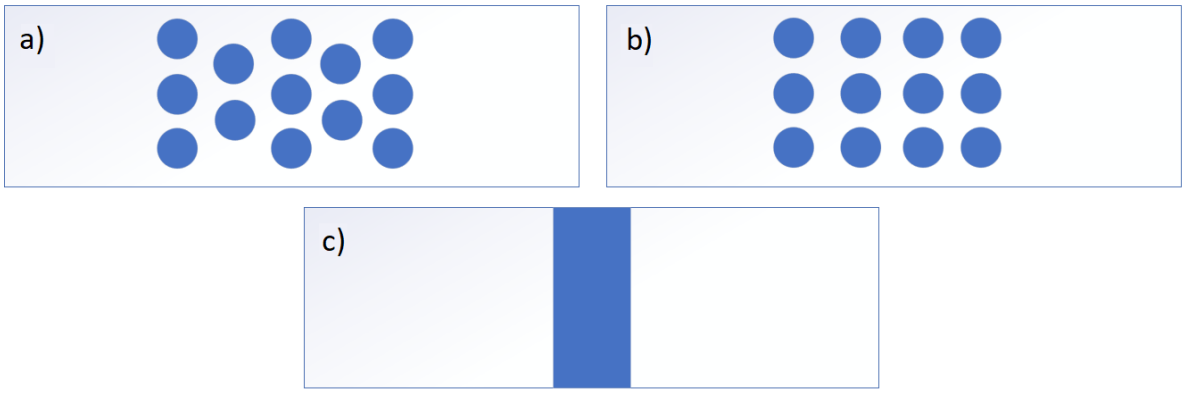


Figure 2.1: Different patterns discussed in this thesis a)dotted diagonal pattern , b) dotted horizontal pattern, c) line structure

the identified local behaviour can be coupled to overall material response and applicability.

2.2. Approach by simulations

Simulations are used to determine three important effect: (i) the effect of the architectured structure on the local deformation of the steel, (ii) the effect of the architectured structure on the overall stress-strain response of the steel and (iii) the effect of strength ratio between individual phases on the deformation behaviour of the material. Finally it is discussed how well the simulated results represent the observations made in the experiments regarding the deformation and stress partitioning. The advantages and limitations of the simulations are addressed.

2.3. Selection of patterns

Two patterns are experimentally investigated: (i) a dotted diagonal structure and (ii) a dotted horizontal structure. The choice of these structures is based on the topology design, producibility and the study of the behaviour of the contained phases. The structures are further examined using simulations where an additional line structure is investigated as well due to its available experimental results from previous research. Schematic examples of the structures used can be seen in figure 2.1. The structures are investigated using as-quenched martensite and tempered martensite base material to identify the difference in behaviour caused by the strength ratio between the soft and hard phase and are examined both experimentally and by simulations.

3. Experimental research

3.1. Experimental Procedure

3.1.1. Material

Every specimen used in this research comes from the same batch for which the composition is given in table 3.1. The alloy was vacuum casted in a 80 mm x 80 mm x 400 mm billet that was subsequently forged to a 50 mm x 50 mm x 1000 mm billet and homogenized at 1273 K for 12 hours. Flat coupons of 1 mm were machined from the billet with the use of a Electrical Discharge Machine (EDM). The final dimensions of the specimens used in this research have a length of 110 mm, a width of 20 mm and a thickness of 1 mm.

Table 3.1: Composition of the alloy

	%Ni	%C	%Mn	%Si	%Mo	%Al	%N	%S	%P	%Cr	%Fe
Wt-%	24.90	0.20	0.02	<0.01	<0.01	0.005	—	0.002	0.003	0.02	balance

The equilibrium phase diagram of the Fe-25Ni with variable carbon content from iron is calculated using the Thermocalc software [72] and is displayed in figure 3.1. At room temperature the equilibrium microstructure consists of FCC_A1 (austenite), BCC_A2 (ferrite) and cementite. Martensite forms under non-equilibrium conditions. The phase fraction of martensite formed depends on the undercooling below the martensite start temperature (M_s)[33]. Therefore it is important for further heat treatment that the M_s is known. For the calculation of the M_s the software package JMatPro 4.0 [73] is used which results in a M_s temperature of 291K with the given composition. It should however be noted that the carbon concentration has a significant influence on the M_s temperatures, which can cause local increased M_s temperatures as a result of decarburisation in the steel. Therefore it is possible for martensite to form even at higher temperatures.

3.1.2. Pattern creation

Base Material

To ensure the same prior austenite microstructure in all specimens, an initial salt bath heat treatment is performed of 60 seconds at 1173K after which the material is quenched in water. After obtaining the fully austenitic structure, the specimens are immersed in liquid nitrogen with a temperature of 77K for 600 seconds to create the martensitic base material. Half of the specimens were further subjected to a tempering heat treatment in an oven at 523K for 1800 seconds and air cooled to room temperature. After these treatments two different specimens are obtained: (i) as-quenched martensite (QM) specimens and (ii) tempered martensite (TM) specimens.

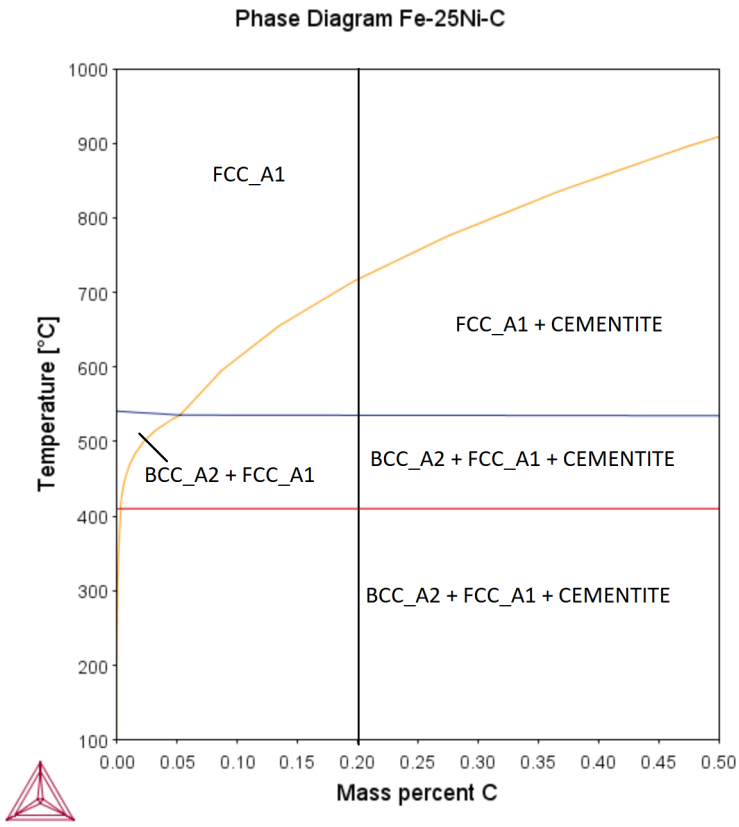


Figure 3.1: Equilibrium phase diagram of Fe-25Ni with variable carbon content obtained with Thermocalc [72]

Laser heat treatment

QM and TM were subjected to localised heat generated by a laser to create patterned structures by means of solid state transformation to austenite. The specimens for the laser treatment are used without further grinding of the surface. No reflection is expected due to the opacity. The laser used for this research is a Trumpf Trudisk 8002 Nd:YAG laser with a wavelength of 1064 nanometer. A single pulse laser beam is applied to the specimen. In order to create dots with diameter of around 3 mm, the focal distance is placed further away from the specimen by increasing the height of the laser. The initial distance is defined as the focal length and is set as 200 mm. Relative to the initial distance the laser hight is increased by 20 mm. With the focal distance defined in the suppliers data sheet, the beam spot diameter is calculated to be 2.9 mm. The beam spot is defined assuming a Gaussian beam profile until a dropped intensity of $1/e^2$.

Two experiments were used with the laser treatment to create dots on the specimen:

- (i) A single pulse on one side of the specimen is applied for the first experiment. This experiment is a preliminary test in order to define the parameters of the laser. It is important for the austenite pattern to have full penetration but also to avoid melting since a solid state transformation is wanted. Therefore an optimal should be found in the applied energy to the irradiated surface which can be done by changing the power of the laser or changing the exposure time. In this research the power is fixed

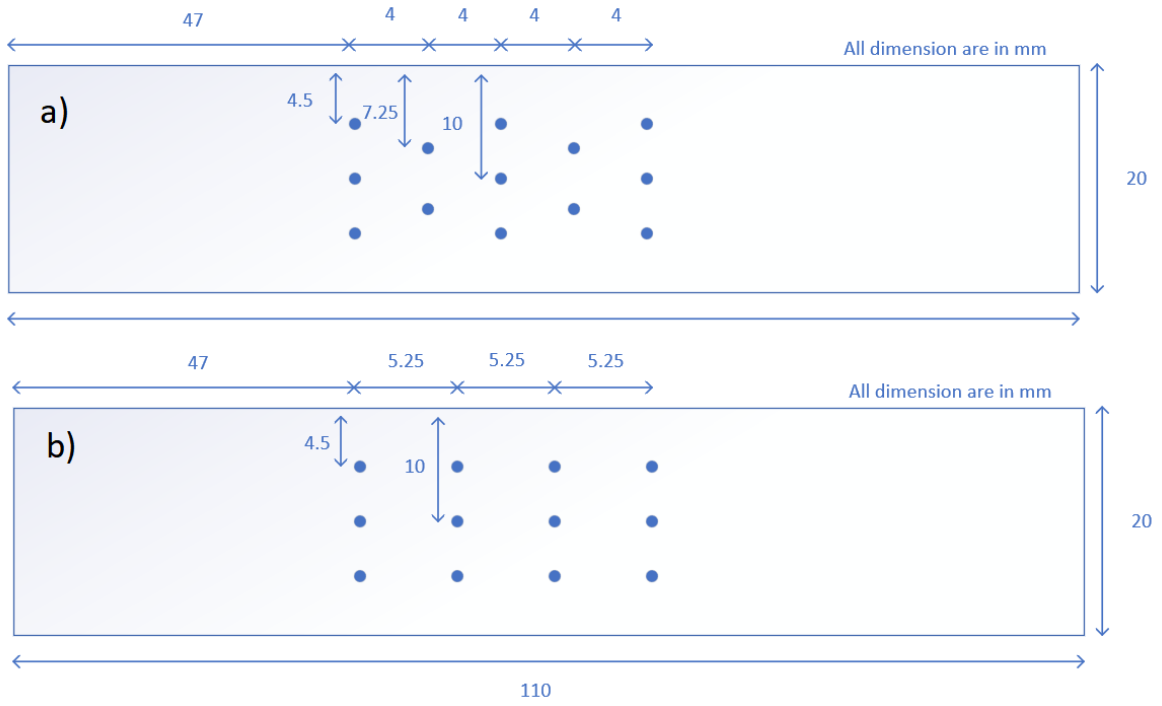


Figure 3.2: Dimension created pattern by laser treatment a) dotted diagonal pattern b) dotted horizontal pattern

to 400 W while the exposure time is kept as a variable. To assess the penetration and transformation of the dots produced by the laser treatment, three different specimens are tested. The laser parameters used in these three test are displayed in table 3.2 in which the height is again relative to the focal length. The parameters corresponding to specimen 3 are selected for further research in (ii)

- (ii) A single pulse is applied on both sides of the specimen in order to ensure a straight depth profile for further investigation. The most ideal parameters are chosen with regards to the initial laser experiment and further applied with a pattern on the specimens according to Figure 3.2. The laser pattern is applied on both sides of the specimen to achieve full penetration while trying to keep the diameter as constant as possible throughout the thickness of the specimen. The specimens created are split up in four different conditions. All specimens use the laser parameters defined for Specimen 3 in table 3.2 on both sides. QM is used for as-quenched martensite, TM is tempered martensite, diagonal (or /) is used to describe the diagonal shape created with the laser and horizontal (or -) describes the straight shape pattern:
  - As-Quenched Martensite with dotted diagonal pattern (QM/);
  - As-Quenched Martensite with dotted horizontal pattern (QM-);
  - Tempered Martensite with dotted diagonal pattern (TM/);
  - Tempered Martensite with dotted horizontal pattern (TM-).

Table 3.2: Laser parameters for penetration tests

	Power (W)	Exposure time (ms)	Energy (J)	Height (mm)
Specimen 1	400	70	28	20
Specimen 2	400	85	34	20
Specimen 3	400	100	40	20

3.1.3. Microstructural characterisation

Samples for optical microscopy (OM) were ground to a P2000 finish using a Stuers rotary grinder, and polished to a one micron finish using a Stuers Labopol polishing machine. Two different etchants are used in order to evaluate the microstructures[76]:

- Nital 5% (5 g HNO_3, 100 mL ethanol);
- Waterless Kalling's No.2 (5 g $CuCl_2$, 100 mL HCl, 100 mL ethanol);

Nital is used for revealing the martensite, which leads to an accurate contrast between the martensite and the austenite created by the laser treatment which is convenient for determining the phase fraction of austenite. Kalling reveals the austenite grain boundaries as well as the martensitic, due to their difference in contrast and morphology and is used for determination of grain sizes.

Light optical microscopy was performed using both a Leica DMLM optical microscope and a Keyence VHX-100 digital microscope, mainly to study initial microstructural features and the mechanically induced transformation. For the measurement of the average grain size, multiple random straight lines were drawn through the microstructure using ImageJ software. The number of grain boundaries intersecting the line are counted and divided by the line length.

3.1.4. Mechanical testing

Microhardness Testing

Microhardness measurements were performed in an EMCO G5 DuraScan and hardness Vicker 0.1 was selected. In HV microhardness testing, an indentation is made on the specimen by a diamond indenter through the application of a specified load. The size of the indentation, which is measured with the help of a calibrated optical microscope, determines the hardness of the indented region [77]. In this work the microhardness testing serves two purposes:

- For the evaluation of the hardness gradient at the LAZ. Three different specimens are inspected all with the laser parameters used with specimen 3 from table 3.2 without any prior deformation: (i) As-Quenched Martensite which is laser treated on only one side, (ii) As-Quenched Martensite which is laser treated on both sides and (iii) Tempered Martensite which is laser treated on both sides. The hardness is measured in the thickness cross section where five lines of indices are analysed as can be seen in the example in figure 3.3. The lines for (i) contain 50 measurements of hardness,

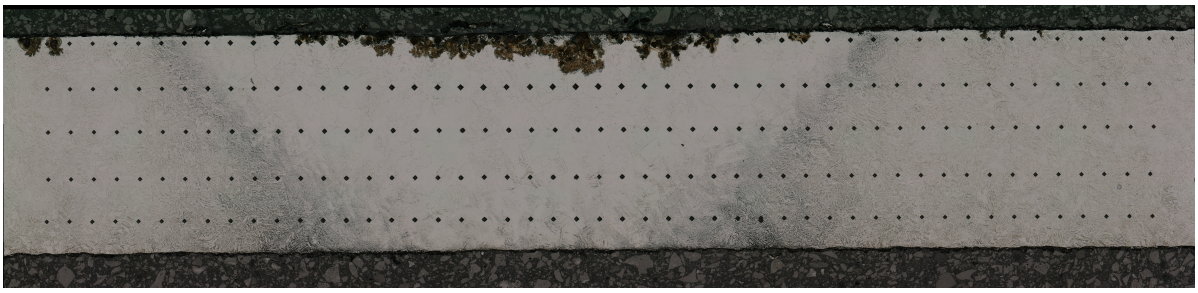


Figure 3.3: Hardness measurements on the QM sample laser treated on one side

whereas the lines for (ii) and (iii) contain 20 measurements. The indentations were made with 0.1 kilograms of force, and therefore measured on the Vickers Hardness scale HV 0.1.

- For the evaluation of the hardening behaviour of the individual phases after being subjected to deformation, the microhardness is measured for QM/1, QM-1 and TM/1 from table 3.3 and 3.4. Around ten measurements are taken for three different phases: (i) the austenite, (ii) the martensite formed due to the TRIP-effect and (iii) the martensite of the base material. Two as-quenched martensite samples and one tempered martensite sample are evaluated at different overall deformations.

Tensile testing
Tensile testing is performed to observe the overall and local deformation behaviour of the specimens with the four different conditions. During a tensile test a uni-axial load is placed on a specimen by means of a constant movement of the clamps. With the use of a load cell the load at each increment is determined after which the stress is calculate using the dimensions of the area of the specimen. The overall strain is measured with the use of an extensometer, whereas the local strain is measured with the use of Digital Image Correlation (DIC).

An Instron 5500R is used for performing the tensile tests. A preload of 500N is applied using a rate of 0.1 mm/s. The strain rate used while applying tensile load during the test is $0.0006 mm/mm/s$. The tensile tests are stopped at different strains in order to investigate the strain-induced martensitic transformations in the austenite. In table 3.3 and table 3.4 the specimens are shown with there corresponding strains at their highest strength value.

Table 3.3: QM tensile specimens with corresponding maximum strain values

Quenched Martensite			
Dotted diagonal pattern		Dotted horizontal pattern	
Specimen number	Strain [mm/mm]	Specimen number	Strain [mm/mm]
QM/1	0.014	QM-1	0.090
QM/2	0.064	QM-2	0.075
QM/3	0.055	QM-3	0.055
		QM-4	0.040

Table 3.4: TM tensile specimens with corresponding maximum strain values

Tempered Martensite			
Dotted diagonal pattern		Dotted horizontal pattern	
Specimen number	Strain [mm/mm]	Specimen number	Strain [mm/mm]
TM/1	0.091	TM-1	0.046
TM/2	0.039	TM-2	0.085
TM/3	0.062	TM-3	0.014
		TM-4	0.030

Extensometer
The extensometer has a gauge length of 25 mm and a maximum extension of 2.5 mm. Therefore during the tensile tests the extensometer has to be removed at strains higher than 9% since at higher strains this exceeds its range. QM/2, QM-2, TM/1, TM-1 and TM-2 where measured without an extensometer. In order to determine their overall deformation, the deformation of the clamps of the machine is used. By using this method a reference sample is used to correct for the compliance of the machine [74]. The reference sample for the As-Quenched Martensite is QM-1 and the reference sample for the Tempered Martensite specimen is TM/2.

An example is shown in Figure 3.4 in which QM/2 has different elastic behaviour compared with QM-1 which used an extensometer. Therefore QM/2 is corrected with the use of the elastic modulus obtained in QM-1 which shows significant change in the behaviour of the curve. After applying these corrections the results of the overall deformation of the extensometer and deformation of the machine can be compared.

Digital Image Correlation
Digital Image Correlation (DIC) is an optical technique which uses image registrations combined with tracking methods to accurately measure the change in images [75]. The tracking takes place by analysing a speckle pattern applied by the user, which gives a 'fingerprint' at a local scale. The tracking of the displacement of the image allows for accurately measuring of local deformation behaviour in the material. Two Q400 Limess DIC cameras were used to capture the local deformation. The scale of the local deformation behaviour is determined by the field of view specified. In this research the field of view is chosen with a height of 35 mm and a width of 40 mm which is accomplished by using a total tube length of 15 mm

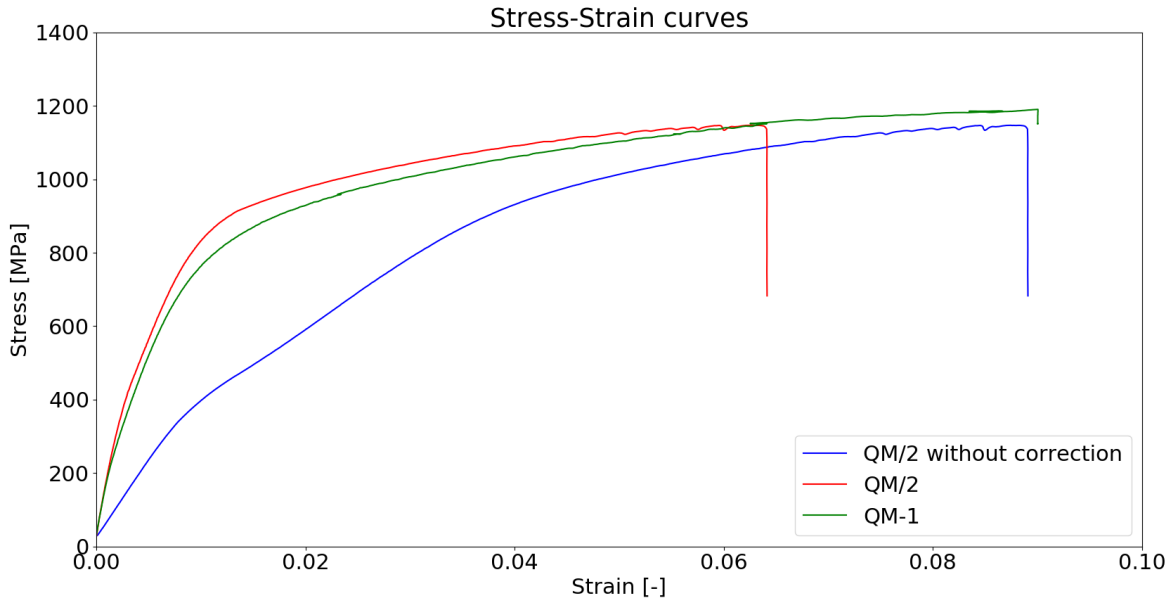
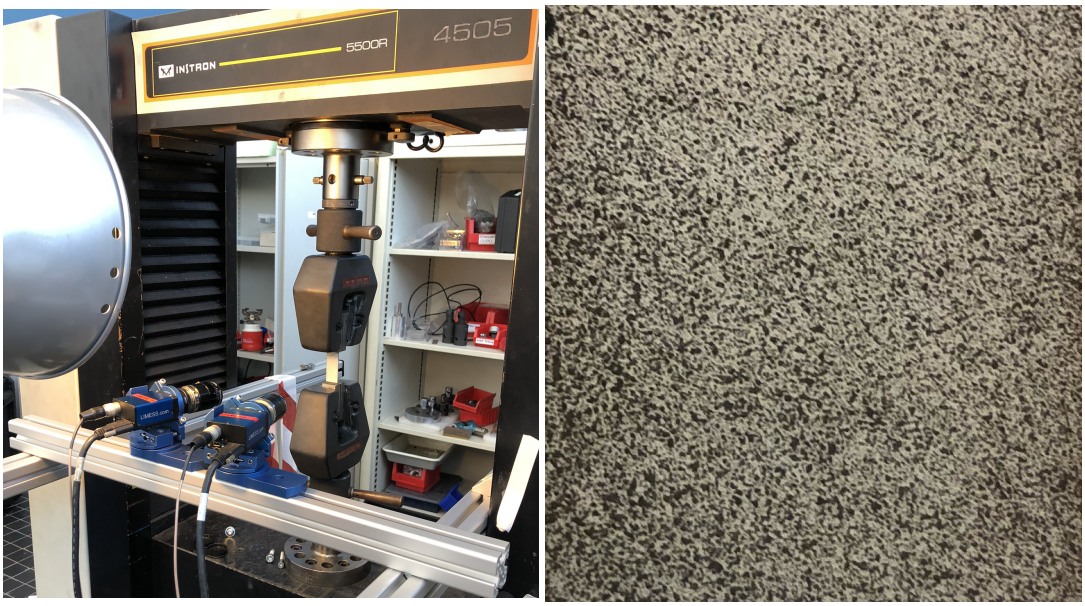


Figure 3.4: Example of correction of QM/2 without the use of an extensometer with the reference of QM-1

on the cameras. DIC is used simultaneously with the tensile machine but is synchronised manually by starting at the same time. In figure 3.5a the setup of the two cameras is shown. A light source is placed behind the cameras in order to create more contrast between the speckles for more accurate evaluation. In figure 3.5b one of the speckle patterns used in the test is shown in which the width captured in the picture displays the width of the specimen used. During the test every five seconds an image is captured, which corresponds to a picture every 0.003 mm/mm.



(a) Test setup with two cameras aligned to the specimen

(b) Speckle pattern used for DIC analysis

Figure 3.5: DIC analysis setup

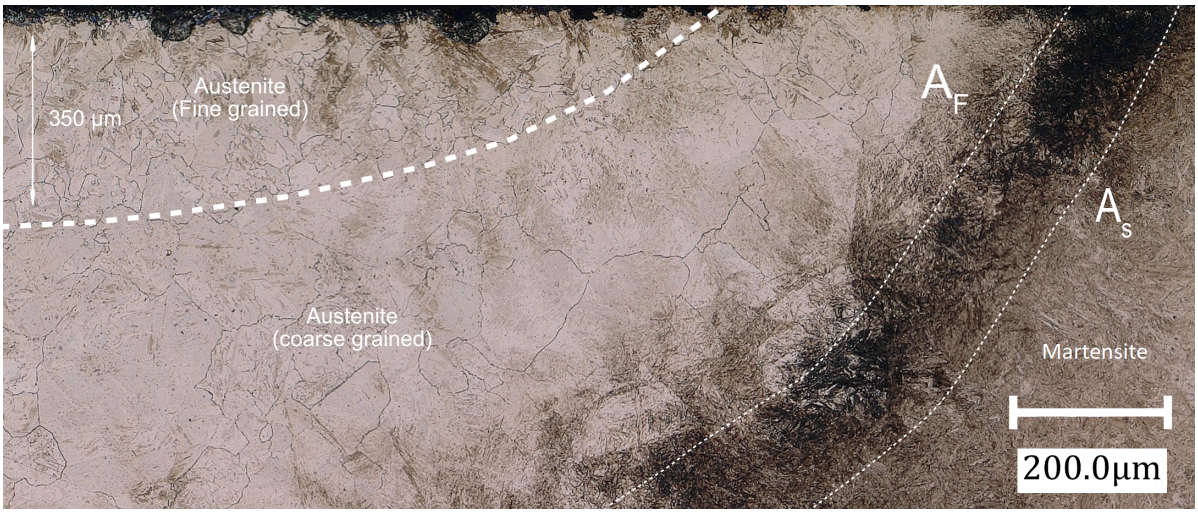


Figure 3.6: OM image where two main regions in the austenite can be distinguished: (i) fine grained region (ii) coarse grained region

For evaluation the software Istra 4D by Dantec Dynamics is used. In order to perform an accurate analysis, calibration needs to take place of the set-up used. A 9 mm x 9 mm calibration card was used to capture twelve images while tilting the card and moving it in the complete field of view. The combination of images captured during the test, and images captured during calibrations allows the software to accurately trace the local deformation.

3.2. Results

3.2.1. Microstructural characterisation of laser treated specimens

Single side laser treated specimen

The microstructures of the specimens laser treated on a single side as described in table 3.2 are characterized using optical microscopy. Only the QM base material samples are investigated, since similar penetration results are expected for the TM due to similar thermal properties between both base materials. A gradient microstructure is shown where three different zones can be distinguished: (i) the martensitic base material, (ii) the austenite created by laser treatment and (iii) the transition region between both zones. These regions are shown in Figure 3.6 from right to left respectively. The transition region between the austenite and martensite is distinguished by dark etching, which is the result of a temperature range between the austenite start temperature (A_S) and the austenite finish temperature (A_F). There also can be carbide formation in the region as indicated by the phase diagram in figure 3.1.

In figure 3.7 a magnification of the martensite base material is shown. Butterfly type of martensite can be observed, which is martensite in which each butterfly wing constitutes a single twin pair of martensite with relative misorientation angle of 16°. This type of martensite is a combination of twins and long dislocations and is typical for Fe-Ni alloys [78, 98].

Furthermore, in figure 3.6 a separation is made between two main regions within the austenite: (i) a fine grained region which is formed in the middle of the austenite and (ii) a more coarse grained region which forms the rest of the ausenitic region. The fine grained region has an average grain size of 26 μm whereas the coarse grained region has an average grain size of 103 μm. The fine grained region has a maximum depth of 350 μm in the middle which decreases when going further away to the side of the dot. This is the result of the intensity of the laser which is assumed to have a Gaussian beam profile and therefore generates more heat in the centre of the austenite region.

Figure 3.8 shows a more detailed view of the grain structure in the top of the sample. A clear difference can be seen within the small grains and the larger ones. The small grain boundaries appear to have straight boundaries (SB) whereas the larger austenite grains have wavy grain boundaries (WB). It is hypothesized that these wavy grain boundaries are the result of previous existing butterfly martensite wings which undergo displacive transformation. Considering this assumption the small grains which do not show wavy boundaries are formed using diffusional processes causing nucleation and growth due to recovery and recrystallisation. This behaviour give distinct properties between the two types of grains which are further investigated using microhardness test.

The results of penetration due to the localised laser treatment are shown in figure 3.9 which shows a thickness cross-section of the specimens. Melting of the sample is not wanted since only a solid state transformation should take place. Neither of the samples show signs of melting as can be seen in figure 3.9. The energy input in specimen 1 is not sufficient to fully penetrate the sample, whereas in specimen 3 full penetration does takes place. For specimen 2 additional heat is generated in the bottom of the sample since austenitic transformation is visible on the bottom left of the captured region. However this is not directly

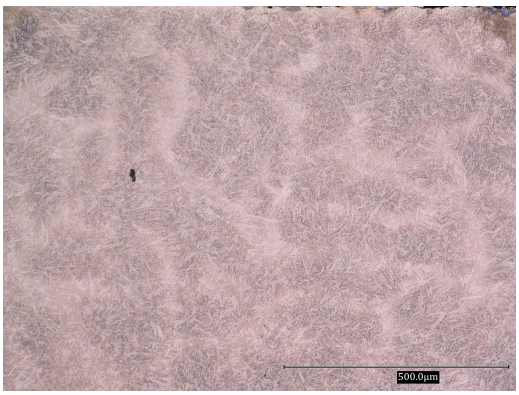


Figure 3.7: Martensitic structure of the base material

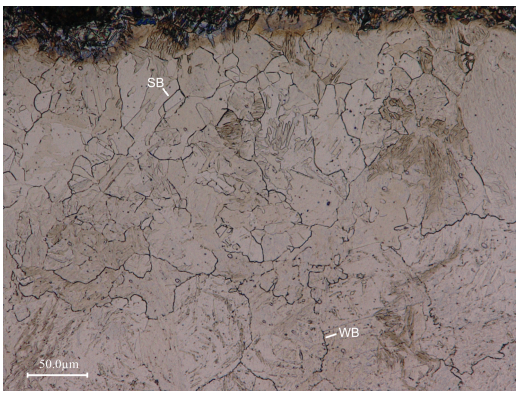


Figure 3.8: Grain structures within the austenite

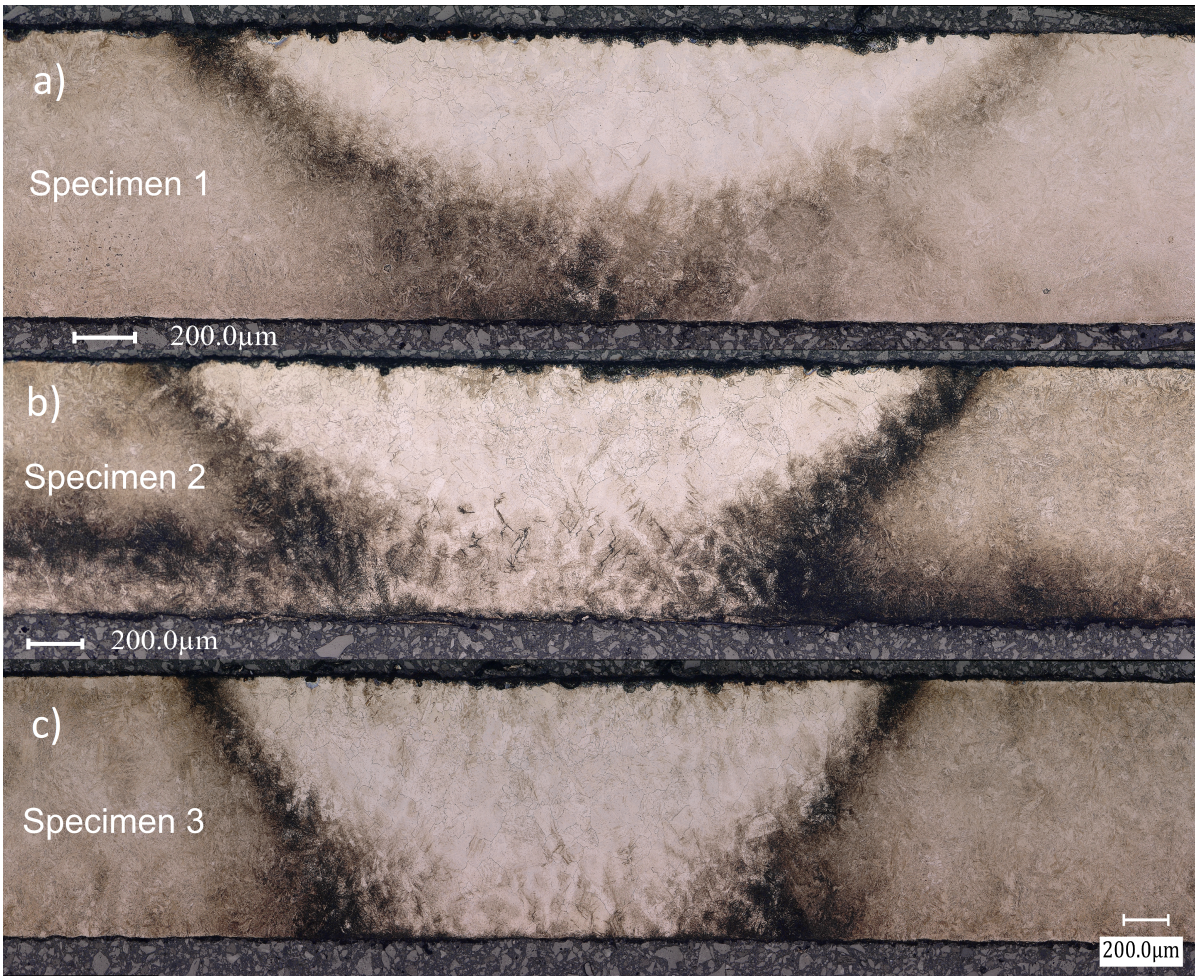


Figure 3.9: Penetration of austenite formation in the laser sample for specimen 1 (a), specimen 2 (b) and specimen 3 (c) according to table 3.2

caused by the laser beam. Therefore, it can not be said with certainty that full penetration is achieved by using these laser parameters.

Further analysis of the microstructures is done regarding the maximum penetration of the fine grained region for all specimens and the austenite grain sizes in both the fine grained and coarse grained region. These values are shown in table 3.5. It can be observed that the penetration of the fine grained region increases significantly with an increase in energy applied to the specimen. The average coarse grain size is relatively constant with a somewhat smaller value for the first specimen. For the average fine grain size specimen 2 and 3 are comparable whereas specimen 1 has slightly larger grains.

Table 3.5: Microstructural features for the different specimens

	Avg fine grain size (μm)	Avg coarse grain size (μm)	max penetration depth fine grained region (μm)
Specimen 1	33 ± 2	93 ± 3	228
Specimen 2	24 ± 1	105 ± 4	293
Specimen 3	26 ± 2	103 ± 2	350

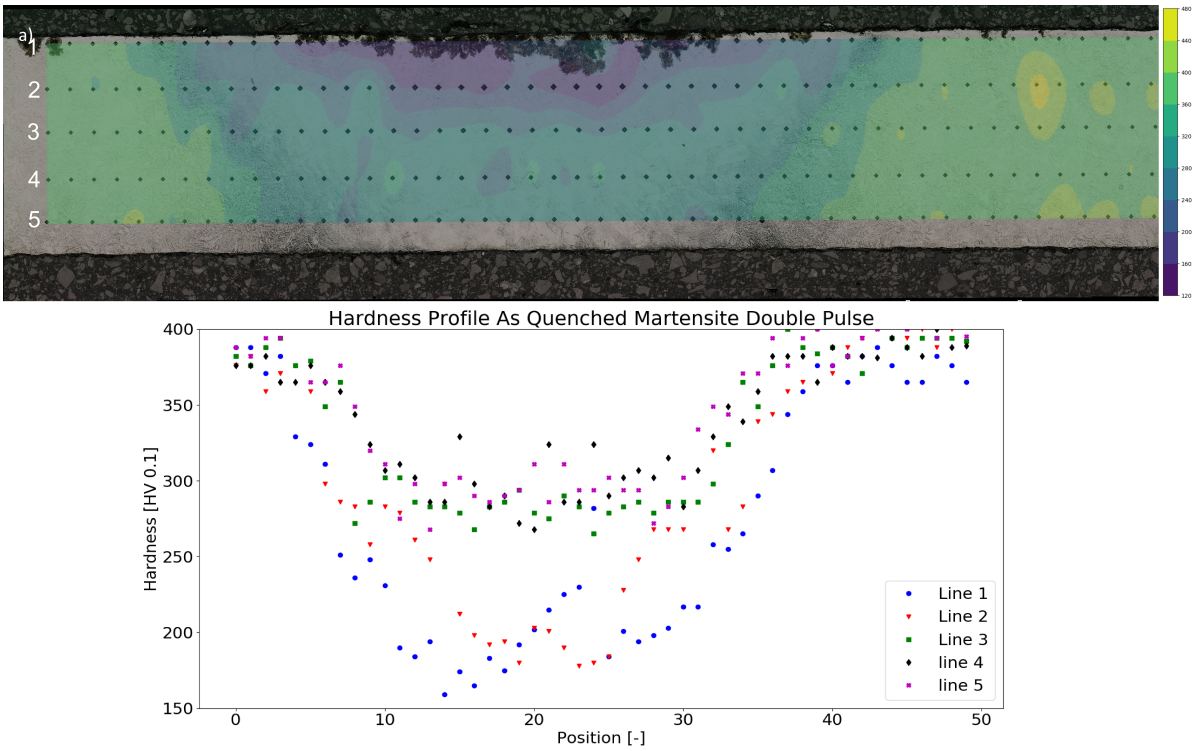


Figure 3.10: Interpolated hardness map of QM of the single spot (a) along with the hardness values for the indices graphed (b)

For further experiments the laser parameters of specimen 3 are used. The width of the austenitic region decreases with the thickness of the material which should be corrected as much as possible, therefore the samples are laser treated on both sides for further experiments to reach full penetration and a constant thickness.

Double sides laser treated specimens

The double sided laser treated specimens were also investigated for the comparison of their grain sizes due to the extra heating on the other side. There is an overlapping zone in the middle of the specimen in which heating from both sides takes place. The average coarse grain size in this region is 109 μm and the average grain size of the small grained region is 26 μm. These values are comparable to the single side laser treated specimen. Hence no further intensive investigation is done regarding these specimens.

3.2.2. Hardness at LAZ in non-deformed specimens

Single side laser treated specimen

First the hardness of the QM specimen which is laser treated on only one side is evaluated. The results presented in Figure 3.10 are shown in the form of a hardness map which is made by interpolation of the hardness data from the measured indices. A plot in which each value for the microhardness of the indentations is given is displayed as well. Lower hardness values are observed in the top-middle of the specimen where the small grains are formed. In these regions the hardness is around 200 HV whereas in the same position deeper in the

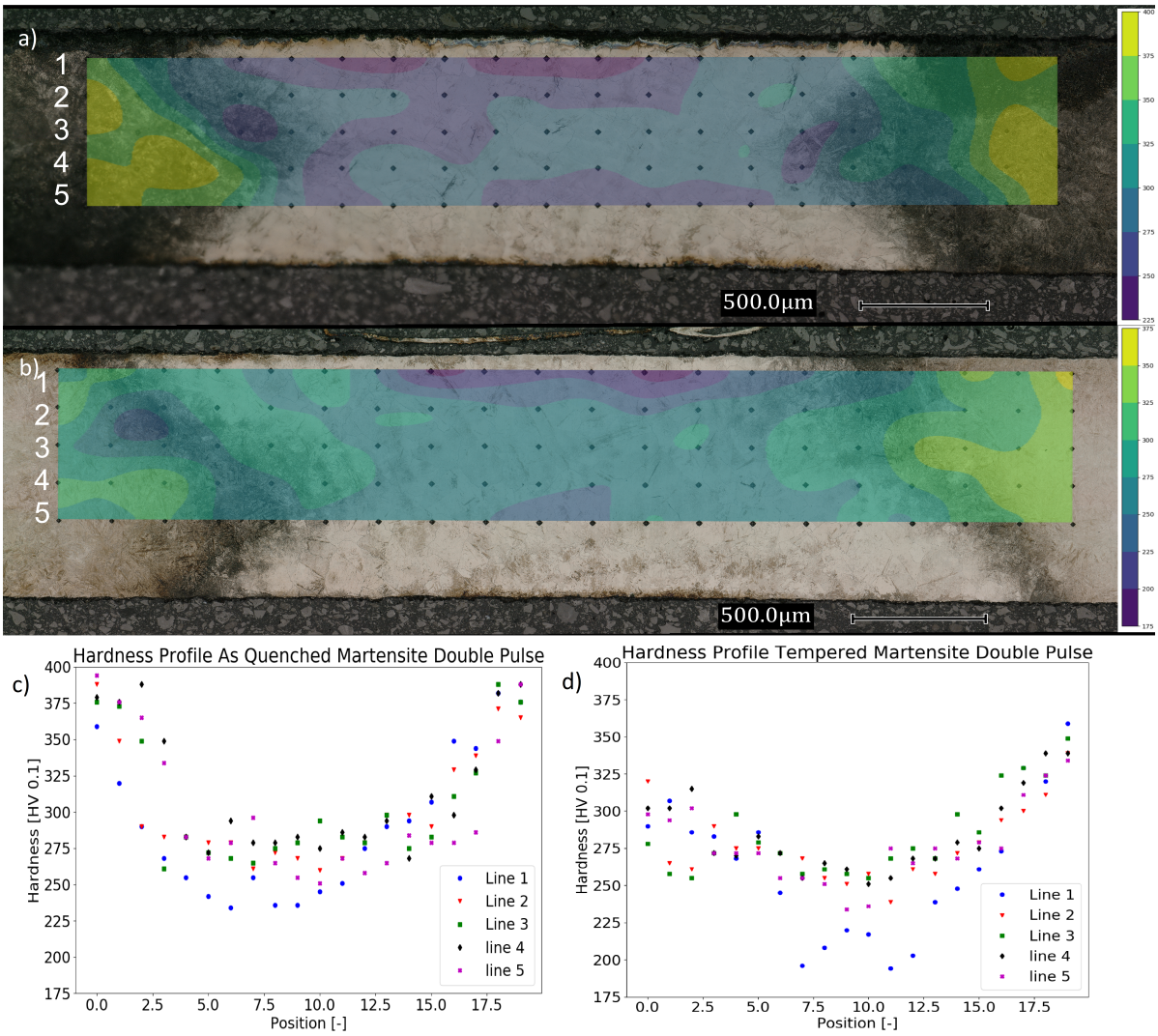


Figure 3.11: Interpolated hardness map of QM (a) and TM (b) along with the hardness values for the indices graphed (c,d)

material the hardeness is around 300 HV. This increase in hardness is correlated with the size of the grains observed.

The austenite structure created by the laser is well reflected by the hardness measurements given by the interpolated map. The martensitic base material has hardness values around 390 HV which decreases at the inter-critical region where both martensite and austenite co-exist. This decrease of hardness flattens for line 3-5 after reaching the austenite, whereas for line 1-2 there is an extended decrease in hardness due to the larger grains around the sides of the dot which are gradually becoming the small grains when going to the centre. Within the austenite some martensite still exist, therefore the higher hardness values in the profile can be caused by an indent in martensite.

Double sides laser treated specimens
For both the QM as the TM specimens a hardness map is created along with the values of the single indentations. The results of these measurements are shown in Figure 3.11. The measurements do not fully cover the complete thickness of the specimen but in principle both sides behave in a similar manner and therefore can be mirrored. An interesting area is the overlapping region between both transformations. The hardness map shows distinct regions of martensite, inter-critical region and austenite. The lowest hardness values are obtained with line 1 which corresponds with the small austenite grains. The indentations of line 2 are in both cases in larger grains, hence the higher hardness values.

The martensite in the QM base material has an average value of 356 HV in which all indentations in this area are included. For the TM samples the hardness of the martensite has an average value of 315 HV. The hardness of the martensite in the TM base material on the left side of the austenite is ranging between 278 and 320 HV whereas the hardness of the martensite on the right side ranges between 300 and 349 HV. The average hardness for the austenite for all lines is taken for both the QM (between indentation 5 and 13) and the TM (between indentation 6 and 14). The austenite of the TM has an average hardness value of 254 HV whereas for the QM the average hardness is 270 HV.

The hardness in the middle of the sample is comparable to the specimen laser treated on a single side. However the hardness values of the top region of the QM specimen are larger in the double treated specimens. The difference between these hardness values can be as high as 75 HV. The measurements of the hardness values of the sample treated on a single side are taken closer to the surface where smaller grains are created compared to the double side specimens which could explain this high difference.

While the hardness of the austenite in QM and TM is comparable, the gap between the hardness of the martensite and the hardness of the austenite for the QM is almost two times bigger than for the TM specimens. It shows that by applying laser treatment the strength difference between the martensite and austenite is varied for the different base materials.

3.2.3. Overall deformation behaviour in the architectured structures

Figure 3.12 show the true stress-true strain curves of the base material of the three different phases: (i) Austenite, (ii) As-Quenched martensite and (iii) Tempered martensite. These stress-strain curves are obtained from previous research [80] with the same material and treatments.

The austenite has a UTS of 1034 Mpa at a strain of 0.222. There is linear hardening behaviour of the austenite after reaching the yield strength at around 200 MPa which is caused by the twinning and mechanically induced transformation . Austenite is tested before the cryogenic creation of martensite and hence its behaviour could differ from the austenite within the created architectured pattern due to the reversed austenization process.

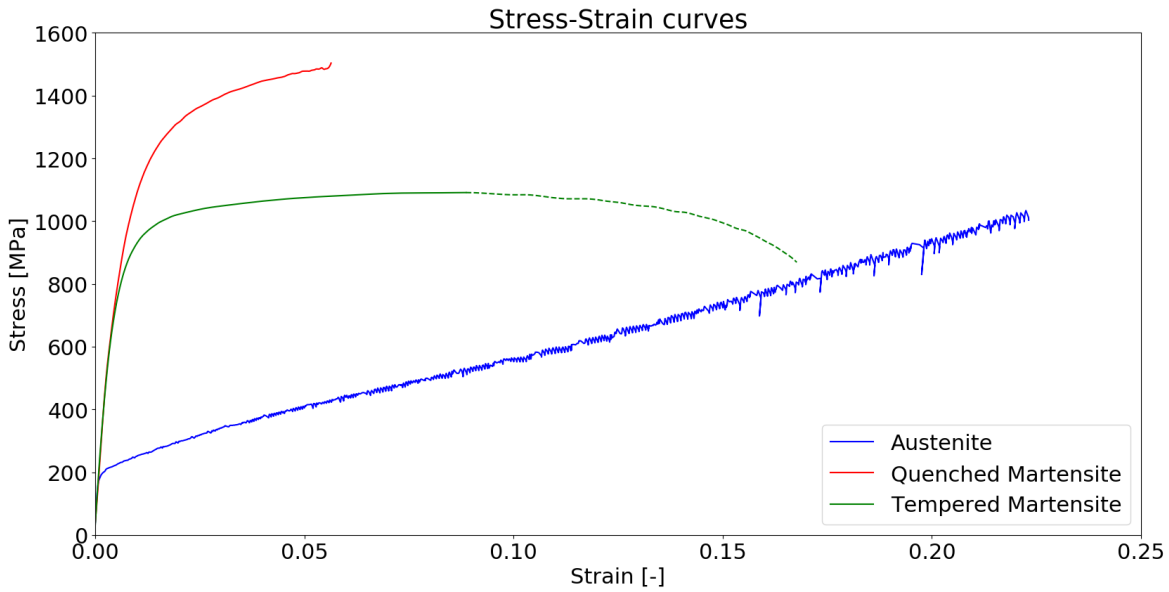


Figure 3.12: True stress- True strain curves of the base material for the individual phases

The QM has a UTS of 1503 MPa at a strain of 0.056 and a yield strength of 1150 MPa which is determined using the 0.02% offset method. The hardening behaviour of the QM is less than for the austenite however it is still clearly observed. For the TM the UTS is 1091 MPa at a strain of 0.088 and a yield strenght of 900 MPa. The TM specimen does not show much hardening behaviour and the plastic regime is mostly flat. However, QM breaks at UTS and TM exhibit extended elongation.

The true stress-true strain curves of the architectured materials are compared to that of the base material in Figure 3.12. Three specimens of the as-quenched martensite (QM/2, QM-1 and QM-2) and two specimens of tempered martensite (TM/1 and TM-2) are loaded until break. All the other specimens are also tensile tested and the results are displayed in Appendix B. Due to crack initiation at low strains some specimens broke prematurely, probably due to crack formation during the initial heat treatment of the martensite. Moreover, the curvature formed during initial heat treatment can possibly change the tensile test results since it can not be considered as a fully uni-axial tensile load.

In the QM the dotted structures have considerably smaller UTS than the QM base material but greater than the austenite. The dotted horizontal pattern shows more strain than the dotted diagonal pattern, however it is not possible to conclude that the form of the structure has such a influence on the maximum strain since only one specimen of the dotted diagonal pattern is examined. Compared to the QM base material there is thus a reduction in strength but an enhancement in maximum strain. The reduction in strength is caused by a lower yield strength of the QM patterned structures. The hardening of the material is comparable to QM base material.

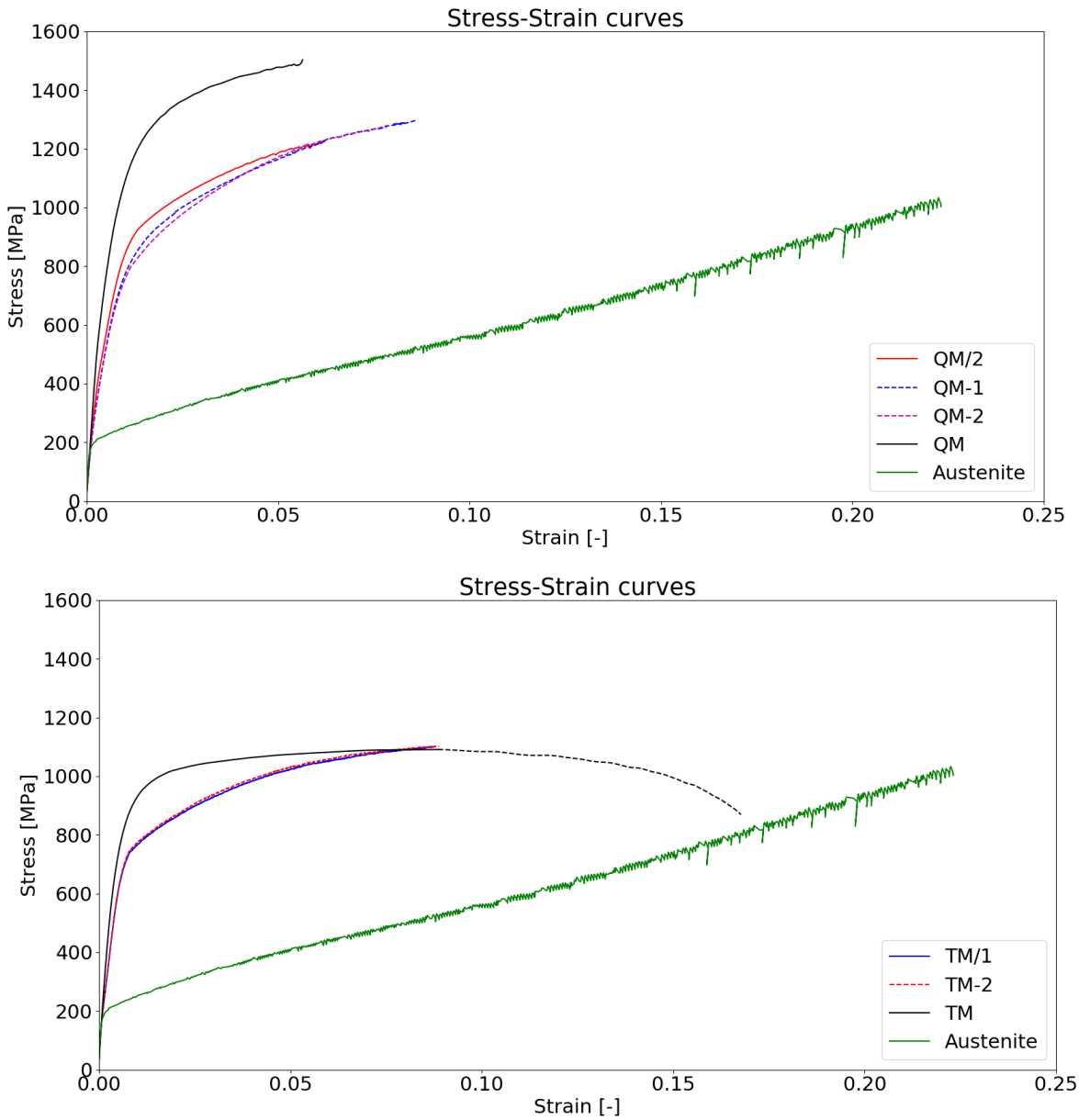


Figure 3.13: True stress- True strain curves of (a) as-quenched martensite specimens and (b) tempered martensite specimens

The energy absorption of the material is represented as the area under the curves. For the QM samples it can be observed that the patterned specimens can absorb more energy than the base material, hence showing higher toughness. For the TM the patterned structure absorbs significantly less energy than the base material which is mainly caused by the immediate break after the UTS while the base material still deforms.

For the TM, the base material shows some reduction in stress with increasing strain after reaching the UTS. This is because the reduction in the area of the specimen is not measured and therefore after UTS the line is dotted. This line is still shown in order to clarify that the all specimens with a pattern fail directly after the UTS whereas the TM base material does not. TM/1 and TM-2 are comparable and show a UTS similar to that of the TM

base material. The hardening behaviour of the base material has a much lower hardening rate compared to the architectured material and also has a considerably higher yield strength. The difference between both the dotted diagonal pattern and the dotted horizontal pattern is negligible, hence showing that both structures do not differ much in the overall deformation behaviour.

3.2.4. Local deformation behaviour by DIC

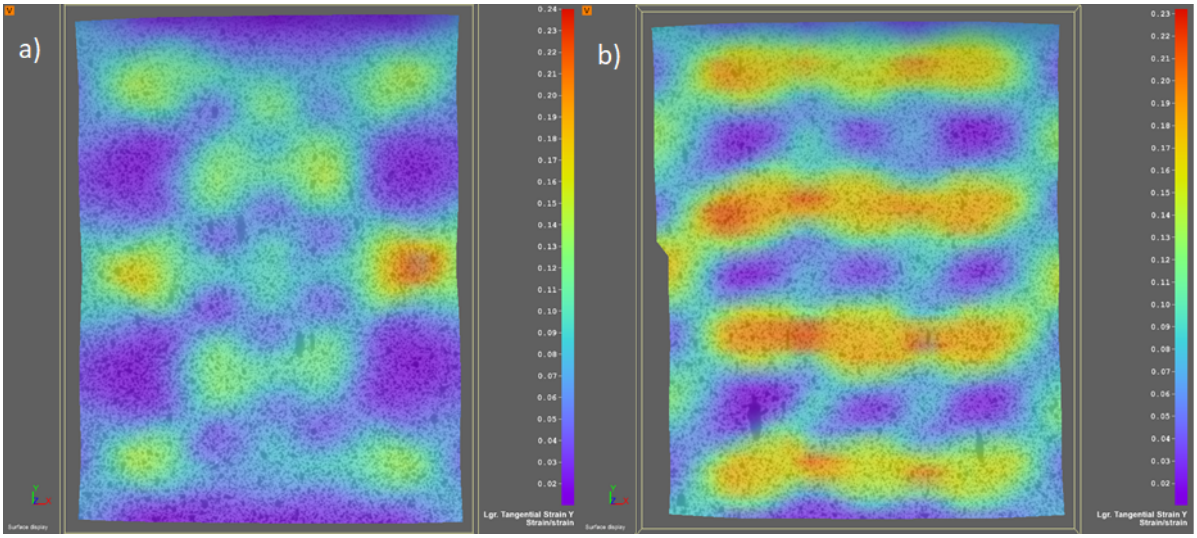


Figure 3.14: DIC results of the QM for (a) the dotted diagonal pattern and (b) the dotted horizontal pattern with an overall strain of 0.055

In Figure 3.14 the DIC map for both the dotted diagonal pattern (QM/3) and the dotted horizontal pattern (QM-3) is given. Both specimens have an overall strain of 0.055. All other DIC maps for the maximum strain can be examined in Appendix A. From the DIC result it can be concluded that strain partitioning takes place in the austenite phase, the dotted structure is clearly visible:

- The dotted diagonal pattern show austenite dots with higher local strain than in the martensite. Two dots at the third line which are close to the sides show even more strain which can be linked to crack initiation. The dots are connected to each other with strain bands of two types: (i) a connection between dots in the x-direction and (ii) a diagonal connection between dots. The area between the dots in the y-direction contain the least amount of deformation, where the martensite only slightly deforms.

- The dotted horizontal pattern show similar behaviour, however the material experience more consistent strain between the dots. The strain bands within the martensite connecting the austenite dots in x-direction contain large strain fields which are as high as in the austenite. Small strain partitioning band in the martensite are observed, connecting the dots in diagonal direction. The martensite area between the dots in the y-direction contain almost no strain. Strain partitioning is observed in the martensite at the free surfaces in between the horizontal dotted lines. These areas are connected to the dots with diagonal strain bands.

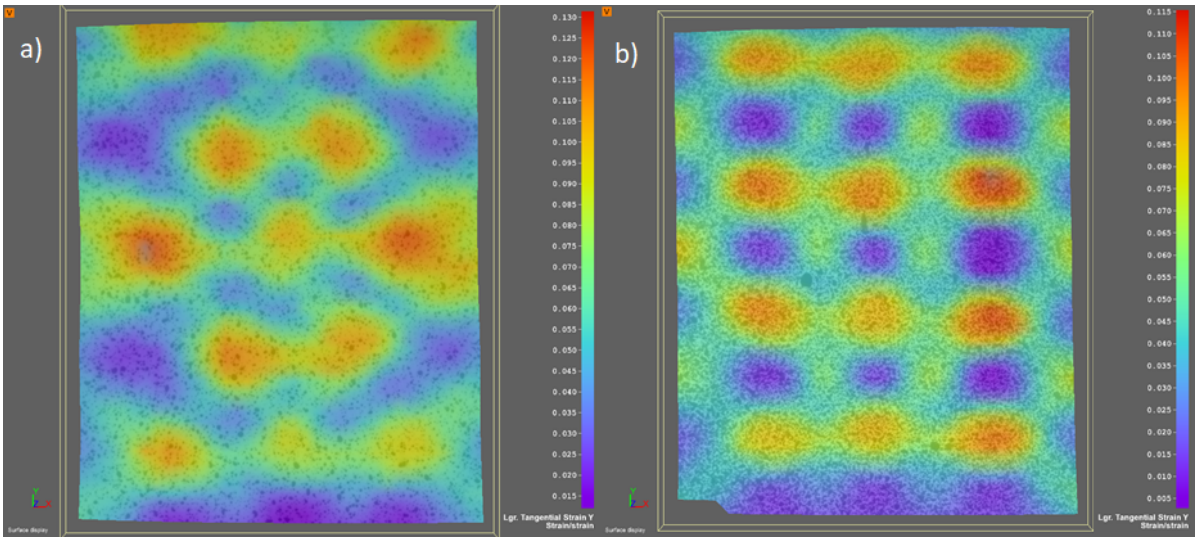


Figure 3.15: DIC results of TM for (a) the dotted diagonal pattern and (b) the dotted horizontal pattern

For the TM specimens the results of TM/2 and TM-4 are discussed which have an overall deformation of 0.039 and 0.030 respectively and are shown in Figure 3.15.

- The dotted diagonal pattern shows the same observations as in the QM, where the strain partitioning is clearly visible in the austenite dots. However the strain band in the martensite connecting the austenite dots are better distinguishable due to the higher localised strain. The strain partitioning in the dots seems more spread out which suggest that the strain partitioning is less local in the TM specimens. The specimen shows strain bands connecting the dots in x-direction and diagonally with similar local strain values.

- The dotted horizontal pattern shows clear strain partitioning in the austenite dots. There is a clear strain partitioning in the martensite in the area in the middle of the four dots which has about half the strain as in the austenite. Together with the strain bands in x-direction these strain give almost a straight line in the y-direction with strain partitioning. These spots can be the result of overlapping diagonal strain bands and therefore do not differ from previous cases other than the magnitude of the strain. There is also some strain partitioning taking place in the martensite at the free surface between the horizontal dotted lines.

The fracture pattern of QM/2, QM-2 and TM/1 are captured to see if this behaviour corresponds with the local strain partitioning as can be seen in Figure 3.16. It is observed that QM/2 has a crack initiation and propagation which goes into the x-direction of the specimen whereas for QM-2 the crack develops at an angle around 45°. These observation correspond perfectly with the local strain observed in the DIC results shown in Appendix A. For both QM/2 and QM-2 the fracture goes through the austenite dots. This behaviour is also explained through the DIC results since the strain partitioning for the QM is localized around the austenite dots.

The fracture pattern of TM/1 corresponds to the local strain partitioning which shows crack initiation at an angle around 45°. The development of the crack occurs at the edges of the austenite dots, hence going through the martensite. In the local deformation map the strain partitioning is more spread out thus stimulating crack propagation in the martensite. Further investigations of the fracture surface of the specimen is beyond the scope of this research and therefore not included.

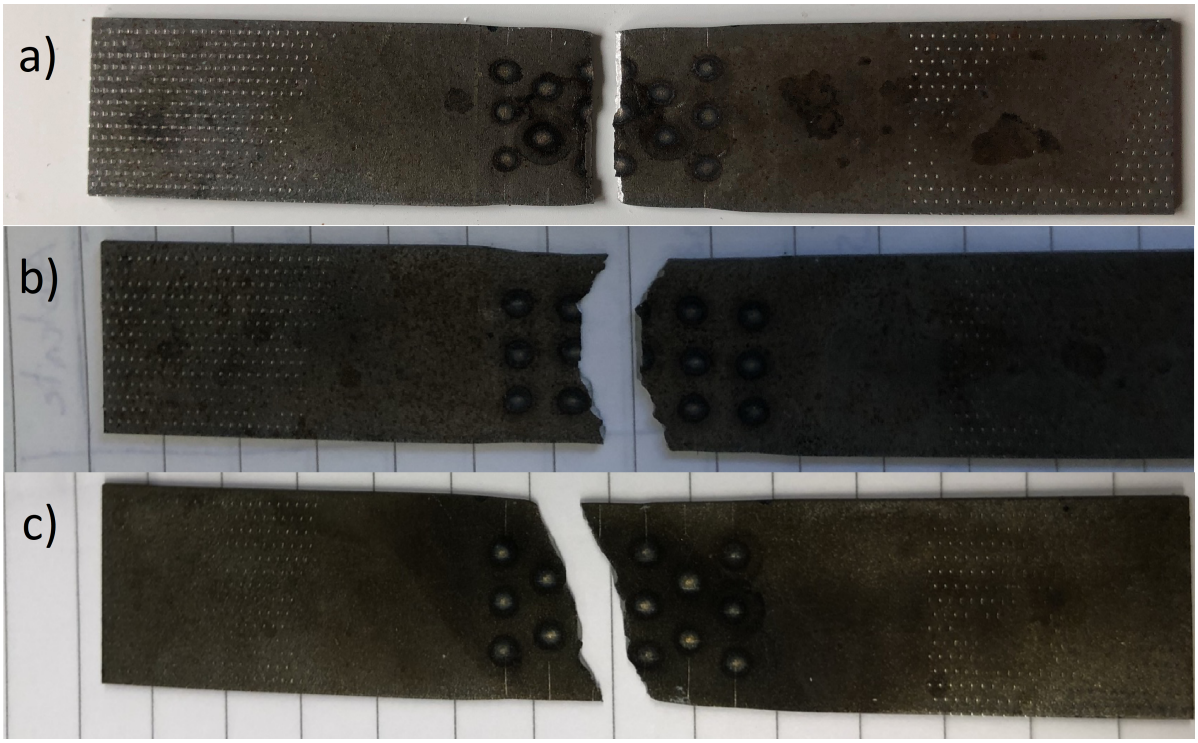


Figure 3.16: Fracture of the specimens: (a) QM/2, (b) QM-2 and (c) TM/1

3.2.5. Mechanical stability of austenite

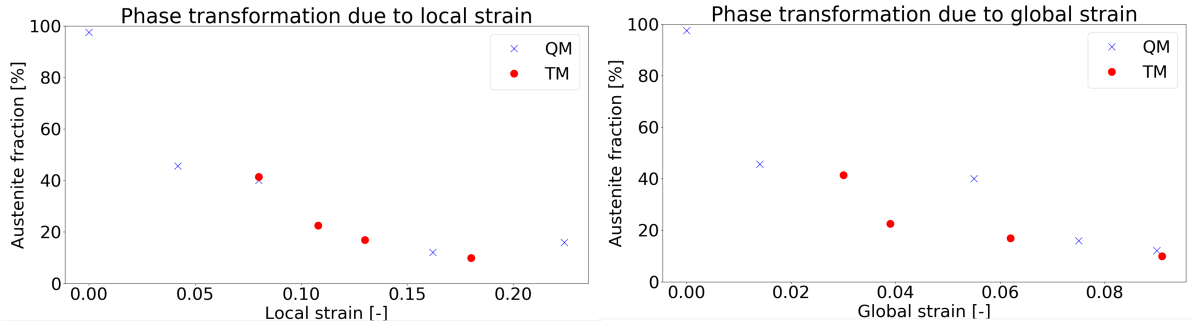


Figure 3.17: The austenite phase fraction in the laser treated area as a result of (a) the local strain and (b) global strain

TRIP effect can take place in the austenite giving the material an enhancement in both the strength and the ductility. This is caused by the transformation of austenite in martensite during plastic deformation. To measure the amount of austenite transformed as a consequence of the local strain, several dots of austenite are microscopically examined. The

amount of austenite still present is determined using ImageJ which uses the contrast of the different phases due to etching with Nital.

The phase fraction of the austenite is measured for an initial QM specimen with no deformation, four deformed QM (QM/1, QM/3, QM-1 and QM-2) and four deformed TM specimens (TM/1, TM/2, TM/3 and TM-4). In these specimens the local strain within a single dot and the global strain are obtained from the DIC experiments and tensile test respectively. Resulting from this the austenite phase fraction is given as a function of the local strain in Figure 3.17a and the global strain in Figure 3.17b.

For the local strain a clear exponential decrease in austenite phase fraction is observed in which at a local strain of 0.042 already 55% of martensite formed. It is difficult to conclude that there is a difference between the formation of martensite as a consequence of the strain between QM and TM since there is limited data obtained. At a local strain of 0.08 both QM and TM have a similar austenite phase fraction. In order to draw a reliable conclusion about the difference in austenite to martensite transformation as a result of the TRIP-effect between QM and TM more experiments need to be conducted.

The global strain shows similar exponential decrease. However, some points have comparable local deformations with high difference in global deformations. This results in a different trend compared to the local deformation in which the decrease of austenite fraction is not as smooth.

Examples of the austenite to martensite phase transformation are given in Figure 3.18 in which three different loading conditions are shown: (a) An undeformed specimen with 0 strain, (b) a dot from QM/1 with a local strain of 0.042 and (c) a dot from QM-1 with a local strain of 0.162. The following observations can be made:

- At the undeformed specimen (Figure 3.18a) butterfly martensite is already present in the middle and top region, but in very small fractions (2.45%).
- The developed martensite is formed first in the middle of the dot as can be seen with the help of the QM/1 specimen (Figure 3.18b).
- The newly developed martensite in QM/1 is formed at an angle of 45 °with respect to the surface (Figure 3.18b).
- In specimen QM/1 the martensite is party butterfly martensite, as in the base material. However in some regions martensite is packed more dense and looks more like lath martensite (Figure 3.18b).
- In QM-1 only small regions of austenite exist and the martensite which is formed shows only a small fraction of butterfly martensite within the austenite region. Instead mostly lath martensite is formed (Figure 3.18c).

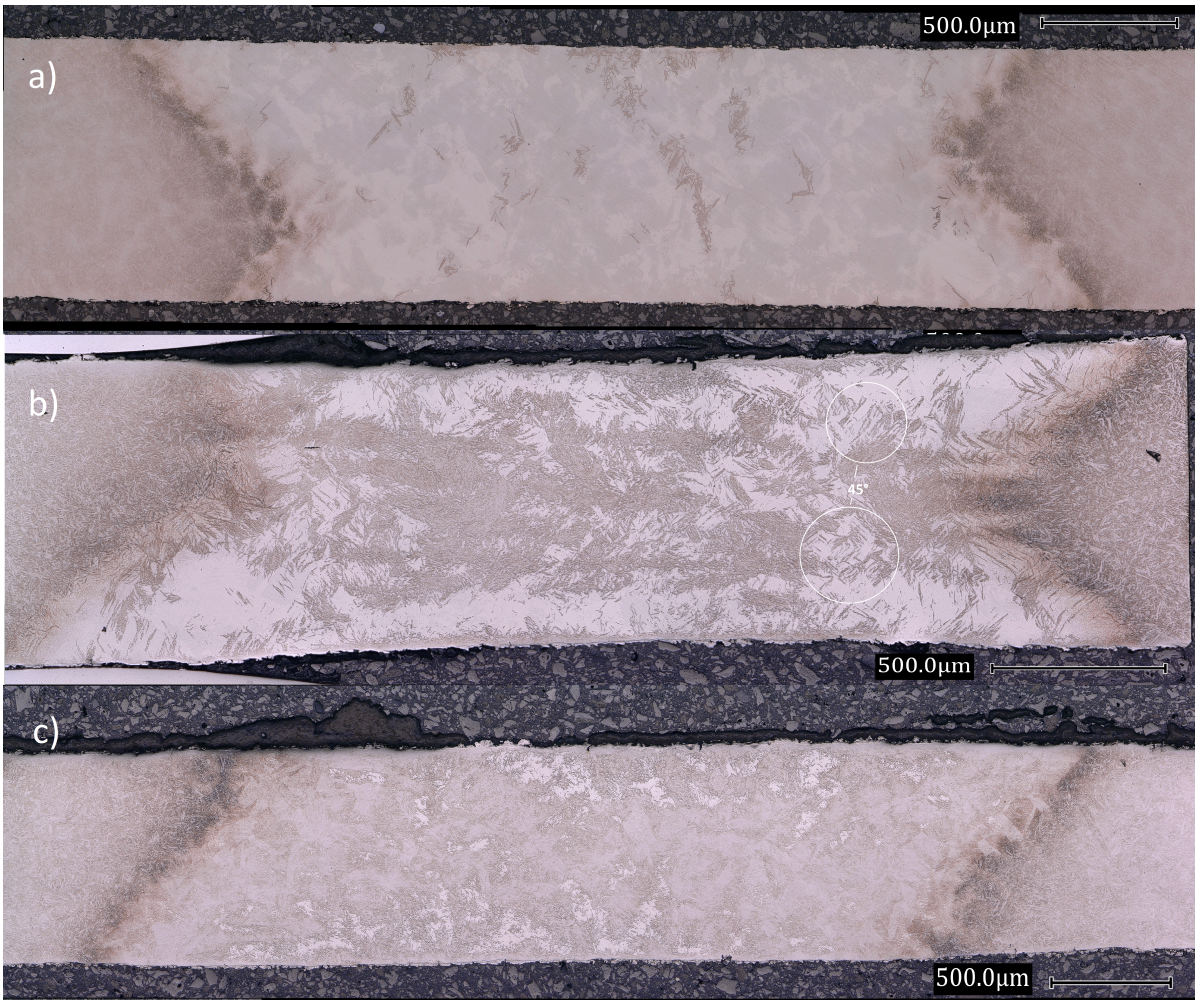


Figure 3.18: OM images of the austenite dot which display martensitic transformation with different local strain values for a) 0, b) 0.042 and c) 0.162

3.2.6. Hardening of different phases

Microhardness measurements are performed after deformation took place to investigate the hardening in different individual phases. Three distinct phases are examined: (i) the martensite of the base material, (ii) the austenite phase and (iii) the martensite formed as a result of the TRIP-effect. These measurements, performed on two QM samples with local strain of 0.042 and 0.162 (QM/1 and QM-1) and on one TM specimen with a a local strain of 0.180 (TM/1) are displayed in Table 3.6.

The hardness values obtained from the non-deformed material from Figure 3.11 are included in the table as the initial state. The deformation has a significant influence on the hardness values of the both the martensite and the austenite. For the QM specimen the average hardness of the austenite and the martensite increases with increasing local strain. The TRIP-martensite of the QM specimen is harder than the base material martensite. This difference increases with increasing strain.

The TM specimen shows an increase in average hardness of the austenite and the martensite due to an increase in strength. For the TM specimen the hardness of the TRIP-martensite is significantly higher than the martensite of the base material. In all these observations it is clear that the deformation still causes hardening in all phases considered.

Table 3.6: Microhardness values of the individual phases for different specimens

	Overall strain (-)	Austenite (HV 0.1)	TRIP-martensite (HV 0.1)	Base martensite (HV 0.1)
Initial QM	0	270	-	356
QM/1	0.042	293	408	396
QM-1	0.162	329	527	474
Initial TM	0	254	-	315
TM/1	0.180	278	474	392

3.3. Discussion

In this section the results which are obtained through the experiments are discussed further. The section is subdivided in two main part: (i) discussion of the microstructure formed as a consequence of the laser treatment and (ii) the deformation behaviour as a result of the architectured structure.

3.3.1. Microstructure of the laser treated specimen

The microstructural features of the austenite created by the laser treatment are dependent on the parameters used by the laser and due to the thermal properties of the material. The laser generates the heat at the surface of the material after which the heat is conducted into the material. As per the heat equations supplied in D.R. Poirier et al. [79] a temperature gradient exist in all directions of the material and demonstrated in previous master thesis [80]. Due to the temperature gradient, different solid state transformations take place at different areas. These areas are described from far away from the heating source to close: (i) base material, (ii) intercritical region, (iii) large austenite grains, and (iv) recrystallized austenite. These regions are shown in Figure3.6.

- (i) The base material is not affected by the heat generated. In this area the highest hardness values are obtained due to the high dislocation density within the martensite as well as the trapped carbon in the octahedral sites of the martensite [64]. Lower hardness values are obtained in the TM specimens compared with the QM specimens due to the carbon atom segregation and the carbide precipitation in the TM which reduces the lattice distortion. In the case of the QM specimens, a tempered martensite region is formed far away from the laser spot where the temperature is not high enough for solid state transformation to occur, but instead their is enough time and temperature for the material to temper. This is a relatively small region where there is some decrease in the hardness observed.

- (ii) In the inter-critical region there is a mix of a martensite and austenite which cause a decreasing hardness.

- (iii) Large austenite grains are formed in the austenite further away from the laser source in both the thickness direction as well as the outer radius of the dot. They turned to austenite according to a displacive transformation called the 'austenite memory' principle. This is supported by the wavy grain boundaries since they are thought to be a result of the prior butterfly martensite wings. This means that the austenite grains formed have similar shape, size and orientation as the austenite created by the initial heat treatment [85, 86]. This effect was observed in previous research [80] as well as in research of material with similar composition such as in A. Alaei et al. [85]. The obtained reverse austenite grains have increased dislocation density compared to the initial austenite [43] which explains the higher hardness of the larger grains compared to the small grains which is contradicting the Hall-Petch relationship [58, 59].

- (iv) The small grains observed at the surface of the material are caused by recrystallization. The driving force of recrystallization is obtained by the stored energy of plastic deformation within the steel [81], since the reversed austenite has initially a high dislocation density [44]. Recrystallization is observed close to the surface where the highest temperature is achieved. Hence small grains grow in this area with significantly lower hardness due to the reduction in dislocation density as a consequence of energy minimization in the newly formed grains. The relation between hardness and dislocation density is intensively discussed in S. Graca et al. [82]. Since this is a process of nucleation and growth the newly formed grain boundaries do not include shapes from previous existing microstructures, hence showing straight boundaries [83].

The hardness values of the regions in the austenite in the single side laser treated specimen are comparable to the hardness values of the double side laser treated specimen. This suggest that the second laser pulse had not a noticeable effect on the recovery of austenite in the overlapping regions. The energy supplied by the second pulse is thus not enough for recovery or recrystallization in the middle of the sample and the displacive transformation was already finished by applying the first laser pulse.

In the double side laser treated specimen the difference between hardness of the top region and the middle regions is small, whereas for the single side laser treated specimen this difference is significant. Possible explanations are:

- For the single side specimens the indentations are taken closer to the surface, hence in a region with the smaller grains.

- Due to the second pulse there can be carbide precipitation in the austenite which was formed during the first pulse. The temperature in the middle of the sample is not sufficient for the growth of the new austenite grains, but is for carbides to form [87]. In the TM specimens a reduction in hardness of the line 1 (Figure 3.11) is observable which can be caused since carbide formation already took place during the tempering treatment. However, there is no evidence for this so further study is needed.

Tempering affects the hardness of the martensite but the hardness of the austenite remains the same, thus for the QM specimen a larger hardness gradient exist compared to the TM specimen which is represented in the hardness gap shown in Figure 3.11. This fact can have a consequence on the deformation behaviour of QM and TM discussed in Huang et al. [84]. A difference in microstructure and mechanical properties between two materials lead to different deformation behaviour and produce a significant deformation incompatibility. This incompatibility can be reduced by adding a interface layer which results in better distribution of strain for the QM specimens. In this research the intercritical region and tempered martensite can be thought of as the interface layer hence resulting in better distribution of strain. The TM specimen exhibit a larger inter-critical area compared to the QM and due to the smaller difference in mechanical properties less incompatibility in deformation is expected.

3.3.2. Effect of pattern topology on the deformation

From the DIC experiments it can be observed that strain partitioning takes place in the austenite dots during tensile deformation. This behaviour is similar to that observed in stochastic microstructure where higher local von Mises strain were obtained in the austenite grains compared to the martensitic ones [89]. Lee et al. [90], which studied a stochastic austenite/martensite structure, showed with the use of in-situ neutron diffraction measurements that three stages can be identified when the steel is tensile loaded:

- (i) The martensite and austenite both deform elastically
- (ii) The softer austenite grains deform plastically
- (iii) Both martensite and austenite deform plastically where the plastic deformation is concentrated in the softer austenite.

This behaviour is explained to be caused by the lower yield strength in combination with the much higher strain hardening of the individual austenite phase compared to the martensite. The much higher strain hardening of the austenite phase is partially due to the TRIP effect taking place in the material in which the volume of the created martensite is larger than that of the austenite [91]. The observation of the three stages made by Lee at al. [90] was confirmed by Dutta et al. [89] using DIC experiments for different strains during plastic deformation.

In this research this finding can also be supported and is explained according to Figure 3.19. In a) there is only little overall strain and no real partitioning takes place between the two phases because both phases most likely deform elastically. At higher strains such as in b) the strain clearly partitions in the austenite dots which can be assumed is caused by the plastic deformation in the austenite while the martensite still elastically deforms. Eventually in c) there is also strain localisation visible in the marentsite which would indicate that both the martensite and austenite plastically deforms but the plastic deformation is still concentrated in the softer austenite just as described by S. Lee et al. [90].

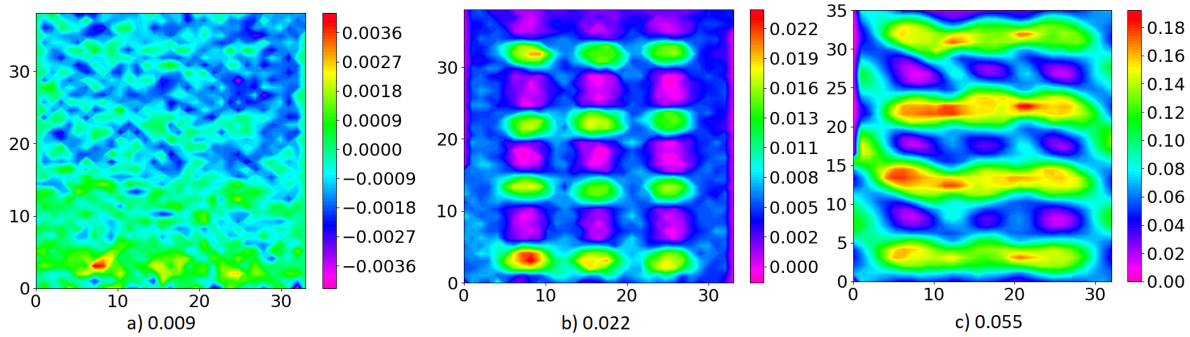


Figure 3.19: DIC results of QM-3 at a overall strain of a)0.009, b)0.022 and c)0.055

Due to the strain partitioning in the austenite dots, the TRIP-effect takes place during deformation as is shown in Figure 3.17a. The local strain in the austenite causes an exponential decrease in austenite fraction. In the case of no deformation already 2.5% martensite exist within the austenite, which can be caused by local decarburization [96] and large grains [97] which locally increases the martensite start temperature to ambient temperatures.

The difference in coefficients of Thermal Expansion (CTE) between the martensitic and austenitic phase after the laser treatment causes residual stress in the austenite contributing to the critical driving force for the martensitic transformation. Despite the high dislocation density in the bulk of the austenite, which makes it in principle stable, the big grains in combination with decarburiztion and the stresses due to the difference in CTE causes some parts of the austenite to transform into martensite without deformation.

In Figure 3.18 it is shown that with a strain of 0.042 the martensite mostly forms in the middle of the austenite. This is likely caused by the reduced austenite stability caused by the larger grains and increased stress due to difference in CTE compared to the grains at the surface [57, 60]. The fresh martensite forms at an angle of 45 °in the middle of the specimen as can be observed in Figure 3.18b. This is the result of the maximum shear stress taking place at this angle [92] in which the large shear component stimulates martensite formation.

The recrystallized area causes local reduction in strength [88] and also a reduction in grains size which results in a trade-off regarding austenite stability. The reduction of strength of the austenite causes less austenite stability, whereas the small grain size increases the stability [57]. From Figure 3.18 it seems that the mechanically induced transformation occurs more in the bulk of the specimen comparing to the surface, which could suggest that the reduction in grain size increases the austenite stability more than the reduction in strength decreases it.

At a strain of 0.042 the martensite formed is of a similar butterfly type as the martensite of the base material, however with increased strain to 0.162 the martensite observed is more of a continuous morphology like lath martensite and do not show similarities with the base martensite. This visual observed phenomena is confirmed by the microhardness of the in-

dividual phases. The TRIP-martensite at higher strains (0.162 for as-quenched and 0.180 for tempered) shows much higher hardness than the base material which suggests that a martensite type with a higher dislocation density than that of the base material is formed. Lath martensite is known to have higher dislocation density than butterfly martensite [98].

As the austenite further transforms to fresh martensite, the pattern and the matrix both are hard phases instead of having one soft phase. This causes strain partitioning in the martensite instead of only strain partitioning in the austenite. This difference is clearly observable in Figure 3.19b and c. Due to this change, strain partitioning bands are observed in the martensitic phase connecting the austenite dots. Two types of strain bands are observed in the martensite:

- Diagonal strain bands which connect the austenite dots with each other under an angle of 45°. The angle of 45°is thought to be the result of the maximum in plane shear stress which takes place at the 45°angle regarding to the loading direction in the uniaxial tensile test [92]. Since dislocation glide is the result of shear stress, the dislocations which were moving in the already plastically deformed austenite are moving first on the slip planes which are close to the maximum shear stress. This means that favourable oriented grains which require lower critical resolved shear stress transfer the dislocations first. These observations are in line with L. Patriarca et al. [93] which showed that the critical resolved shear stress required to yield at 45°is much lower than in other grains which causes high strain localizations in this direction.

- Horizontal strain bands which are thought to be the results of strain compatibility. If the austenite dots start to deform more than the martensite as mentioned earlier, the martensite between those deformed area's have to accommodate the shape change in the material. Since separation of crystallites does not occur, slip systems in the martensite will be activated hence creating strain partitioning bands between the austenite dots. The strain equilibrium between neighbouring grains is explained through the Taylor model and is known as the full constraint theory [94]. This theory is adjusted in order to obtain stress equilibrium stated by the Sachs model [95]. Normally the strain equilibrium is compensated on grain scale level, however since the strain partitioning is at much larger scale the compensation is thought to be on a higher scale as well explaining the horizontal strain partitioning bands.

The dotted diagonal pattern shows different strain partitioning compared to the dotted horizontal pattern. The horizontal strain band of the dotted horizontal patterns show more consistent partitioning in the martensite, whereas the diagonal bands experience less local deformation. This can be caused by the difference in diagonal distance between the dots. For the dotted diagonal pattern the diagonal distance is smaller than for the dotted horizontal pattern, hence interconnecting easier and showing more strain. Since it is harder for the dotted horizontal pattern to connect diagonally, the strain is partitioned more in horizontal direction.

The difference between the dotted diagonal pattern and the dotted horizontal pattern in terms of overall behaviour is negligible. Both materials have similar austenite content and similar sized dots. The interconnection between the austenite dots and thus the deformation in the martensite does not play a significant enough role to see difference in overall deformation behaviour.

For the patterned structures in general the difference in yield strength in the overall behaviour between the base materials and patterned structures is tested with the use of the rule of mixture.

$$\sigma_y^{Pattern} = \sigma_y^{Martensite} * V^{Martensite} + \sigma_y^{Austenite} * V^{Austenite} \tag{3.1}$$

The austenite percentage is 17% considering the gauge length of 25 mm and the constant diameter of 2.9 mm of the austenite dots. This result in predicted yield strengths of 988 MPa for QM and 781 MPa for TM. In Figure 3.13 it can be seen that this assumption gives a good prediction of the actual yield strengths. However the values are a bit underestimated which can be the result of not taking into account the increase in yield strength of the austenite due to hydrostatic stress caused by the surrounded hard phase.

The fracture behaviour of the specimens shown in Figure 3.16 confirms the strain localizations which is described by the DIC experiments. The initiation of the crack occurs normally at a material inhomogeneity such as the free edges of the material. Therefore the strain localization points at the free edges of the material are thought to be the initiation points of failure. After this initiation the crack propagation follows the bands with high strain which are also observed in the DIC experiments. The crack does not goes through the austenite dots although they appear to have the highest local deformation. A reason for this is that after the mechanically induced martensitic transformation the newly formed martensite has a higher strength than the initial QM in the matrix. Due to the TRIP-effect more deformation is possible within the dots.

3.3.3. Effect of phase strength

When comparing the QM patterned specimens with the TM patterned specimens it was observed that the strain in the austenite dots of the QM specimens were more localized whereas the strain in the dots of the TM specimens were more spread out in the martensitic matrix. Using the previously discussed reasoning it can be concluded that TM patterned specimens start yielding earlier than the QM patterned specimen causing earlier stage 3 deformation resulting in less distinguishable strain partitioning in the austenite. This also causes lower local strain values within the strain partitioning regions of the austenite.

Another important factor is the deformation incompatibility. Since the TM has less difference in mechanical properties with the austenite compared with the QM in terms of yield strength, tensile strength and deformation behaviour, less deformation incompatibility is expected in TM patterned specimens. This is also represented in the hardness maps where

the QM has a higher hardness gap compared to TM, suggesting more incompatibility between QM and austenite.

The stability of the austenite is dependent on the strength of the surrounding phase [50, 61], since the strength of the TM is significantly lower than QM some difference in transformation can be expected. However the results do not show a clear difference between the decrease in austenite fraction for the TM and QM. This can be due to the following two reasons:

- In most research the austenite grain is surrounded by the harder phase, whereas in this created microstructure the austenite grains are mostly adjoined to other austenite grains. After the austenite is partly transformed into martensite due to the instability of the austenite, the grains can again be surrounded by martensitic grains hence increasing the stability. In this behaviour it does matter if the base material is TM or QM since table 3.6 shows that the TRIP-martensite of the QM is harder than the TM at similar strains. It can be expected that the difference between transformation of austenite in QM and TM decreases at higher strains.
- In this research the local strain is compared to the martensite transformation, and in other researches it is more common to use the global strain due to the ease of measurements. Since there is difference in strain partitioning between QM and TM it is expected that local strain is achieved at different global strain, hence showing difference in martensitic transformation. However Figure 3.20 shows the relation between global strain and local strain in the austenite dots for both QM and TM base materials. The trendline for both the QM and TM are very similar suggesting that the martensitic transformation is very similar for local and global strains.

The analysis of the local deformation suggested that the TM samples has more homogeneous distributed strain, and the austenite deforms identical in the TM samples compared to the QM samples. This would suggest difference in local vs. global behaviour between TM and QM. However this difference is not observed when looking at Figure 3.20, where the behaviour looks similar. This could be caused due to the TRIP effect, which makes the strength en deformation of the newly formed martensite dictate the behaviour.

More information is needed to say more about the behaviour differences between QM and TM regarding austenite stability. Therefore it is advised that in further research more effort is done in obtaining information about the TRIP-effect in both the QM and TM in order to compare the effect of both phases on the austenite stability. XRD is advised to be used to determine phase fractions for more accurate results than obtained by OM analysis.

The microhardness results in table 3.6 show that the individual phases show strain hardening during deformation since an increased strain results in a increased microhardness. Results show that the austenite within the QM specimens experience more strain hardening (increase of 59 HV with a local strain of 0.162) than the TM (increase of 24 HV with a local strain of 0.180). This gives evidence of different strain hardening behaviour in the austenite of the QM compared to the TM. However further investigation of the stress-strain

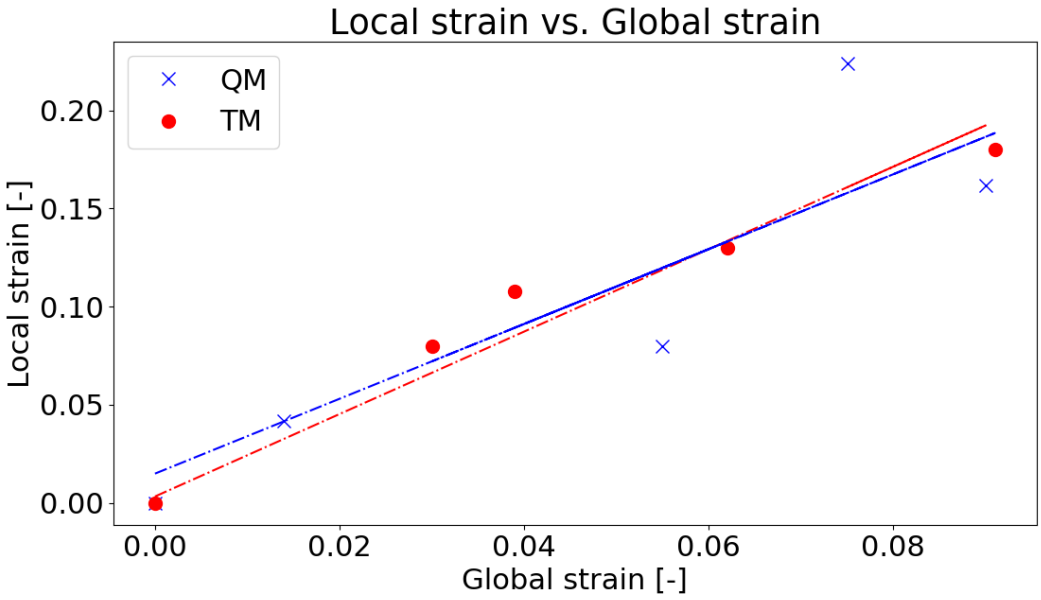


Figure 3.20: Local strain vs. Global strain

behaviour of the individual phases is needed to determine this behaviour and is not included in the scope of this research.

When comparing the overall deformation behaviour of QM patterned specimens with TM patterned specimens the strain of failure is comparable. Due to the higher strength of the QM, the QM specimens display much more toughness than the TM specimens. The similar strain to fracture can be explained according to the fracture behaviour observed. For both the QM and TM the fractures initiate at the outer region of the dot which suggest that the failure is caused in the intercritcal or tempered region in both the QM and TM. These regions do not differ much in both conditions, hence explaining the similar overall strain of failure.

4. Simulation experiments

4.1. Introduction

In this research a computational model is used to simulate the deformation behaviour of the Fe-Ni-C steel investigated in the experimental part. The simulations in this research serve two main purposes:

- (i) In the DIC experiments some limitation exist regarding the stress partitioning between the phases. By using simulations this behaviour can be investigated.

- (ii) After validation, simulations can help to better understand the behaviour of the architectured materials. This makes it easier to design favourable patterns in order to improve the mechanical properties, specifically the trade-off between strength and ductility.

The behaviour of the material is simulated using Crystal Plasticity Finite Element Modelling (CPFEM), which is used to describe plastic deformation in polycrystalline materials [102]. In the CPFEM method, single crystal plasticity model is incorporated into the FE framework to define constitutive relations at each integration point of the element. It is currently known to be best for prediction of microstructual and texture evolution during plastic deformation [103, 104]. Since this research relies on the prediction of the local behaviour of multi phase materials, the use of CPFEM is well suited [105]. In order for a CPFEM model to be efficiently used, a virtual microstructure is needed which is representative of the material and consist of a distribution of grains with particular orientation and morphologies. The intrinsic properties of the material are described with the use of characteristic model parameters which need to be calibrated.

4.2. Crystal plasticity simulations

4.2.1. Introduction to DAMASK software

The open source software package DAMASK [106] is used to perform CPFEM analysis. The software package uses a system in which at least three main files need to be defined:(i) the .geom file, (ii) the .load file and (iii) the material.config file.

Geometry file
The .geom file defines the distribution of the grains together with the overall geometry. In table 4.1 the parameters of the geometry are shown. A few additional comments regarding these parameters are made:

- The size is not included in the calculation of DAMASK and are for design purposes;
- The definition of the origin is optional;
- Homogenization is further defined in the material file.

After all these settings are defined, the grains are defined by sets of so called featureID's. These featureID's are placed in a matrix corresponding with the total number of grid points. Each number represents a grain with characteristics that are further defined in the material.config file. The program uses the defined size to make a 3D structure reading first the defined numbers on the x-axis, then the y-axis and finally the z-axis.

Table 4.1: Geometry file variables

Parameter	Example value	Description
Grid	a: 500, b: 250, c: 1	Defines the number of grid points in each direction
Size	x: 500, y:250, z: 1	Translation between grid points and physical sizes
Origin	x: 0 y: 0 z: 0	Defines the origin
Homogenization	1	Defines the homogenization index
Microstructures	1100	Defines the total number of grains

Load file
The load file defines the load applied to the volume element. The file may contain a number of consecutive load cases in which each load case corresponds to one line in the load file. For explanatory purposes two load cases are defined in the example below. The *fdot* is the deformation gradient rate in which the numbers are values in the tensor and the dots are variable tensor values which allows for volume preserving loads due to the set boundary conditions. Instead of *fdot*, it is possible to define other load cases such as the deformation gradient (F), the velocity gradient (L), and the Piola-Kirchhoff stress (P). After the *fdot* the stress is defined which is a tensor as well. These so called Mixed Boundary conditions need to fulfill three requirements:

1. Stress and Deformation boundary conditions are mutually exclusive;
2. The stress boundary condition must not allow for rotation, meaning the opposite off-diagonal element cannot have stress components at the same time;
3. If a velocity gradient is prescribed, each row of the tensors must either contain stress or velocity gradient.

When one of these conditions is not met, the simulation produces an error. It is very important to define the tensors in a correct way since they define the boundary conditions of the simulation. The load file described below is also the load case used for further simulations, if not state otherwise, and is recognized as the boundary conditions of a tensile load. Further variables in the load case prescribed are:

- *time*, which defines the total time in second for the load case;

- *incs*, which defines the number of increments in the load case. Linear time scaling is used so each increment takes $\frac{time}{incs}$ seconds;
- *freq*, which defines the frequency of the output. With *freq* 5 every five increments the output is obtained.

The total strain applied is also defined in this file. If the *fdot* variable is used, as is the case in this example file, the product of the *fdot* value and the total time define the maximum strain of the load case.

Below is an example of the load file input. Two rows are defined with different frequencies. A reason for this definition could be to have more data point in the first part of deformation (elastic region) to get a more accurate stress-strain curve.

Input

```
fdot 0.02 0 0 0 . 0 0 0 . stress . . . . 0 . . . 0 time 0.5 incs 50 freq 5
fdot 0.02 0 0 0 . 0 0 0 . stress . . . . 0 . . . 0 time 9.5 incs 475 freq 25
```

Material file
The material file defines the composition, microstructure and orientation distribution per material point which is a geometrical point describing the structure. Part of the file is written by DREAM.3D and a part need to be manually defined by the user. Five different sections need to be defined within the material file. The input is defined in table 4.2:

- homogenization: Allows for material point to describe an aggregate of constituents with different phases and/or crystallographic orientations. Due to homogenization it is possible to include multiple grains to a single material point. In this way texture can be applied to macroscopic scale simulations if needed. The *mech* command allows for the definition of the type of homogenization used for the mechanical fields at material points. Examples for this variable is *isostrain* or *RGC* (Relaxed Grain Cluster) which deals with how the grains on individual material points act towards each other (Voigt, Reuss or a combination of both) [110].
- crystallite: Defines the output parameters written by the simulation, however it is still possible to retrieve other output variables in later post-processing steps.
- phase: Defines the different phases using constitutive models defined by the users. In this section the material parameters need to be defined. Examples for constitutive laws describing plasticity are the phenomenological law and the dislocation density based law. The parameters which need to be defined with individual laws are further described in section 4.2.3.
- texture: Defines the texture of each individual grain defined by making use of Euler angles. The textures can be manually assigned to the grains. However while using DREAM.3D the texture defined in the statistical pipeline is implemented and texture for each grain is automatically generated.

- microstructure: Defines for each grain the output, the texture and the phase of the grain. In the microstructure section all the previously defined variables are assigned to material point or grains. The phase which is defined uses the parameters for the calculations of that grain. It should be noted that de number of the phase corresponds to the count of the inserted phase in the phase section, the same goes for the texture. The microstructure section is also automatically generated by DREAM.3D.

Table 4.2: Material file sections and variables

Section	Parameter	Example value	Description
Homogenization	mech	none, isostrain, RGC	Defines the homogenization scheme used
Crystallite	output	texture, f, p	Determines written output
Phase	See section 4.2.3.	-	Parameters defining constitutive laws
Texture	gauss	-	Spherical harmonical approximation of texture
	phi1	327.735	ϕ_1-Euler angle in degree
	Phi	54.082	Φ-Euler angle in degree
	phi2	196.517	ϕ_2-Euler angle in degree
	scatter	0.0	Angular scatter in degree
	fraction	1.0	Volume fraction of this texture component
Microstructure	phase	1,2,3	Defines the phase of the grain
	texture	1,2,3	Defines the texture of the grain from Texture section
	fraction	1.0	Volume fraction of the grain component

Calculations performed by DAMASK

The calculation performed by DAMASK are based upon continuum mechanics. The strain formulation of DAMASK is based on the assumption that a continuum body ($\mathscr{B}$) occupies region $\mathscr{B}_0$ in the reference configuration and $\mathscr{B}_t$ in the current configuration. The location of material point in the reference configurations is given by x and in a deformed configuration by y. The change in the current configuration on each reference point is then calculated with:

$$dy = \frac{\partial y}{\partial x}\, dx = \mathbf{F}(x)\, dx \tag{4.1}$$

In which ***F(x)*** is the deformation gradient which maps the line segment dx in the reference configuration to dy in the current configuration. In order to solve the partial differential equations to calculate the mechanical equilibrium, different solvers can be used such as Finite Element Method (FEM), Finite Volume Method (FVM), Finite Difference Method (FDM) and the Fast Fourier Transform (FFT) based spectral method. In this research the FFT spectral method is used in which the mechanical equilibrium equations are solved using fully implicit time stepping [111]. To calculate the stress response of the material points, decomposition of the deformation gradient in a elastic (e), plastic (p) and eigenstrain (i) part is necessary.

$$F = F_e\, F_i\, F_p \tag{4.2}$$

Where the evolution of the plastic gradient is given in terms of the velocity gradients (L_p) by the following flow rule:

$$\dot{F}_p = L_p F_p \tag{4.3}$$

Time integration from the kinematic quantities from t_0 to $t = t_0 + \Delta t$ is needed to obtain the plastic deformation gradient:

$$F_p(t) = F_p(t_0) + \int_{t_0}^{t} L_p(\tau) F_p(\tau) \, d\tau \tag{4.4}$$

To calculate the plastic behaviour of the material different constitutive laws can be used in order to include or exclude different phenomena. Normally it is a trade-off between accuracy and computational cost which influences the choice of the model. However the general principle in every model within plasticity is that the plastic velocity gradient L_p is determined as a function of the applied Mandel Stress M_p which is typically a non-linear relation. The plastic velocity gradient L_p is calculated as the sum over the individual shear contributions $\dot{\gamma}^\alpha$ on the systems α and is described by the following formula:

$$L_p = \sum_\alpha \dot{\gamma}^\alpha (\mathbf{s}_\mathbf{s}^\alpha \otimes \mathbf{n}_\mathbf{s}^\alpha) \tag{4.5}$$

with $\mathbf{s}_\mathbf{s}^\alpha$ and $\mathbf{n}_\mathbf{s}^\alpha$ being the unit vectors along the shear direction and shear plane, thus describing the Schmid factor of the system which relates the shear stress on the slip plane back to a global Mandel Stress by means of the orientation of the system.

In this research the main model used to determine the plasticity of the material is the phenomenological crystal plasticity model. Therefore, it is discussed in more detail in the upcoming sections by using the model description and formulas used in F. Roters et al [106].

Phenomenological crystal plasticity

The phenomenological crystal plasticity model is a model which was first described for slip in fcc crystals and later extended by introducing twinning. In DAMASK it is possible to implement twinning for all available crystal structures. The complex kinematics associated with dislocation generation and motion in this model are idealized as continuous crystallographic shears or slips, and the total slip on each system (rather than dislocation density) is used to correlate the evolution of hardening. The only driving force for slip is taken to be the resolved shear stress and all Non-Schmid phenomena such as diffusion and cross slip are not considered [112]. The plastic behaviour in this model is described in terms of the resistance ξ on both the slip N_s and twin systems N_{tw}. The resistance changes from an initial value ξ_0 to a saturation in which this change is formulated as followed for a slip system α

$$\dot{\xi}^{\alpha} = h_0^{s-s}(1 + c_1(f_{tw}^{tot})^{c_2})(1 + h_{int}^{\alpha}) \times \sum_{\alpha'=1}^{N_s} |\dot{\gamma}^{\alpha'}| \left|1 - \frac{\xi^{\alpha'}}{\xi_{\infty}^{\alpha'}}\right|^{a} sgn\left(1 - \frac{\xi^{\alpha'}}{\xi_{\infty}^{\alpha'}}\right) h^{\alpha\alpha'} + \sum_{\beta'=1}^{N_{tw}} \dot{\gamma}^{\beta'} h^{\alpha\beta'} \quad (4.6)$$

in which f_{tw}^{tot} is the total twin volume fraction, h_0^{s-s}, h_{int}, c_1 and c_2 are fitting parameters, ξ_{∞} is the asymptote for the resistance and h are the components of slip-slip and slip-twin interaction matrices respectively. The resistance can also be determined for the twin systems and is quite similar:

$$\dot{\xi}^{\beta} = h_0^{tw-s}\left(\sum_{\alpha=1}^{N_s} |\gamma^{\alpha}|\right)^{c_3} \sum_{\alpha'=1}^{N_s} |\dot{\gamma}^{\alpha'}| h^{\beta\alpha'} + h_0^{tw-tw}(f_{tw}^{tot})^{c_4} \sum_{\beta'=1}^{N_{tw}} \dot{\gamma}^{\beta'} h^{\beta\beta'} \quad (4.7)$$

with h_0^{tw-s}, h_0^{tw-tw}, c_3 and c_4 being model specific fitting parameters. The shear rate of a slip system is, as stated before, dependent on the slip resistance. This relation is given in the following formula

$$\dot{\gamma}^{\alpha} = (1 - f_{tw}^{tot})\dot{\gamma}_0^{\alpha}\left|\frac{\tau^{\alpha}}{\xi^{\alpha}}\right|^{n} sgn(\tau^{\alpha}) \quad (4.8)$$

And for twin systems the formulation is as followed

$$\dot{\gamma}^{\beta} = (1 - f_{tw}^{tot})\dot{\gamma}_0^{\beta}\left|\frac{\tau^{\beta}}{\xi^{\beta}}\right|^{n} H(\tau) \quad (4.9)$$

With $H(\tau)$ being the Heaviside or unit step function which is zero for negative values and one for positive values. f_{tw}^{tot} is the total twin volume fraction and is defined according to

$$f_{tw}^{tot} = max\left(\sum_{\beta=1}^{N_{tw}} \gamma^{\beta}/\gamma_{char}^{\beta}, 1.0\right) \quad (4.10)$$

Where γ_{char} is the characteristic shear due to mechanical twinning which depends on the twin system. When the strain rate is determined the velocity gradient can be calculated according to the laws of plasticity used and defined earlier by equation (4.5).

4.2.2. Description of the RVE

The Representative Volume Element (RVE) is regarded as a volume of a heterogeneous material that is sufficient large to be statistically representative for the structure analysed [108]. The description of the RVE consist of two primary steps: (i) the selection of the geometry which can represent the structure analysed, and (ii) the implementation of the RVE in the used computational model. Both steps will be discussed in detail in this section.

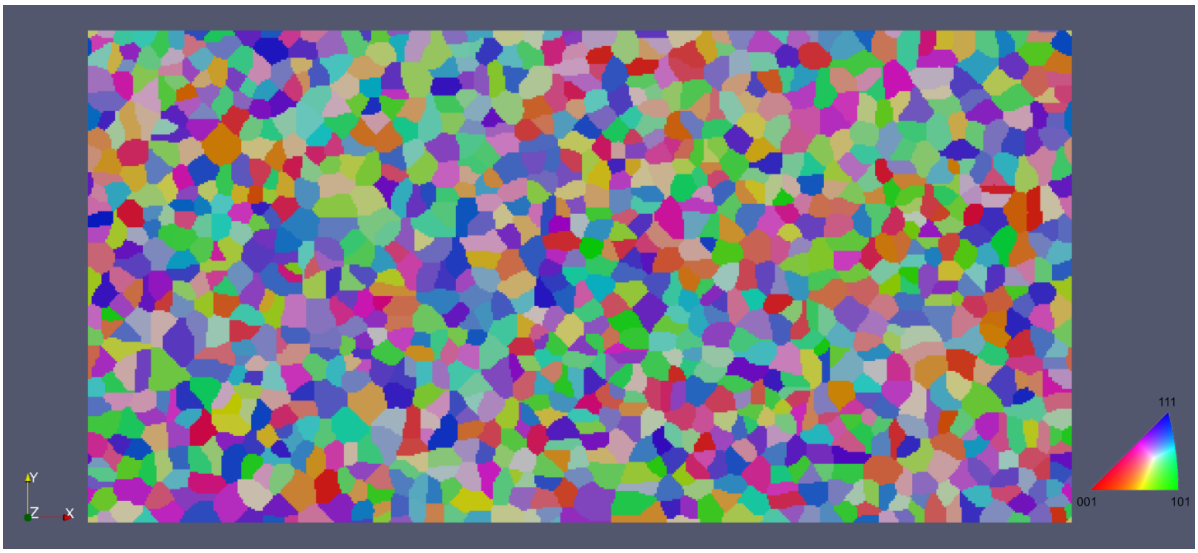


Figure 4.1: Microstructure used for simulating large structures including crystallographic orientations of each grain

Geometry of the RVE

The microstructures and architectured patterns used for the simulation are discussed in this section. These microstructure are created by using DREAM.3D [107] in combination with the visualisation tool Paraview [109]. Using DAMASK simulations the dotted diagonal pattern and the dotted horizontal pattern are examined. In addition a line pattern of austenite created in a (tempered) martensitic matrix is also simulated as the DIC data was obtained in previous research. The RVE is kept in 2D since full penetration of the austenite phase is assumed, hence there is no difference in the z-directions and saves up considerably in computational time. A 3D simulation is performed as well in order to validate that this difference is negligible.

RVE for material parameter calibration

A RVE is created in order to calibrate the base materials according to their experimentally obtained stress-strain curves. This RVE consist of 1200 grains with a random texture as is shown in Figure 4.1. Since a high number of grains is used, the texture should not influence the obtained stress-strain curves and hence the resulting calibrated material parameters can be used for further simulation. This RVE consist of only one phase and can easily be created using DREAM.3D.

RVE for pattern simulation

The simulations are split up in two different sections:

- The RVE is kept small and the austenite fractions is significant in order to properly evaluate the initial response of the simulation.

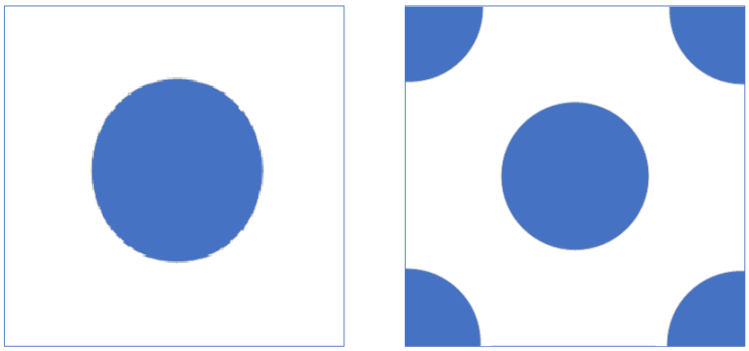


Figure 4.2: RVE for the dotted horizontal pattern (left) and dotted diagonal patter (right)

  - A line structure is used in which approximately one third of the RVE (which consist of 91 grains) is austenite and the rest is martensite. This line structure is used to validate the behaviour of the simulation with the use of the experimental DIC results obtained in previous work [80].
  - Both a single dot and a FCC unit cell (Figure 4.2) is created in which again approximately one third of the RVE (which consist of 200 grains) is austenite and the rest is martensite. These structures represent the dotted horizontal pattern and dotted diagonal pattern respectively due to the periodic boundary conditions of the FTT spectral solver.

- A larger scale where the structures are displayed as in the experiments. It uses the same base microstructure as described for the calibration of the material parameters (Figure 4.1) which consist of 1200 grains with a random texture from which every patterned structure is created. The total austenite area is kept around 7% for all simulations by calculation the area of the dots and the line. The area of both the dots and the line are extracted in paraview to identify the grains within these area's. Than the grains are manually changed to be the austenite phase in the material.config file in the *microstructure* section.

Creation of the RVE

The RVE need to be created such that it can be directly implemented in DAMASK. Therefore the .geom file and part of the the material.config file is created using the open source software package DREAM.3D [107]. It creates the files to be used in DAMASK, while leaving sections open for the user to additionally define. DREAM.3D allows for the creation of microstructures of user defined sizes, and generates grains including pre-defined texture. It is also possible to implement EBSD data obtained from experiments to generate an accurate representation of the texture using the software.

A limitation for its usage in this research is the statistical random distribution of different phases whereas in this research a predefined phase distribution is needed. However, in order to overcome this problem, a single phase material is created after which the desired grains are identified using Paraview [109] and manually altered in the material.config file.

The output of the program consist of a microstructure consisting of grains with statistically defined sizes and textures in a DAMASK format (if desired). This format of the RVE needs be complemented with the model parameters and description of the used setting as described earlier.

4.2.3. Selection of the model parameters

For the calculation performed by the DAMASK software to be representative, the parameters within DAMASK need to be defined correctly. They are defined such that a structure with a random texture fits with the stress-strain curve from the experiments obtained. In this section the parameters of de phenomenological model are discussed.

Parameters Phenomenological model

The input parameters in the phenomenological model are defined the <*phase*> part of the material.geom file. This section shows the different parameters needed for the phenomenological model and are displayed in table 4.3.

It is assumed that, within the martensite, slip is the only deformation mechanism which takes place, while for austenite twinning is additionally added as compensation for the underestimation of hardening due to exclusion of the TRIP-effect. The exclusion of twinning in the martensite is achieved by inserting zero in the parameter for the amount of twin systems. DAMASK has for every lattice structure supported its own set of slip systems implemented in the calculations.

h0_slipslip, *h0_twintwin*, *h0_twinslip* and *h0_sliptwin* are interaction coefficients between slip/twin systems. They are determined by fitting the stress-strain curve from experimental data using the RVE for calibration. The values can initially be approximated and a range can be determined before the fitting. A script is then used which uses the ranges from the selected parameters and fit the data from the experiments. This script uses an algorithm which makes iteration to reduce the error value as much as possible for the simulated stress-strain curve when compared to the experimental curve. This should result in a simulated stress-strain curve which fits with minimal error on the experimental data.

Some parameters do not show a description in table 4.3, since their physical meaning could not be traced and their influence is negligible. These unknown parameters are based on previous simulations performed with DAMASK.

4.2.4. Alternative simulation setups

As will be later showed in the results and discussion, some configuration did not lead to the expected results according to the experiments. Figure 4.3 show alternative approaches which were considered in order to overcome the limitations observed.

Dislocation density based crystal plasticity model

The dislocation density based crystal plasticity model include microstructural properties. It includes Twinning Induced Plasticity (TWIP) as well as Transformation Induced Plasticity (TRIP) for fcc metals. This could include the strain difference in the austenite which is

Table 4.3: Simulation parameters for phenomenological model

Parameter	Example value	Description
plasticity	phenopowerlaw	Law for plasticity
elasticity	hook	Law for elasticity
lattic_structure	bcc	DAMASK considers: bcc, fcc, hex, bct
ca	1	Ratio of c and a from crystal structure
Nslip	12	Number of slip systems
Ntwin	0	Number of twin systems
c11	133e9	Elastic constant c11
c12	85e9	Elastic constant c22
c44	106e9	Elastic constant c44
gdot0_slip	0.001	-
n_slip	20	Exponent in equation 4.8
tau0_slip	300e6	Hardening parameter
tausat_slip	530e6	Hardening parameter
gdot0_twin	0.001	-
n_twin	20	Exponent in equation 4.9
tau0_twin	31e6	Twinning parameter
s_pr	0	Twinning parameter
twin_b	0	-
twin_c	0	-
twin_d	0	-
twin_e	0	-
h0_slipslip	4e10	Interaction between slip systems
h0_sliptwin	0	Interaction between twin and slip systems
h0_twinslip	0	Interaction between twin and slip systems
h0_twintwin	0	Interaction between twin systems
interaction_slipslip	1 1 1.4 1.4 1.4 1.4	Interaction coefficients slip
interaction_sliptwin	1 1 1 1 1 1	Interaction coefficients slip and twinning
interaction_twinslip	1 1 1 1 1 1	Interaction coefficients slip and twinning
interaction_twintwin	1 1 1 1 1 1	Interaction coefficients twinning
a_slip	2.0	-
atol_resistance	1	Convergence tolerance

neglected by using the phenomenological model. The parameters needed for this model are shown below. These parameters are obtained from literature or calculated using simple models. Several adjustment parameters are present as can be seen in the comments behind the parameters. The dislocation mean free path is adjusted in order to change the hardening behaviour of the material until it fits the austenitic stress-strain curves obtained by experiments. For the tests with the dislocation density approach the martensite in the RVE uses the phenomenological model since it is a bcc structured phase and hence does not include the TWIP or TRIP effect.



Figure 4.3: Scheme of different simulation routes to overcome limitations in the used simulation

A drawback for the use of the dislocation density based crystal plasticity model is that a lot of extra parameters are needed which can be acquired from literature, experiments or simulations The model is also computational very demanding compared to the phenomenological model.

Input

```
[FCC_Austenite]

elasticity          hooke
plasticity          dislotwin

### Material parameters ###
lattice_structure     fcc
C11                   133.0e9
C12                   85.0e9
C44                   106.0e9
grainsize             4.4e-5        # Average grain size [m]
SolidSolutionStrength 6.74e6        # Strength due to elements in solid solution

### Dislocation glide parameters ###
Nslip               12
slipburgers         2.5399e-10      # Burgers vector of slip system [m]
rhoedgedip0         1.0             # Initial dislocation density [m/m3]
rhoedge0            7.6e12          # Initial dislocation density [m/m3]
v0                  4.696e-6        # Initial glide velocity [m/s]
```

```
Qedge               3.5e-19         # Activation energy for dislocation glide [J]
p_slip              1.0             # p-exponent in glide velocity
q_slip              1.0             # q-exponent in glide velocity

# hardening of glide
CLambdaSlip         23.0            # Adj. parameter controlling dislocation mean free path
D0                  4.9e-5          # Vacancy diffusion prefactor [m2/s]
Qsd                 4.7e-19         # Activation energy for climb [J]
Catomicvolume       1.0             # Adj. parameter controlling the atomic volume [in b]
Cedgedipmindistance 1.0             # Adj. parameter controlling the minimum dipole distance [in
atol_rho            1.0
interaction_slipslip 0.122 0.122 0.625 0.0454 0.137 0.122  # Interaction coefficients

### Twinning parameters ###
Ntwin               12
twinburgers         1.466e-10       # Burgers vector of twin system [m]
twinsize            5.0e-8          # Twin stack mean thickness [m]
l0_twin             442.0           # Length of twin nuclei in Burgers vectors
maxtwinfraction     1.0             # Maximum admissible twin volume fraction
xc_twin             1.0e-9          # critical distance for formation of twin nucleus
VcrossSlip          4.9155e-27      # cross slip volume
r_twin              10.0            # r-exponent in twin formation probability
Cmfptwin            1.0             # Adj. parameter controlling twin mean free path
Cthresholdtwin      1.0             # Adj. parameter controlling twin threshold stress
interaction_sliptwin 0.0 1.0 1.0    # Dislocation-Twin interaction coefficients
interaction_twintwin 0.0 1.0        # Twin-Twin interaction coefficients
atol_twinFrac       1.0e-7
SFE_0K              0.074           # stacking fault energy at zero K
dSFE_dT             0               # temperature dependance of stacking fault energy
```

Homogenization

In order to see if strain partitioning in the austenite takes place, homogenization schemes are used. It contains material points at which each material point contains eight grains. In this way a larger structure of grains can be implemented. The first simulation is done using the isostrain assumption which state that all constituents comprising a material point are subjected to the same deformation. This is considered as a possible reason for the lack of strain partitioning. The second homogenization scheme is the Relaxed Grain Cluster (RGC) in which two parameters (the over-proportionality and scaling parameter) govern the ratio between equal strain and equal stress assumption mentioned by Voigt and Reuss [110]. Simulations with these parameters using different orders of magnitude are performed to see an isostress, an isostrain and a combined situation.

Different boundary conditions

While using the FFT approach, automatic periodic boundary conditions are applied. These can cause the behaviour of the strain in the material to be different than when free surfaces are used. T. Maiti et al. [125] did a simulation using the FFT approach while creating free surfaces using two approaches: (i) by adding a very elastic material ($C_{11} = 0.1$, $C_{12} = 0$ and $C_{44} = 0.05$) and adding a Dilatational conditions. Python is used in order to add both ap-

proaches to the calculation, however some convergence problems arise using the simulation and therefore no reasonable output was obtained.

Change in load file
In the load file *fdot* is applied, which is the deformation gradient rate, for all cases investigated. It is not defined on which material points *fdot* is applied. Therefore, it is thought that every material point has the same deformation gradient rate. This can be close to the truth in cases where the phases have a stochastic distributed, however since clear distinction is made between the phases in the form of a line structure this assumption can be inaccurate. To check this, different conditions are varied as input in the load file: (i) the deformation gradient, (ii) stress, (iii) velocity gradient. In order for these load files to converge, multiple lines need to be constructed within the load file in which each line represents one increment. It should be tested what step size can be used in order to let the simulation converge, for the stress case this was for example 10 MPa per load case.

Solver
In this research the FFT spectral solver is used to calculate the partial differential equations, however DAMASK allows for FEM solver to be applied using Abaqus. In Abaqus the boundary conditions can be defined per material point which is not allowed for the FFT spectral solver. In order to apply the microstructure to Abaqus an so called UMAT file need to be defined. In this file the mechanical response of the material is defined such as in the *phase* part of the material file in the FFT spectral solver.

Over exaggeration of the hard phase
In order to validate some hypothesis made regarding the handling of the material points, the martensitic phase is altered to obtain an extremely hard phase with very low strain. This is done by putting the yield strength and UTS unrealistically high to see the behaviour of the material. All the parameters of the martensite were kept the same except the *tau0_slip* which was increases to 5000 MPa and *tausat_slip* which was increased to 7000 MPa.

4.3. Results & Discussion

4.3.1. Parameter definition
All parameters need to be obtained either by: (i) literature, (ii) determine according to the base materials stress-strain curve, or (iii) by using a fitting algorithm. The results of the parameters for the phenomenological model are shown in table 4.4.

Martensite
With the use of literature it is shown that for bcc material only the six slip planes of type {110} are implemented since they require the least energy to be activated. Those six slip planes all have two [111] directions [113] which results in a 12 different slip systems which

Table 4.4: Simulation parameters for QM, TM and austenite

Parameter	**QM**	**TM**	**Austenite**
plasticity	phenopowerlaw	phenopowerlaw	phenopowerlaw
elasticity	hook	hook	hook
lattic_structure	bcc	bcc	fcc
ca	1	1	1
Nslip	12	12	12
Ntwin	0	0	12
c11	133e9	133e9	133e9
c12	85e9	85e9	85e9
c44	106e9	106e9	106e9
gdot0_slip	0.001	0.001	0.001
n_slip	20	20	20
tau0_slip	300e6	300e6	68e6
tausat_slip	530e6	370e6	330e6
gdot0_twin	0.001	0.001	0.001
n_twin	20	20	20
tau0_twin	31e6	31e6	68e6
s_pr	0	0	330e6
twin_b	0	0	0
twin_c	0	0	0
twin_d	0	0	0
twin_e	0	0	0
h0_slipslip	4e10	4e10	9e8
h0_sliptwin	0	0	3.3e8
h0_twinslip	0	0	5.3e8
h0_twintwin	0	0	1e9
interaction_slipslip	1 1 1.4 1.4 1.4 1.4	1 1 1.4 1.4 1.4 1.4	1 1 1.4 1.4 1.4 1.4
interaction_sliptwin	1 1 1 1 1 1	1 1 1 1 1 1	1 1 1 1 1 1
interaction_twinslip	1 1 1 1 1 1	1 1 1 1 1 1	1 1 1 1 1 1
interaction_twintwin	1 1 1 1 1 1	1 1 1 1 1 1	1 1 1 1 1 1
a_slip	2.0	2.0	1
atol_resistance	1	1	1

represent the parameter *Nslip*. The elastic constants C_{11}, C_{12} and C_{44} of the austenite phase in a similar Fe-Ni-C steel can be found in [116].

The two hardening parameters *tau0_slip* and *tausat_slip* are approximated with the use of the stress strain curves of the base material from both as-quenched and tempered martensite. Figure 4.4 shows the initial stress-strain curve of austenite for visualization of the in-

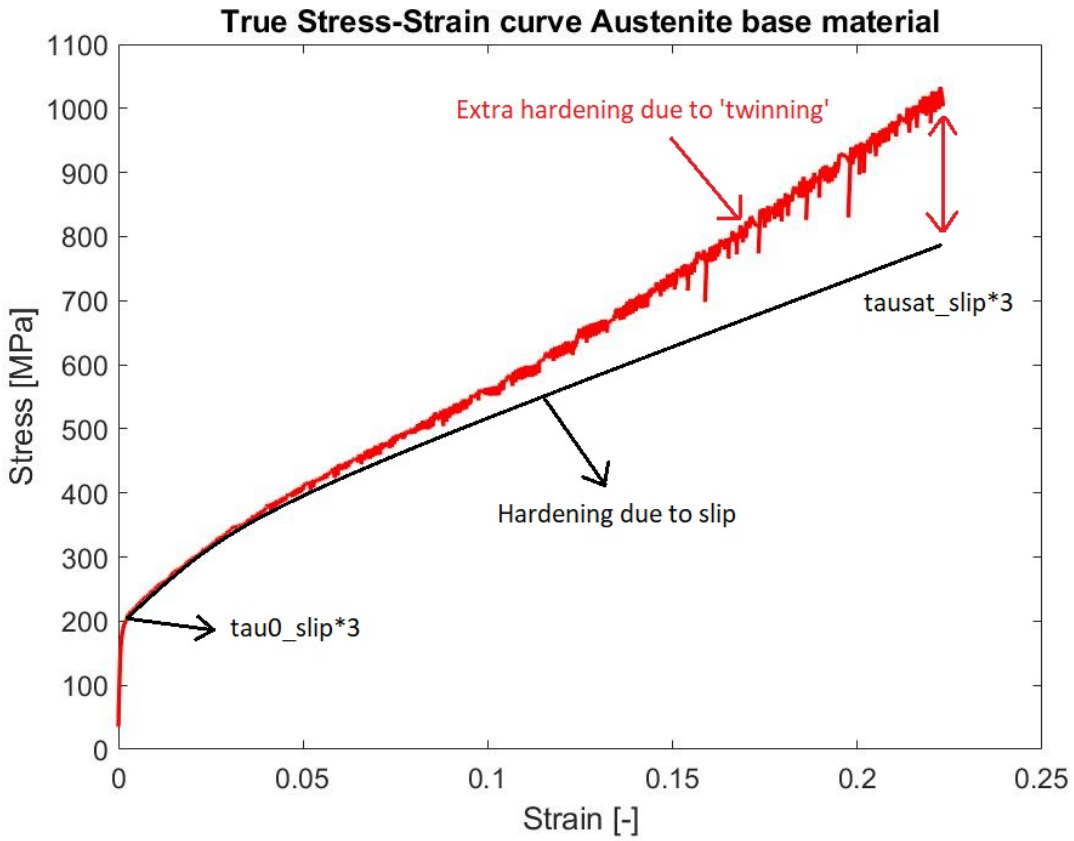


Figure 4.4: Visual interpretation of some parameters in the phenomenological model

terpretation of the parameters. Both *tau0_slip* and *tausat_slip* show a clear definition. The parameter *tau0_slip* is one third of the yield point obtained in the initial base material, and the parameter *tausat_slip* is one third of the UTS of initial base material. Therefore these parameters can be easily determined, for the TM the UTS can be extracted from the experimental curve whereas for the QM the experimental curve need to be extrapolated for the determination of the UTS since the material fails before reaching it.

h0_slipslip is defined as the interaction between two different slip systems, and determine the hardening rate which is represented by the slope of the plastic part of the stress-strain curve. An increase in the *h0_slipslip* increases the slope and therefore the hardening in the material. The exact value of this parameter is obtained with the use of the fitting algorithm.

Austenite

The austenite has additional twinning in order to compensate for the the hardening due to twinning and the TRIP-effect. Hence some additional parameters need to be obtained. For the austenite both *Nslip* and *Ntwin* need to be defined for the fcc lattice. For the slip this results in 12 different slip systems since every fcc has four {111} planes which all have

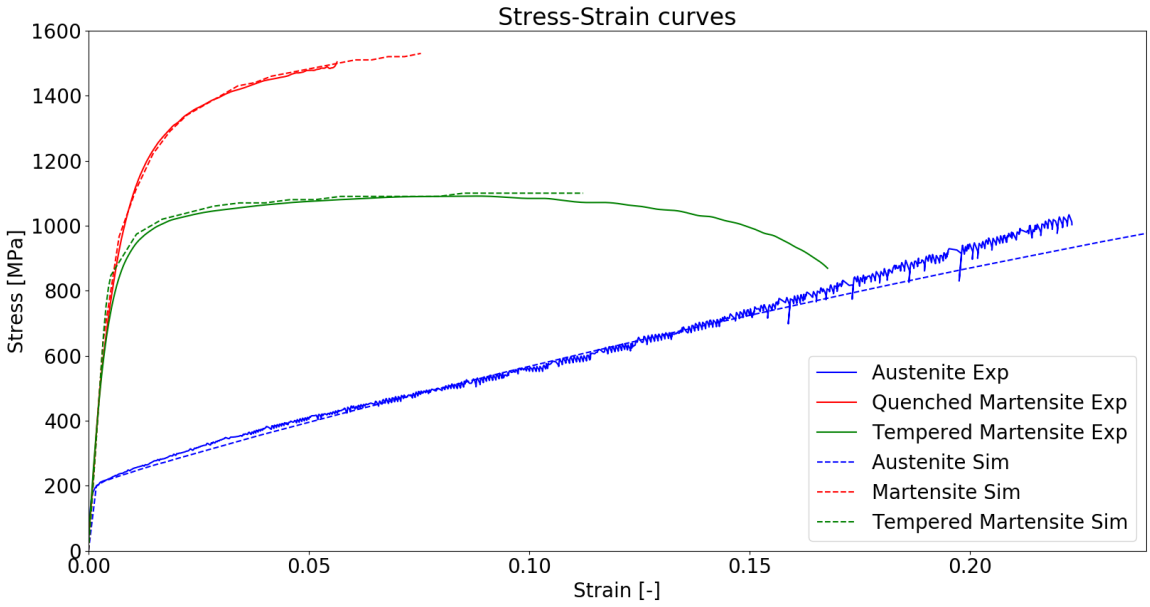


Figure 4.5: Stress-strain curves simulated of the base material in comparison with the experimental curves

three different [110] directions [114] and 12 different twin systems as well since there are four {111} planes each containing three different [112] directions [115]

The parameters describing twinning are similar compared to the parameters describing slip. *tau0_twin* is defined as one third the strength at which twinning starts and *h0_twintwin* is the interaction between twin systems and determines the slope of hardening due to twinning which is fitted using the script along with the *h0_slipslip* parameter in austenite. In contrast to slip there is no saturation value defined for the twinning, however a push up factor can be used and is defined as *s_pr*. This parameter can be expressed as approximately the difference in strength between the saturation of slip and the tensile strength defined in the stress-strain curve as displayed in figure 4.4. The values *h0_sliptwin* and *h0_twinslip*, which are describing hardening caused by the interaction between slip systems and twin systems, do not have a significant influence on the final result of the stress-strain curve. All these additional parameters result in the definition of austenite

4.3.2. Parameter calibration

The results of the calibration simulations are shown in figure 4.5 in which the dotted lines are the simulated stress-strain curves whereas the straight lines are obtained from experiments from previous research. All experimental stress strain curves are displayed in true stress and true strain values [117] whereas the simulated data is in equivalent von Mises stress and strain. However since there is an uni-axial loading those values can be compared.

First the result from the austenite will be compared. The stress-strain curve of austenite consist of both hardening due to slip and hardening due to twinning. The experimental result shows that an almost linear hardening of the material takes place after yielding. The

simulated stress-strain curve follows up on the experimental curve until a strain of around 0.16, after which the simulated curve shows reduced hardening behaviour whereas the experimental curve remains linear. This is however limited at the maximum strain within the austenite to a difference in stress of around 50 MPa. If higher strains are reached and the data is extrapolated the deviation is expected to be larger.

The phenomenological model used to simulate the behaviour of the austenite does not include physical phenomena such as stress induced martensitic transformations, whereas in the austenite experiments this does takes place. The error caused by this is reduced by adding extra twinning to the simulation. Moreover, the stress-strain curve of the austenite is of the microstructure after applying the salt bath on 1173K. However it is shown that the strength and dislocation density in the austenite increases due to the reverse austenization, as discussed in section 1.2.5. Therefore the stress-strain curve can underestimate the strength of the austenite and the higher dislocation density can also cause the strain to be overestimated. It is advised for future research to apply the heat cycle from the laser treatment to the material so a more representative stress-strain curve can be obtained for the austenite.

For both the QM and the TM the simulated curves fit really well with the experimental curves. For the TM the curves are not fitted after the ultimate tensile strength (UTS) since in the simulation necking is not included and hence no softening phenomena after UTS take place. The experimental values for the TM are also not measured with reduction in area, therefore the curve after UTS is not reliable.

The QM was subjected to brittle fracture so no UTS is reached hence the simulation can continue to higher stress than in the experiments. No failure mechanisms are included in the simulated curves which causes them to go asymptotically to a value near the UTS for different materials. This makes it possible for the simulations to reach strains at which normally the material is already broken, hence caution should be applied by comparing strain values much higher than the strain at the UTS of the experimental determined curves.

4.3.3. Small scale simulations

Line pattern microstructure
In order to validate the behaviour of a heterogeneous architectured structure using simulation, a simple case of a single austenite line in a quenched martensite matrix was simulated using DAMASK and compared to the experimentally obtained strain behaviour from previous research. The experiments show a clear partitioning of strain in the austenite as is shown in Figure 4.6.

In Figure 4.7 the stress and strain partitioning is shown as a result of the simulation in which the top of the figure shows the strain partitioning and the bottom shows the stress partitioning. Both the experimental and the simulated results were objected to a load in the

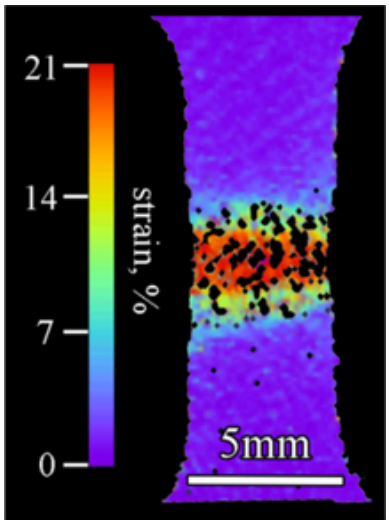


Figure 4.6: DIC results line pattern previous research [80]

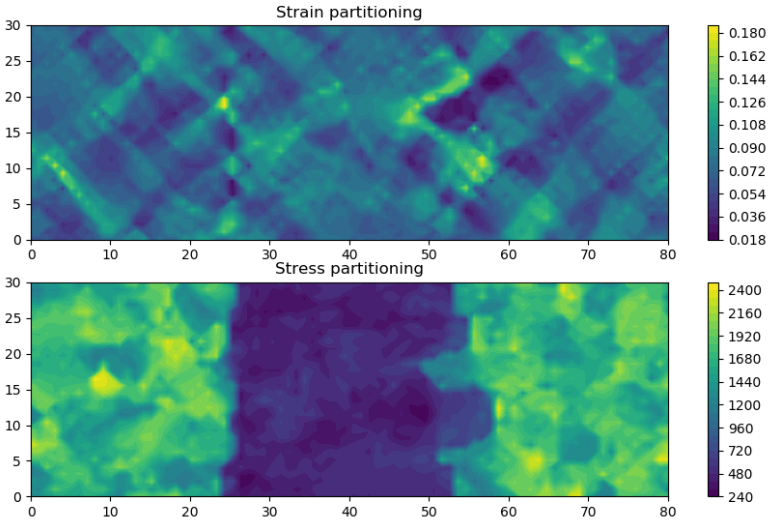


Figure 4.7: Stress and strain partitioning simulation line pattern

direction of their longest axis and are therefore comparable. Figure 4.7 shows no strain partitioning within the austenite, whereas a clear stress partitioning does take place within the martensite. The experimental results of partitioning of stress to the harder phase within a microstructure, consisting of a hard and soft phase, is reported intensively [118–121], these papers also support the experimental obtained results in which the strain partitions in the soft phase (in this case the austenite).

In order to overcome this lack in strain partitioning observed in the simulations, the additional configurations were applied:

- The usage of the dislocation density model including the TRIP-effect give similar results as obtained with the phenomenological model. This can be explained since the stress-strain curve is fitted in the same way as in the previous model. Extra strain in the austenite was expected due to including the TRIP effect, however changing the values of the Stacking Fault Energy (SFE) (governs the TRIP effect in the equations used by the simulations) did not change the behaviour of the material. This is most likely caused by the fact that the TRIP effect is included for ϵ-martensite transformations instead of α-martensite transformations within DAMASK. The SFE is the driving force for the ϵ-martensite transformation and needs to be significantly low [122, 123] which is true for steels with Manganese content of around 15%. Due to the high Nickel content of the steel used in this research the SFE (calculated accordig to D.Q. Xun et al. [124]) is way to high for this transformation to take place.

- For the homogenization and change in load file the results of the simulation does not show any difference within the strain partitioning behaviour of the austenitic region. The isostrain and isostress situation used with homogenization schemes only apply for the grains within material point and not for the material points between each other. Hence explaining why this does not lead to strain partitioning.

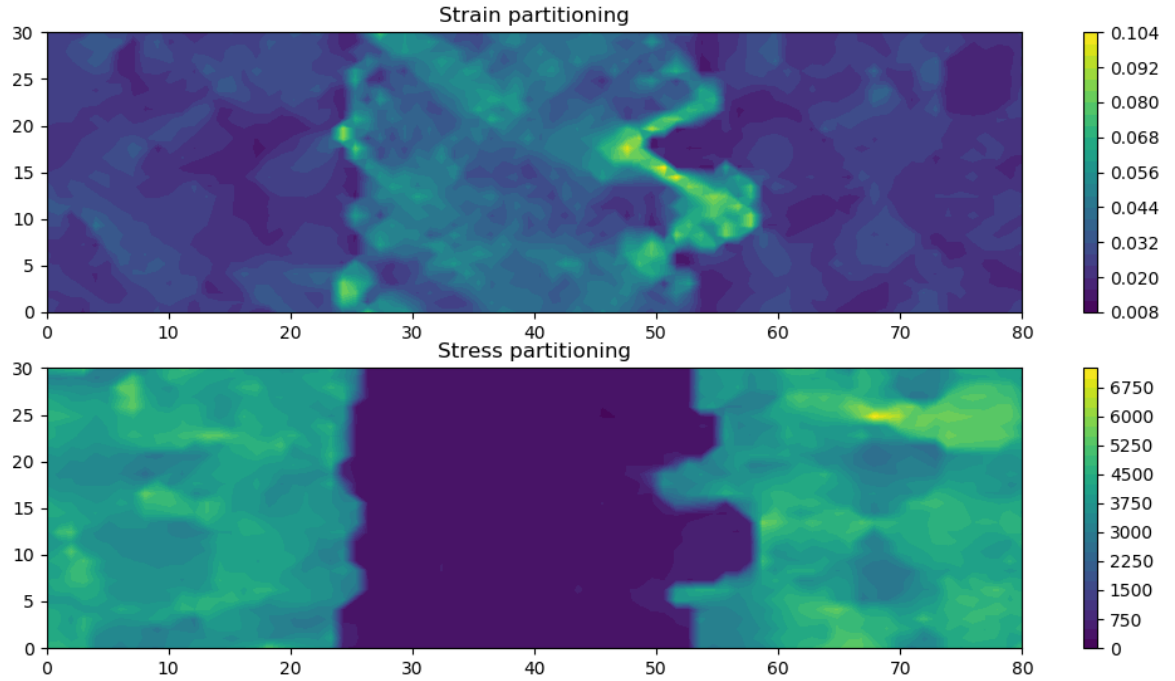


Figure 4.8: Stress and strain partitioning behaviour of a line pattern with an over exaggerated hard phase

- For the configuration with a change in solver, no partitioning of either stress and strain took place in the different phases. The grains defined in the RVE were not distinguishable.
- The changes made in the boundary conditions did not converge, due to limitations in the time of the research conducted it was not possible to investigate this method any further. For further research this can be something to look into, since in the paper written by Maiti et al. [125] promising results with similar applications were shown.
- The over exaggeration of the strength of the hard phase shows results of an overall strain of 4% which are displayed in Figure 4.8. A clear partitioning in strain is now visible which causes the assumption of equal deformation gradient rate to be untrue. The stress partitioning which was visible in previous simulations still exist.

Despite a lot of effort has been made to improve the model to include strain partitioning, none of the methods show direct success or improvement. Hence for further analysis the model description without these configuration is used for its simplicity.

Circular patterned microstructures

Besides the deformation of the line structure, the deformation of the circular patterns are also evaluated. This is done by making a RVE for both cases as can be seen in Figure 4.2. Since periodic boundary conditions are applied in the FFT spectral solver, these patterns are continuously repeated and hence these structure represent both the dotted diagonal pattern and the dotted horizontal pattern. Due to this argumentation this is the computa-

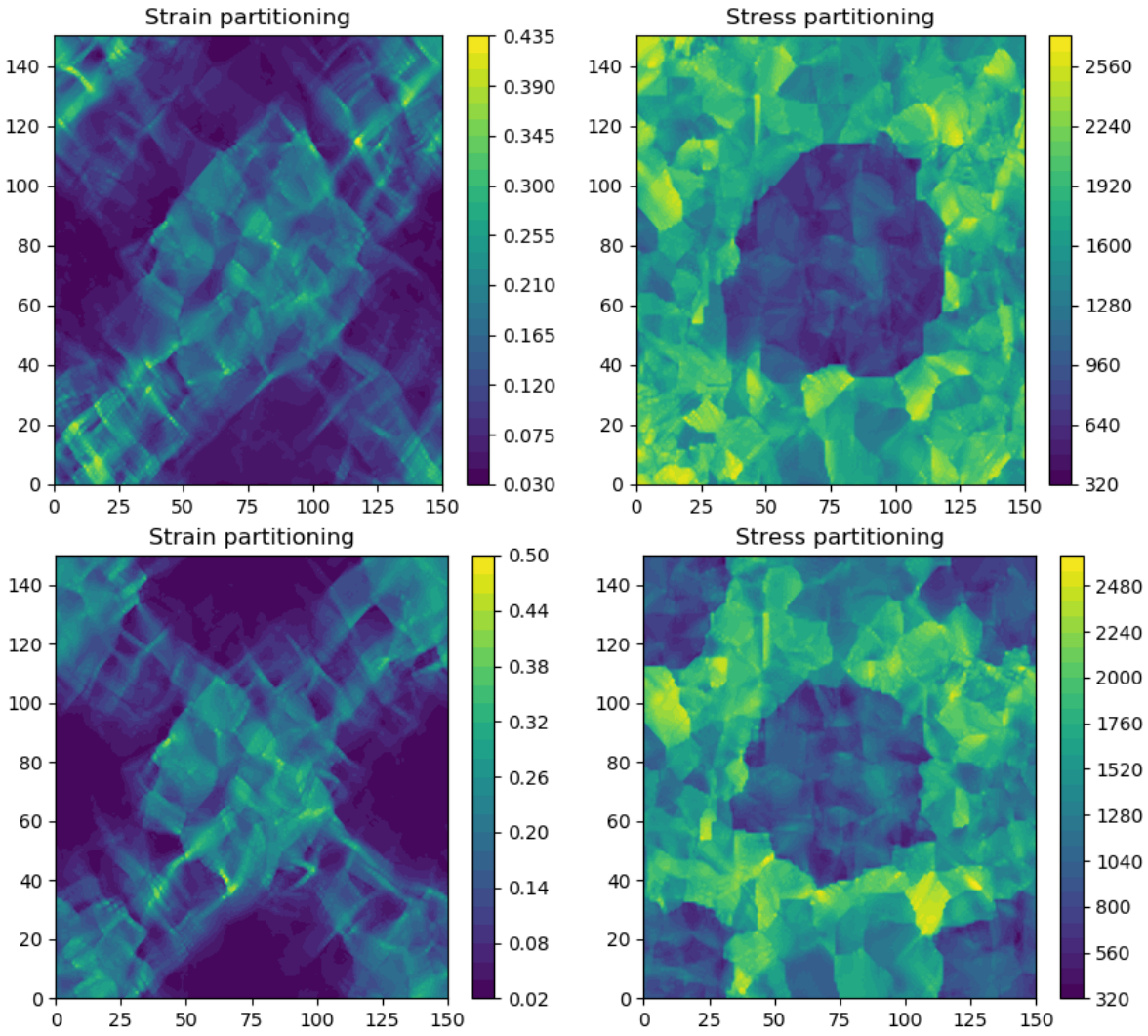


Figure 4.9: Stress and strain partitioning behaviour of a dotted horizontal pattern (top) and dotted diagonal pattern (bottom)

tionally most efficient way to calculate the behaviour of both patterns. For the input of the simulation the same material file is used as for the initial calculations of the line structure, thus the material files before checking the alternative simulation set-up.

In figure 4.9 the results of the stress and strain partitioning in the simulations are shown. In contradiction with the line structure a strain partitioning within the austenite is visible in both cases. The austenitic dot is clearly visible and strain partitions with an X shape through the dot to every corner, hence when periodic boundaries are applied the dots are interconnected with each other by means of diagonal bands.

The X pattern is assumed to be caused by the maximum in plane shear strain which is under approximately 45°compared to the tensile direction [92]. The maximum in plane shear strain takes place in all direction relative to the loading direction hence creating a X pattern which is observed in the simulations. Dependent on the orientation of the grains the strain partitioning can be more or less in each of those four directions.

For all conditions small difference between the martensitic stresses can be observed, which are caused by the texture of the material. Some grains have a lower Schmid factor and therefore contain more stress to overcome the critical resolved shear stress thus creating stress partitioning between grains [126].

Comparing both patterns, there is not much difference in the case of strain partitioning. The dotted diagonal patterns has slightly higher values for the strain within the austenite and in the area of the X shape, whereas the other areas of martensite have lower strain values in case of the dotted diagonal pattern.

The difference in stress partitioning is obvious, the high stresses partition only within the martensitic grains, whereas in the austenitic grains only relatively low stress is observed. The difference between the dotted diagonal structure and dotted horizontal structure is therefore within the distribution of the austenitic phase.

4.3.4. Large scale simulations

In order to compare the different structures with each other as well as with the experimental results a large RVE is created considering the total structure of the tested specimens. The line structure, the dotted diagonal pattern and the dotted horizontal pattern all have an austenite phase fraction around 7% and therefore can be compared to each other. The results of the simulations are shown in Figure 4.10 for both QM (a,c,e) and TM (b,d,f) patterned structures at a overall strain of 0.08.

- The strain partitioning of the line structure is almost identical for the quenched and tempered martensite. For the smaller simulations the strain does not partition within the austenite as it does in the experiments. However in these larger simulations including more grains it is observed that strain partitioning bands forming 45°from the tensile load in all directions. However, this is not limited by strain partitioning in the austenite. The stress partitioning is similar to the previous smaller scale. The stress partitions in the martensite and the austenite only contains small amounts of stress compared to the martensite. There is a large difference between the stress in QM and austenite. In TM large difference in stress exist as well but significantly less compared with the QM.
- The dotted diagonal pattern shows similar results as obtained in the smaller simulations. The austenite phase shows strain partitioning (around 0.24 strain in the dots of the QM) and the dots are diagonal interconnected with each other due to the strain partitioning within the martensite. The horizontal and vertical spaces between the dots contain the least amount of strain which is around the 0.02. The behaviour of the QM and the TM is similar. However, the QM has higher maximum strain values and lower minimum strain values. This is also observed for the smaller scale simulation. These observations support that more partitioning of strain takes place in the QM compared to the TM. Besides the strain partitioning between the dots, the diagonal strain partitioning observed in the martensite in the line structure also takes place however it is not as clear visible since it overlaps with the diagonal strain parti-

tioning of the austenitic dots. The stress partitions in the martensite hence low stress values are observed in the austenitic dots. The maximum stress values within the QM are considerably higher than in the TM whereas the stress values within the dots are somewhat lower.

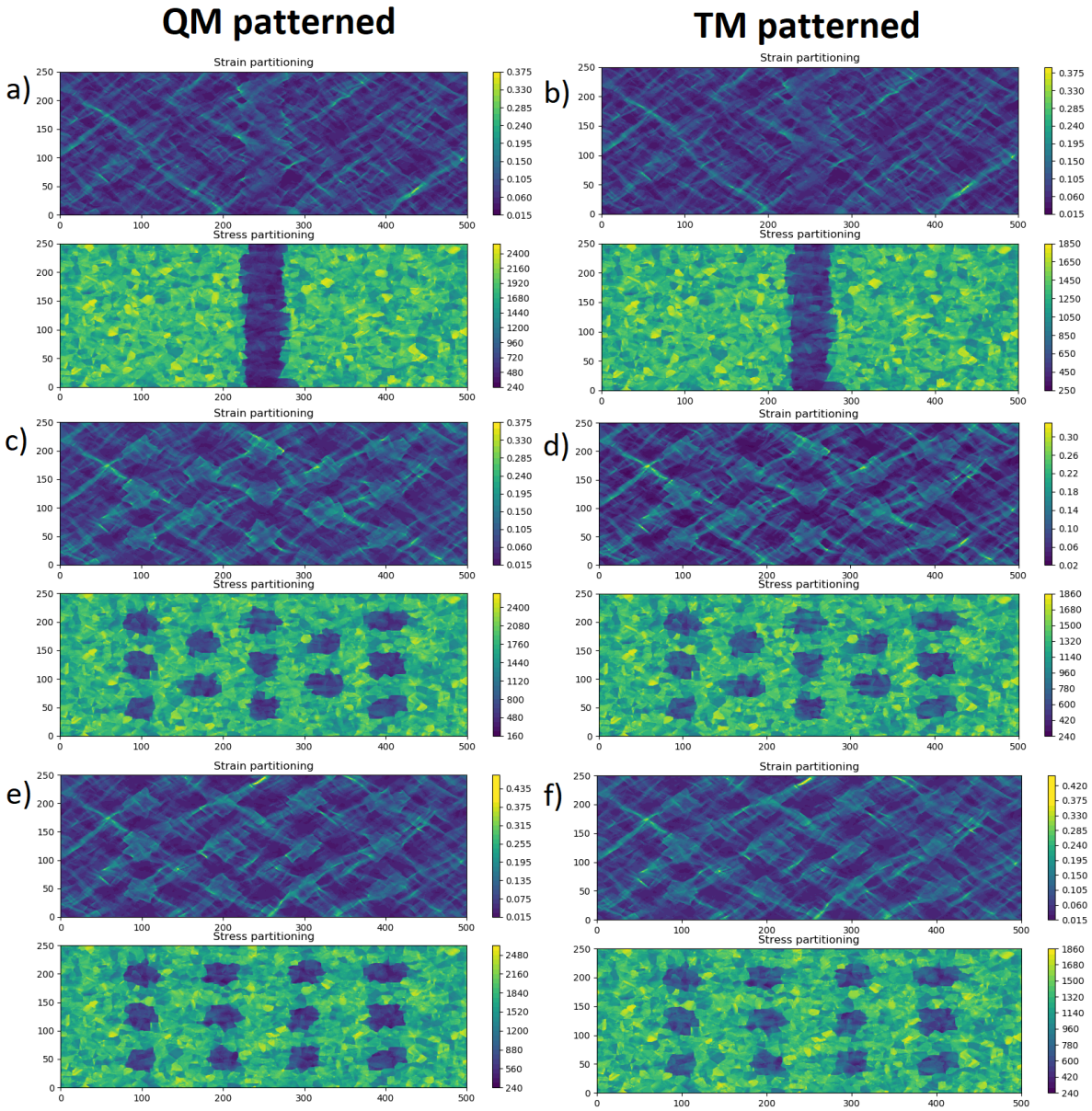


Figure 4.10: Stress and strain partitioning behaviour of QM (a,c,e) and TM (b,d,f) of the patterned line (a,b), dotted diagonal patter (c,d) and dotted horizontal pattern (e,f)

- For the dotted horizontal pattern the strain partitioning is very similar to the dotted diagonal pattern, with the following differences:
  - (i) The angle of the X structure for the strain partitioning is sharper since the dots which interconnect form a square instead of a rectangle and therefore are closer to one another

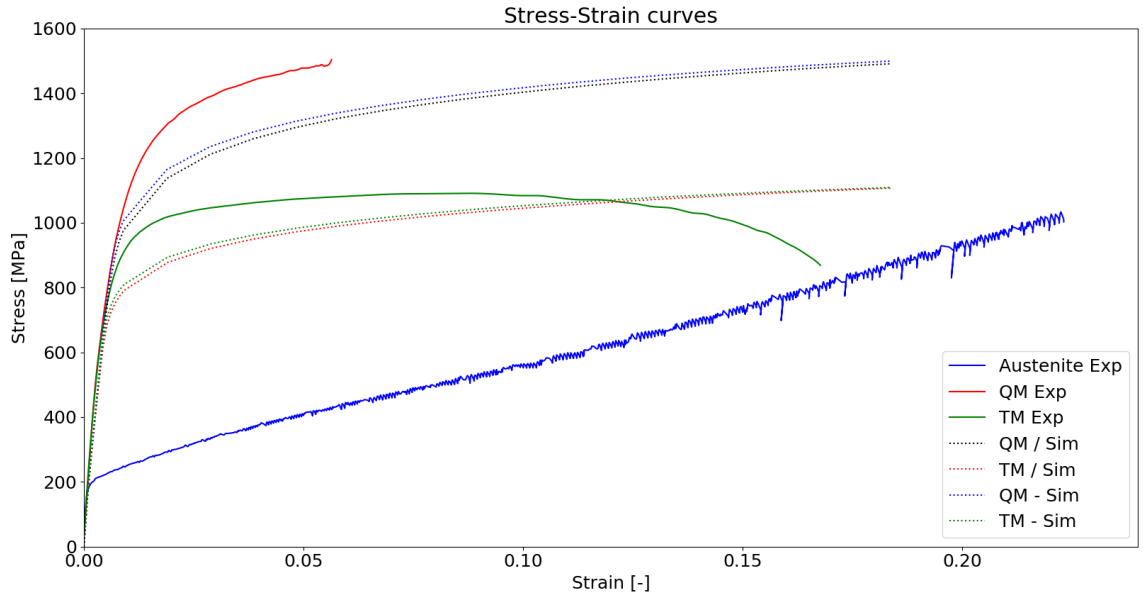


Figure 4.11: True Stress-True Strain curves from the simulated dotted diagonal and dotted horizontal patterns for both QM and TM along with the stress-strain curves of the base materials

- (ii) The maximum strain values are higher
- (iii) The maximum strain difference between QM and TM is lower

For the stress partitioning almost no difference is observed between all structures other than the difference in austenite structure. The maximum stress is somewhat higher for the dotted horizontal pattern compared to the dotted diagonal pattern but this difference is relatively small.

The strain partitioning behaviour of all the simulated structures is dominated by the strain partitioning band which have an angle of 45°. However with the created dot patterns the strain partitioning bands are slightly tilted to form connections between the austenite dots which do show strain partitioning on their own. Perpendicular to the tensile direction no strain partitioning bands are formed between the austenite dots. The structure obtain a rhombus shape of strain partitioning in which the martensite area in between only experience very low strains.

In Figure 4.11 the stress-strain curves of the simulated dotted diagonal pattern and the simulated dotted horizontal pattern of the large scale simulations are presented along with the stress-strain curves of the base materials. The patterns give similar stress-strain response with a small increase in strength for the dotted horizontal pattern for both the QM as TM case.

For both the QM and TM material a decrease in strength is observed as was expected considering the addition of a softer phase. It is not possible to say something about the possible increase in deformation since no failure mechanism is included in the simulation.

The strength of the DAMASK software lies in the use of the crystallographic orientation of the grains. However in this research a random texture was assumed for simulations. For future research it is advised that the texture of the material under investigation is experimentally analysed after which the results should be implemented in DAMASK for more realistic simulated behaviour. This implementation can be done using the DREAM.3D software.

5. Comparison between experimental and simulated results

The shortcoming of the simulations are based on the experimental observed results. Two main behaviours are compared: (i) the local deformation behaviour and (ii) the overall deformation behaviour. For the local deformation behaviour the DIC analysis from the experiments are compared to the strain partitioning in the simulation. The dotted diagonal patter TM/2 is chosen to be compared since both the simulation and the experiment have a strain of 0.039. In the overall deformation behaviour a stress-strain plot is made with both the simulated and experimental result for all cases.

5.1. Local deformation

A comparison between the local deformation behaviour of both (a) simulated and (b) experimental results are displayed in Figure 5.1. The most remarkable observations are:

- The simulation has distinct differences in strain between grains and orientation whereas for the experiments the austenite consist of much more grains and therefore do not show this behaviour. Hence the simulation show more local peaks of strain partitioning up to a strain of 0.168 whereas the maximum for strain partitioning in the experimental results are 0.108.

- Both the simulation and the experiments show strain partitioning of the austenite phase with quite similar magnitude.

- The strain partitioning bands in the martensite connecting the austenite dots diagonally are also both observed in the simulation and experiments. Almost exactly the same strain localization can be visualized.

- The horizontal strain partitioning between the austenite dots in the experiments clearly show that the dots are interconnected by horizontal strain partitioning, however in the simulations this behaviour is not experienced. The areas show almost zero strain in the simulation. A cause of this might be that a more Taylor based model [94, 95] is applied in the simulations compared to reality, hence neglecting the strain partitioning. However this is hypothetically and not yet confirmed, which could be investigated in further research.

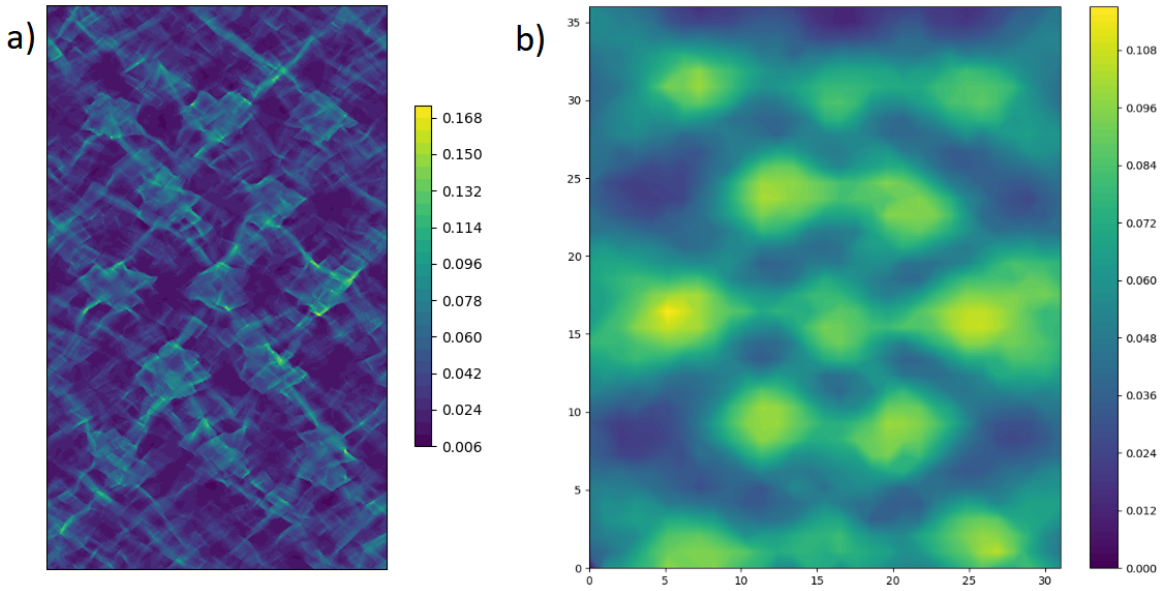


Figure 5.1: Comparison of local deformation behaviour of (a) the simulated and (b) DIC experimental results

Overall the simulation gives a good approximation of the localization of strain between the different structures. However, the difference between experiments and simulations are caused by the fact that the simulations are a simplified version of the experiments, hence the simulation comes with limitations:

- In the simulation the TRIP effect is only included by the extra hardening factor in the twinning parameters. This compensates for the overall behaviour in the stress strain curve, however this does not compensate with the deformation locally. Hence more strain in the austenite takes place in the experiments compared to the simulations which is confirmed by observations. As discussed in previous chapter the TRIP effect can only be included in the dislocation density constitutional laws in which only ϵ-martensite formation is included which only forms in high manganese steels.

- The difference between grains within the austenite is not included in the simulations. As shown experimentally the austenite shows different behaviour for recrystallized grains and displacive transformed grains. This distinction is not made in simulations. However these effects are not observed since the scale of the DIC analysis is much larger than the grain sizes of the material.

- The simulation uses the stress-strain curve of the initial austenite before the martensite formation. However the reversion of the austenite increases the dislocation density of the austenite significantly as explained earlier in this research. Hence the strain in this manner probably over-exaggerated compared to the experiments.

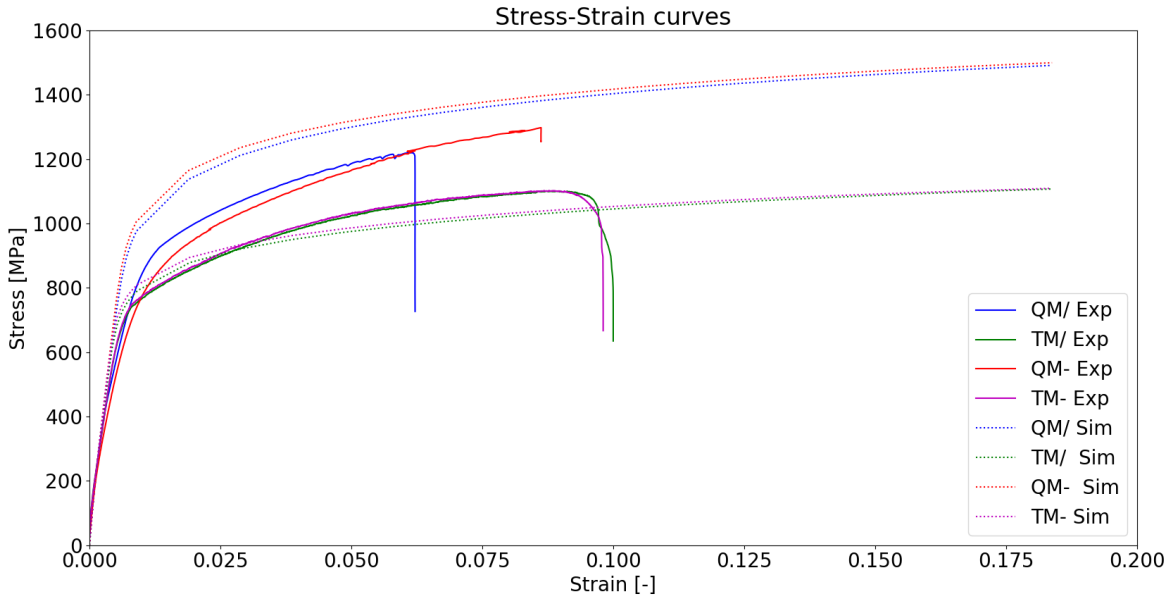


Figure 5.2: Comparison of the stress-strain curves of the experiments and simulations for both the dotted diagonal and dotted horizontal pattern of QM and TM

5.2. Overall deformation

The overall deformation of the simulation is compared to the experiments as well and is displayed in Figure 5.2. The most remarkable observation are:

- In all cases the strain hardening behaviour of the material is underestimated in the simulations. This can be explained by the TRIP-effect which is not included in the simulation since the TRIP-effect is known to increase the strain hardening of the material.

- The overestimation of the strength of the QM simulations. Even with lower strain hardening of the simulation, the strength at the strain to failure of the experimental results is much higher for the simulation.

- The underestimation of the strength in the simulation of the TM at the strain of fracture in the experiments while the yielding of the material is almost equal.

- For both the simulations and experiments the difference in stress-strain behaviour of the dotted diagonal pattern and the dotted horizontal pattern is very small.

The contradiction between overestimation for QM and underestimation for TM is remarkable. It is however difficult to compare the simulated curves with the experimental curves since the austenite fraction are not equal. In the simulation the austenite fraction is kept around 7% whereas for the experiments this is 17% considering the gauge length of 25 mm and the constant diameter of 2.9 mm of the austenite dots. In further research this should be considered more equal.

5.3. Conclusion

Simulations show good agreement with the local deformation behaviour of the different patterned structures. However, simulations do have limitations in its usability. The most important part of the simulation is the correctness of the material model and description of parameters in which considerable time and effort should be invested. Hence the simulations should be applied as tool to help determine which patterns show promising deformation behaviour and are interesting enough for further investigation by means of experiments. Nevertheless, simulations should not be used exclusively.

6. Conclusions and Outlook

This thesis investigated how the deformation behaviour of the a Fe-Ni-C steel can be tailored by the creation of patterned microstructures with the use of localized heat treatment. The deformation behaviour of architectured mircrostructures were investigated using both an experimental and computational approach. The architectured microstructure consists of a patterned austenite phase created by laser treatment in a cryogenically formed martensitic structure. Two main patterns are created: (i) a dotted diagonal pattern, and (ii) a dotted horizontal pattern which are both evaluated using QM and TM as base material. The main results of this investigation are summarized as followed:

- **Characterization of the microstructure of the laser treated specimen**
  The characterization of the created austenite structure showed that two main mechanisms took place upon transformation both experiencing different properties, (i) a displacive transformation which consist of larger austenite grains with relatively high hardness, and (ii) diffusional transformation which consist of smaller formed grains with relatively lower hardness due to recrystallization. The laser parameters used determine the dominant transformation mechanism which was the displacive transformation in this research.

- **The effect of the patterns on the strain partitioning behaviour in the material**
  The patterns created cause strain partitioning in the austenitic phase. These strains are considerably larger than in the martensite, however diagonal and horizontal strain partitioning bands form in the martensite interconnecting the austenite dots. This behaviour is thought to be caused by the maximum in-plane shear stress acting at 45°with respect to the tensile axis and due to strain compatibility causing the horizontal bands. Both the dotted diagonal pattern and the dotted horizontal pattern show similar behaviour.

- **The relation between the strain partitioning and the austenite to martensite mechanical induced transformation**
  The localized strain partitioning in the austenite caused the TRIP-effect to take place. Due to this effect significant hardening took place according to the microhardness values obtained. The martensite created by the TRIP effect is much harder due to the higher dislocation density and morphology. An exponentially decreasing relation was observed between the austenite fraction and the local strain in the austenite for both QM and TM patterned specimens.

- **The influence of the strength ratio between austenite and martensite on the deformation behaviour of the different patterns**
  Two strength ratios between austenite and martensite were obtained in QM and TM patterned specimens. Experiments showed that more strain partitioning took place

in the austenite in case of QM compared to the TM. This is thought to be caused by earlier yielding of the TM causing earlier stage three deformation. In the simulation this behaviour was not obtained and the strain partitioning was similar.

- **The effect of the patterns on the overall stress-strain response of the material**
  In the overall stress-strain response a decrease in strength is observed but instead the deformation is improved for both patterns in as-quenched martensite. For tempered martensite similar UTS is achieved but the specimens fail directly after the UTS, whereas for the base material a large necking region is present.
- **Comparison of the computationally obtained results with the experimental obtained results**
  In terms of local deformation behaviour the simulated results show good similarities with the experimental results, however the simulation has its limitations due to assumptions made as well as exclusion of certain phenomena such as the TRIP-effect. It therefore is advised that the simulation is applied as tool for determining patterns with promising deformation behaviour.

Bibliography

[1] E. Ma, T. Zhu, *Towards strength-ductility synergy through the design of heterogeneous nanostructures in metals*, materials today, volume 20, pp. 323-331, 2017

[2] X. Wu, Y. Zhu, *Heterogeneous materials: a new class of materials with unprecedented mechanical properties*, Material Research Letters, volume 5, pp. 527-532, 2017

[3] N. Fonstein, *Duel phase steels*, Automotive Steels: Design, Metallurgy, Processing and Applications, pp. 169-216, 2017

[4] M.J. Santofimia, S.M.C. van Bohemen, D.N. Hanlon, L. Zhao, J. Sietsma, *Perspectives in High-Strength Steels: Interaction Between Non-Equilibrium Phases*, Conference paper: International Symposium on New Developments in Advanced High-Strength Sheet Steels, 2013

[5] L. Wang, J.G. Speer, *Quenching and Partitioning Steel Heat Treatment*, Metallography, Microstructure and Analysis, volume 2, pp. 268-281, 2013

[6] M. Ashby, *Designing Architectured Materials*, Scripta Materialia, volume 68, pp. 4-7, 2013

[7] A.O. Andreev, M.P. Galkin, M.A. Libman, V.D. Mironov, V.N. Petrovskii, E.I. Estrin, *Use of Laser Heat Treatment for Creation Gradient Materials Based on the Fe-Cr-Ni System*, Metal Science and Heat Treatments, volume 56, pp. 53-56, 2014

[8] M.C. McGrath, D.C. van Aken, N.I. Medvedva, J.E. Medvedeva, *Work Hardening Behaviour in Steels with Multiple TRIP Mechanisms*, Metallurgical and Materials Transactions: A, volume 44, pp. 4634-4643, 2013

[9] C.J. Kuehmann, G.B. Olson, *Computational materials design and engineering*, Materials Science and Technology, volume 25, pp. 472-478, 2009

[10] D. Embury, O. Bouaziz, *Steel-Based Composites: Driving Forces and Classifications*, Annual Review of Materials Research, volume 40, pp. 213-241, 2010

[11] T. Koseki, J. Inoue, S. Nambu, *Development of Multilayer Steels for Improved Combinations of High Strength and High Ductility*, Materials Transactions, volume 55, pp. 227-237, 2013

[12] J.D. Verhoeven, A.H. Pendray, W.E. Dauksch, *The Key Role of Impurities in Ancient Damascus Steel Blades*, Journal of the Minerals, Metals & Meterials Society, volume 50, pp. 58-64, 1998

[13] J.D. Verhoeven, A.H. Pendray, W.E. Dauksch, S.R. Wagstaff *Damascus Steel Revisited*, Journal of the Minerals, Metals & Meterials Society, volume 70, pp. 1331-1336, 2018

[14] O. Bouaziz, Y. Brechet, D. Embury, *Heterogeneous and Architectured Materials: A Possible Strategy for Design of Structural Materials*, Advanced Engineering Materials, volume 10, pp. 24-36, 2008

[15] B. Chehab, H. Zurob, D. Embury, O. Bouaziz, Y. Brechet, *Compositionally Graded Steels: A Strategy for Materials Development*, Advanced Engineering Materials, volume 11, pp. 992-999, 2010

[16] R. Roumina, D. Embury, O. Bouaziz, H.S. Zurob, *Mechanical behaviour of a compositionally graded 300M steel*, Materials Science & Engineering: A, volume 578, pp. 140-149, 2013

[17] F. Lefevre-Schlick, O. Bouaziz, Y. Brechet, D. Embury, *Compositionally graded steels: The effect of partial decarburization on the mechanical properties of spherodite and pearlite*, Materials Science & Engineering: A, volume 491, pp. 80-87, 2008

[18] J. Kato, T. Kyoya, D. Yachi, K. Terada, *Topology optimization of micro-structure for composites applying a decoupling multi-scale analysis*, Structural and Multidisciplinary Optimization, volume 49, pp. 595-608, 2014

[19] Y. Dai, M. Feng, M. Zhao, *Topology optimization of laminated composite structures with design-dependant loads*, Composite Structures, volume 167, pp. 251-261, 2017

[20] N. de Kruijf, S. Zhou, Q. Li, Y.W. Mai, *Topology design of structures and composite materials with multiobjectives*, International Journal of Solids and Structures, volume 44, pp. 7092-7109, 2007

[21] B. Xu, X. Huang, S.W. Zhou, Y.M. Xie, *Concurrent topological design of composite thermoelastic macrostructure and microstructure with multi-phase material for maximum stiffness*, Composite Structures, volume 150, pp. 84-102, 2016

[22] X. Yan, X. Huang, Y. Zha, Y.M. Xie, *Concurrent topology optimization of structures and their composite microstructures*, Computers and Structures, volume 133, pp. 103-110, 2014

[23] J. Gao, H. Li, Z. Luo, P. Li, *Topology optimization of micro-structured materials featured with the specific mechanical properties*, Thesis at Huazhong University of Science, 2007

[24] Z. Jia, Y. Yu, L. Wang, *Learning from nature: Use material architecture to break the performance tradeoffs*, Materials and Design, volume 168, 107650, 2019

[25] B.S. Yilbas, S.Z. Shuja, *Laser Surface Processing and Model Studies*, Materials Forming Machining and Tribology, Springer, 2013

[26] W.M. Steen, J. Mazumder, *Laser Material Processing*, fourth edition, Springer, 2010

[27] E. Romer, *Modelling and control of laser surface treatment*, PhD thesis University of Twente, 1999

[28] J. Meijer, I. van Sprang, *Optimization of Laser Beam Transformation Hardening by One Single Parameter*, CIRP Annals, volume 40, pp. 183-186, 1991

[29] S. Vogt, A. Voll, S. Wollgarten, T. Freese, *Local laser softening of high-strength steel with an adapted intensity*, Journal of Laser Applications, volume 31, 012007, 2019

[30] M.J. Troughton, *Laser Welding*, Handbook of Plastic Joining, Second edition, pp. 81-95, 2009

[31] J. Mazumder, *Laser-aided direct metal deposition of metals and alloys*, Laser Additive Manufacturing, pp. 21-53, 2017

[32] I. Kozelkova, C. Dagbert, P. Gregoire, J. Galland, L. Hyspecka, *Kinetics of Austenite to Martensite Transformation in Iron-Nickel-Carbon Alloys During their Cooling or Tensile Testing*, Journal de Physique, volume 5,pp. 323-328, 1995

[33] H. Bhadeshia, R. Honeycombe, *Steels - Microstructure and Properties*, Elsevier, fourth edition, 2017

[34] A.A. Tiamiyu, S. Zhao, Z. Li, A.G. Odeshi, J.A. Szpunar, *Thermal and Mechanical Stability of Austenite in Metastable Austenitic Stainless Steel*, Metallurgical and Materials Transistions: A, volume 50, pp. 4513-4530, 2019

[35] K.R. Kinsman, J.G. Shyne, *Thermal stabilization of austenite in iron-nickel-carbon alloys*, Acta Metallurgica, volume 15, pp. 1527-1543, 1967

[36] V.A. Lobodyuk, E.I. Estrin, *Martensitic Transformations*, Cambridge International Science Publishing, 2014

[37] A. Weidner, *Deformation Processes in TRIP/TWIP Steels*, Springers Series in Material Science, volume 295, 2020

[38] I. Tamura, *Deformation-induced martensitic transformation and transformation-induced plasticity in steels*, Metal Science, volume 16, pp. 245-253, 1982

[39] H. Sato, S. Zaefferer, *A study on the formation mechanisms of butterfly-type martensite in Fe-30% Ni alloy using EBSD-based orientation microscopy*, Acta Materialia, volume 57, pp. 1931-1937, 2009

[40] H. Shirazi, G. Miyamoto, S.H. Nedjad, T. Chiba, M.N. Ahmadabadi, T. Furuhara, *Microstructure evolution during austenite reversion in Fe-Ni martensitic alloys*, Acta Materialia, vol. 144, pp. 269-280, 2018

[41] C.A. Apple, G. Krauss, *The Effect of Heating Rate on the Martensite to Austenite Transformation in Fe-Ni-C Alloys*, Acta Metallurgica, vol. 20, pp. 849-856, 1972

[42] Y.Y. Meshkov, E.V. Pereloma, *The effect of heating rate on reverse transformations in steels and Fe-Ni based alloys*, Phase Transformations in Steels, vol. 1, pp. 581-618, 2012

[43] V.V. Sagaradze, V.E. Danilchenko, Ph. L'Heritier, V.A. Shabashov, *The structure and properties of Fe-Ni alloys with a nanocrystalline austenite formed under different conditions of γ-α-γ transformations*, Materials Science and Engineering: A, vol. 337, pp. 146-159, 2002

[44] G. Krauss, *Fine Structure of Austenite Produced by the Reverse Martensitic Transformation*, Acta Metallurgica, vol. 11, pp. 499-509, 1963

[45] W. Bleck, X. Guo, Y. Ma, *The Trip Effect and its Application in Cold Formable Sheet Steels*, Steel Research International, vol. 88, Issue 10, 2017

[46] R. Rana, S.B. Singh, *Design, Metallurgy, Processing and Applications*, Automotive Steels, pp. 47-93, 2017

[47] D. de Kijf, C. Fojer, L. Kestens, R. Petrov, *Factors influencing the austenite stability during tensile testing of Q& P steel determined via in-situ EBSD*, Material Science and Engineering: A, vol. 638, pp. 219-227, 2015

[48] R. Wu, W. Li, C. Wang, Y. Xiao, L. Wang, X. Jin, *Stability of Retained Austenite Through a Combined Intercritical Annealing and Quenching and Partitioning (IAQP) Treatment*, Acta Metallurgica Sinica, vol. 28, pp. 386-393, 2015

[49] S. Lee, S. Lee, B. Cooman, *Austenite stability of ultrafine-grained transformation-induced plasticity steel with Mn partitioning*, Scripta Materialia, vol. 65, pp. 225-228, 2011

[50] J. Hidalgo, K.O. Findley, M.J. Santofimia, *Thermal and Mechanical stability of retained austenite surrounded by martensite with different degrees of tempering*, Materials Science and Engineering: A, vol. 690, pp. 337-347, 2017

[51] X.C. Xiong, B. Cheng, M.X. Huang, J.F. Wang, L. Wang, *The effect of morphology on the stability of retained austenite in a Q& P steel*, Scripta Materialia, vol. 68, pp. 321-324, 2013

[52] I.B. Timokhina, P.D. Hodgson, E.V. Pereloma, *Effect of microstructure on the stability of retained austenite in TRIP steels*, Metallurgical and Materials Transactions: A, vol. 35, pp. 2331-2341, 2004

[53] W.S. Li, H.Y. Gao, H. Nakashima, S. Hata, *In-situ study of the deformation-induced rotation and transformation of retained austenite in a low-carbon steel treated by the Q& P process*, Materials Science and Engineering: A, vol. 649, pp. 417-425, 2015

[54] R. Lehnert, A. Weidner, H. Biermann, *Martensite formation during tensile deformation at high-alloy TRIP steel after Q& P route investigated by DIC*, Materialia, vol. 8, 2019

[55] N.H. van Dijk, A.M. Butt, L. Zhao, J. Sietsma, S.E. Offerman, J.P. Wright, S. van der Zwaag, *Thermal stability of retained austenite in TRIP steels studied by synchrotron X-ray diffraction during cooling*, Acta Materialia, vol. 53, pp. 5439-5447, 2005

[56] J.G. Speer, Li Wang, *Quenching and Partitioning Steel Heat Treatment*, Metallography, Microstructure and Analysis, vol. 2, pp. 268-281, 2013

[57] M.J. Santofimia, J.G. Speer, A.J. Clarke, L. Zhao, J. Sietsma, *Influence of interface mobility on the evolution of austenite–martensite grain assemblies during annealing*, Acta Materialia, vol. 57, pp. 4548-4557, 2009

[58] E.O. Hall, W. Sylwestrowicz, *The Deformation and Ageing of Mild Steel*, Proceedings of the Physical Society, volume 64, pp. 495-502, 1951

[59] N.J. Petch, *The cleavage strength of polycrystals*, Iron steel institute, volume 64, pp. 747-753, 1953

[60] C.Y. Wang, J.Shi, W.Q. Cao, H. Dong, *Characterization of microstructure obtained by quenching and partitioning process in low alloy martensitic steel*, Materials Science and Engineering: A, vol. 527, pp. 3442-3449, 2010

[61] P.J. Jacques, J. Ladriere, F. Delannay, *On the Influence of Interactions between Phases on the Mechanical Stability of Retained Austenite in Transformation-Induced Plasticity Multiphase Steels*, Metallurgical and Materials Transactions: A, vol. 32, pp. 2759-2768, 2010

[62] G. Boa, J.W. Hutchinson, R.M McMeeking, *The flow stress of dual-phase, non-hardening solids*, Mechanics of Materials, vol. 12, pp. 85-94, 1991

[63] G. Krauss, *Steels: Processing, Structure, and Performance*, ASM International, second edition, pp. 373-398, 2015

[64] G. Krauss, *Tempering of martensite in carbon steel*, Phase Transformations in Steels, volume 2, pp. 126-150, 2012

[65] L.E. Samuels, *Tempering of martensite*, Metallography, Microstructure and Analysis: Application and Innovation for Metals, Alloys and Engineered Materials, volume 3, pp. 70-90, 2014

[66] K.A. Taylor, G.B. Olson, M. Cohen, J.B. van der Sande, *Carbide Precipitation during Stage I Tempering of Fe-Ni-C Martensite*, Metallurgical Transactions: A, volume 20, pp. 2749-2765, 1989

[67] B. Kim, J. Sietsma, M.J. Santofimia, *Thermodynamic aspects of carbon redistribution during ageing and tempering of Fe-Ni-C alloys*, Philosophical magazine, volume 96, pp. 2632-2648, 2016

[68] F.Roters, P. Eisenlohr, L. Hantcherli, D.D. Tjahjanto, T.R. Bieler, D. Raabe, *Overview of constituative laws, kinematics, homogenization and multiscale methods in crystal plasticity finite-element modeling: Theory, experiments, applications*, Acta Materialia, volume 58, pp. 1152-1211, 2010

[69] D. Raabe, *Deformation Processing*, Encyclopaedia of Condensed Matter Physics, pp. 387-395, 2005

[70] J.H. Yoon, H. Huh, Y.S. Lee, *Finite Element Analysis of Polycrystalline Deformation wiht the Rate-dependent Crystal Plasticity*, AIP Conference Proceedings, volume 908, 2007

[71] B. Mohammed, T. Park, F. Pourboghrat, J. Hu, R. Esmaeilpour, F.A. Farha, *Multiscale crystal plasticity modeling of multiphase advanced high strength steel*, International Journal of Solids and Structures, volume 151, pp. 57-75, 2018

[72] J.O. Andersson, T. Helander, L. Hoglund, P. Shi, B. Sundman, *Thermo-Calc & DICTRA, computational tool for material science*, Calphad, volume 26, pp. 273-312, 2002

[73] Sente Software Ltd., *JMatPro4.0 [Computer software]*, 2001

[74] S.R. Kalidindi, A. Abusafieh, E. El-Danaf, *Accurate Characterization of Machine Compliance for Simple Compression Testing*, Experimental Mechanics, volume 37, pp. 210-215, 1997

[75] E.B. Dolan, S.W. Verbruggen, R.A. Rolfe, *Techniques for studying mechanobiology*, Mechanobiology in Health and Disease, pp. 1-53, 2018

[76] R.E. Chinn, *Etching*, Metallography, Microstructure and Analysis, volume 4, pp. 240-257, 2015

[77] R.E. Smallman, A.H.W. Ngan, *Characterization and Analysis*, Modern Physical Metallurgy, Eighth edition, 2014

[78] G. Hai, *Butterfly martensite in industrial steels*, Metallography, volume 20, pp. 263-275, 1987

[79] D.R. Poirier, G.H. Geiger, *Transport Phenomena in Materials Processing*, The Minerals, Metals & Materials Series, Springer, 2016

[80] H.J. Breukelman, *Architectured Microstructures: The effect of localized lasser heat treatment on the microstructure of a FeCNi steel*, Thesis, 2019

[81] J.D. Verhoeven, *Fundamentals of Physical Metallurgy*, John Wiley & Sons, 1975

[82] S. Graca, R. Colaco, P.A. Carvalho, R. Vilar, *Determination of dislocation density from hardness measurements in metals*, Materials Letters, volume 62, pp. 3812-3814, 2008

[83] P.R. Rios, F. Siciliano, H.R.Z. Sandim, R.L. Plaut, A.F. Padilha, *Nucleation and Growth During Recrystallization*, Materials Research, volume 8, pp. 225-238, 2005

[84] M. Huang, C. Xu, G. Fan, E. Maawad, W. Gan, L. Geng. F. Lin, G. Tang, *Role of layered strucutre in ductility improvement of layered Ti-Al metal composite*, Acta Materialia, volume 153, pp. 235-249, 2018

[85] A. Alaei, H. Jafarian, A.R. Eivani, *Observation austenite memory and significant enhancement of tensile properties during cyclic reverse martensite transformation in a Fe-Ni-C TRIP steel*, Materials Science & Engineering: A, volume 676, pp. 342-350, 2016

[86] S.W. Ooi. A.A. Shirzadi, J. Yang, *Austenite Memory and Variant Selection in a Noval Martensitic Welding Alloy*, Materials today: Proceedings, volume 2, pp. 325-331, 2015

[87] S.H. Talebi, M. Jahazi, H. Melkonyan, *Retained Austenite Decomposition and Carbide Precipitation during Isothermal Tempering of a Medium-Carbon Low-Alloy Bainitic Steel*, Materials, volume 11, 1441, 2018

[88] M. Park, M.S. Kang, G.W. Park, E.Y. Choi, H.C. Kim, H.S. Moon, *The Effects of Recrystallization on Strength and Impact Toughness of Cold-Worked High-Mn Austenite Steels*, Metals, volume 9, pp. 948-962, 2019

[89] A. Dutta, D. Ponge, S. Sandlobes, D. Raabe, *Strain partitioining and strain localization in medium manganese steels measured by in situ microscopic digital image correlation*, Materialia, volume 5, 100252, 2019

[90] S. Lee, B.C. de Cooman, W. Woo, *Analysis of the Tensile Behavior of 12 pct Mn Multiphase TWIP + TRIP Steel by Neutron Diffraction*, Metallurgical and Material Transactions: A, volume 47, pp. 2125-2140, 2016

[91] Y.H. Yan, *Strain-Hardening behaviours of TRIP-assisted steels during plastic deformation*, Materials Science and Engineering: A, volume 479, pp. 333-338, 2008

[92] R.J.H. Jolly, D.J. Sanderson, *A Mohr Circle construction for the opening of a pre-existing fracture*, Journal of Structural Geology, volume 19, pp. 887-892, 1997

[93] L. Patriarca, M. Filippini, S. Beretta, *Digital image correlation-based analysis of strain accumulation on a duplex γ-TiAl*, Intermetallics, volume 75, pp. 42-50, 2016

[94] W. Mao, *Intergranular mechanical equilibrium during the rolling deformation of polycrystalline metals based on Taylor principles*, Materials Science and Engineering: A, volume 672, pp. 129-134, 2016

[95] W. Mao, *On the Taylor principle for plastic deformation of polycrystalline metals*, Frontiers of Materials Science, volume 10, pp. 335-345, 2016

[96] B. Edenhofer, D. Joritz, M. Rink, K. Voges, *Carburizing of steels*, Thermochemical Surface Engineering of Steels, pp. 485-553, 2015

[97] C.C. Casero, J. Sietsma, M.J. Santofimia, *The role of the austenite grain size in the martensitic transformation in low carbon steels*, Materials & Design, volume 167, 107625, 2019

[98] H. Sato, S. Zaefferer, *A study of the formation mechanism of butterfly-type martensite in Fe-30% Ni alloy using EBSD-based orientation microscopy*, Acta Materialia, volume 57, pp. 1931-1937, 2009

[99] E.J. Seo, L. Cho, Y. Estrin, B.C. de Cooman, *Microstructure-mechanical properties relationships for quenching and partitioning processed steel*, Acta Materialia, volume 113, pp. 124-139, 2016

[100] E. de Moor, S. Lacroix, A.J. Clarke, J. Penning, J.G. Speer, *Effect of Retained Austenite Stabilized via Quench and Partitioning on the Strain Hardening of Martensitic Steels*, Metallurgical and Materials Transactions: A, volume 39, pp. 2586-2595, 2008

[101] P. Moore, G. Booth, *Failure modes and analysis in metals*, The Welding Engineering's Guide to Fracture and Fatigue, pp. 95-110, 2015

[102] H. Sheikh, R. Ebrahimi, E. Bagherpour, *Crystal plasticity finite element modelling of crystallographic textures in simple shear extrusion process*, Materials & Design, volume 109, pp. 289-299, 2016

[103] F. Roters, P. Eisenlohr, L. Hantcherli, D.D. Tjahjanto, T.R. Bieler, D. Raabe, *Overview of constitutive laws, kinematics homogenization and multiscale methods in crystal plasticity finite-element modelling: Theory,experiments, applications*, Acta Materialia, volume 58, pp. 1152-1211, 2010

[104] D. Kim, J. Kim, W. Park, Y. Lee, Y. Im ,Y. Lee, *Three-dimensional crystal plasticity finite element analysis of microstructure and texture evolution during channel die compression of IF steel*, Computational Materials Science, volume 100, pp. 52-60, 2015

[105] B. Mohammed, T. Park, F. Pourboghrat, J. Hu, R. Esmaeilpour, F. Farha, *Multiscale crystal plasticity modeling of multiphase advance high strength steel*, International Journal of Solids and Structures, vol. 151, pp. 57-75, 2018

[106] F. Roters et al, *DAMASK - The Dusseldorf Advanced Material Simulation Kit for modelling multi-physics crystal plasticity, thermal, and damage phenomena from the single crystal up to the component scale*, Computational Materials Science, vol. 158, pp. 420-478, 2019

[107] M.A. Groeber, M.A. Jackson, *DREAM.3D: A Digital Representation Environment for the Analysis of Microstructure in 3D*, Integrating Materials and Manufacturing Innovation, vol. 3, pp. 56-72, 2014

[108] T. Kanit, S. Forest, I. Galliet, V. Mounoury, D. Jeulin, *Determination of the size of the representative volume element for random composites: statistical and numerical approach*, International Journal of Solids and Structures, vol. 40, pp. 3647-3679, 2003

[109] J. Ahrens, B. Geveci, C. Law, *Paraview: An End-User Tool for Large Data Visualization*, Visualization Handbook, Elsevier, 2005

[110] D.D. Tjahjanto, P. Eisenlohr, F. Roters, *A noval grain cluster-based homogenization scheme*, Modelling and Simulations in Materials Science and Engineering, volume 18, 015006 , 2010

[111] P. Eisenlohr, M. Diehl, R.A. Lebensohn, F. Roters, *A spectral method solution to crystal elasto-viscoplasticity at finite strains*, International Journal of Plasticity, volume 46, pp. 37-53, 2013

[112] T. Wu, J.L. Bassani, C. Laird, *Latent hardening in single crystals - I. Theory and experiments*, Proceedings of the Royal Society A, 1991

[113] C.R. Weinberger, B.L. Boyce, C.C. Battaile, *Slip planes in bcc transition metals*, Institute of Materials,k Minerals and Mining and ASM International, volume 58, pp. 296-314, 2013

[114] A.G. Jackson, *Slip systems*, Handbook of Crystallography, Springer New York, pp. 83-88, 1991

[115] M. Niewczas, *Dislocations and Twinning in Face Centred Cubic Crystals*, Dislocations in Solids, volume 13, pp. 263-364, 2007

[116] D.E. Diesburg, *The elastic constants of Fe-Ni-C alloys*, Iowa State University repository, 1971

[117] P. Arasaratnam, K.S. Sivakumaran, M.J. Tait, *True Stress-True Strain Models for Structural Steel Elements*, ISRN Civil Engineering, 2011

[118] C. Song, H. Yu, J. Lu, T. Zhou, S. Yang, *Stress partitioning among ferrite, martensite and retained austenite of a TRIP-assisted multiphase steel: An in-situ high-energy X-ray diffraction study*, Materials Science & Engineering: A, volume 726, pp. 1-9, 2018

[119] Z.H. Cong, N. Jia, X. Sun, Y. Ren, J.Almer, Y.D. Wang, *Stress and Strain Partitioning of Ferrite and Martensite during Deformation*, Metallurgical and Materials Transactions: A, volume 40, pp. 1383-1387, 2009

[120] A.K. Rana, S.K. Paul, P.P. Dey, *Effect of Martensite Volume Fraction on Strain Partitioning Behaviour of Dual Phase Steel*, Physical Mesomehcanics, volume 21, pp. 333-340, 2018

[121] S. Kuang, Y. Kang, H. Yu, R. Liu, *Stress-strain partitioning of constituent phases in dual phase steel based on the modified law of mixture*, International Journal of Minerals, Metallurgy and Materials, volume 16, pp. 393-398, 2009

[122] Y.K. Lee, C.S. Choi, *Driving Force for $\gamma - \epsilon$ Martensitic Transformation and Stacking Fault Energy of γ in Fe-Mn Binary System*, Metallurgical and Material Transactions: A, volume 31, pp. 355-360, 2000

[123] D.P. Escobar, S.S.F. Dafe, D.B. Santos, *Martensite reversion and texture formation in 17Mn-0.06C TRIP/TWIP steel after hot cold rolling and annealing*, Journal of Material Reserach and Technology, volume 4, pp. 162-170, 2015

[124] D.Q. Xun, W.A. Dong, C.X. Nong, L.X. Min, *Stacking Fault energy of cryogenic austenitic steels*, Chinese Physics, volume 11, pp. 596-600, 2002

[125] T. Maiti, P. Eisenlohr, *Fourier-based spectral method solution to finite strain crystal plasticity with free surfaces*, Scripta Materialia, volume 145, pp. 37-40, 2018

[126] D. Hull, D.J. Bacon, *Introduction to Dislocations*, Elsevier, Fifth edition, 2011

Appendices

A. DIC result of the specimens

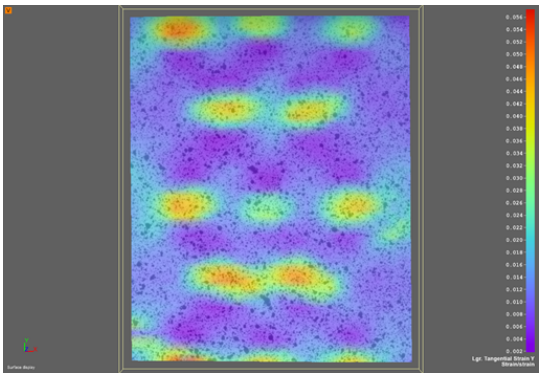


Figure A.1: DIC results QM/1

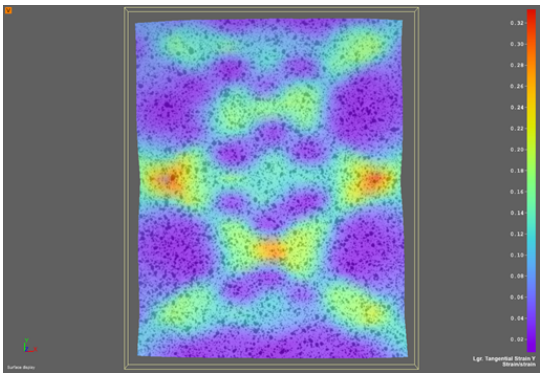


Figure A.2: DIC results QM/2

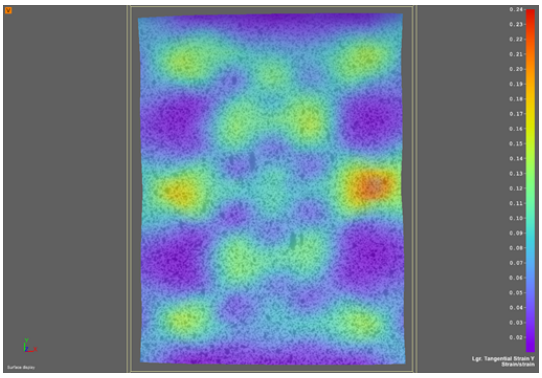


Figure A.3: DIC results QM/3

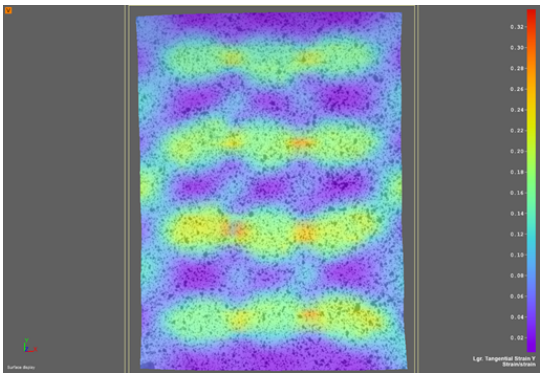


Figure A.4: DIC results QM-1

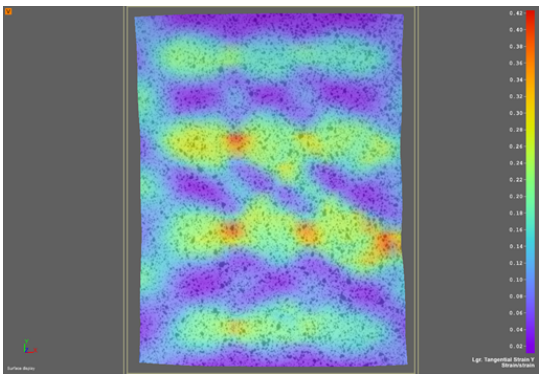


Figure A.5: DIC results QM-2

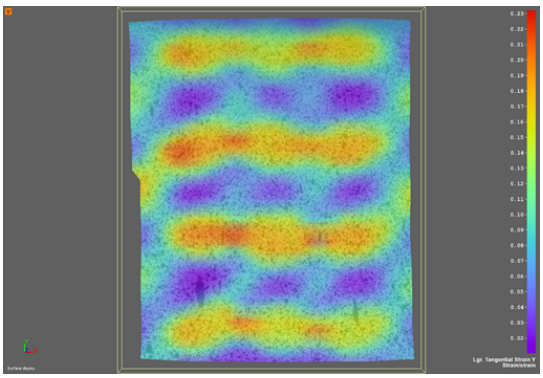


Figure A.6: DIC results QM-3

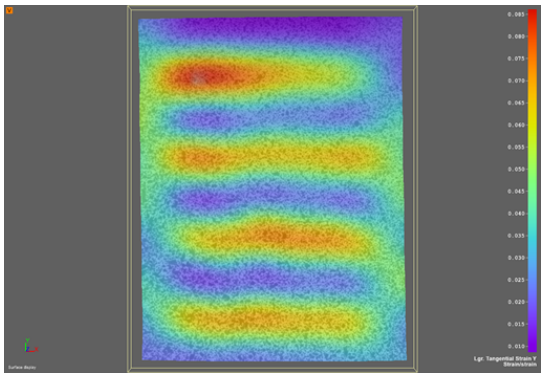


Figure A.7: DIC results QM-4

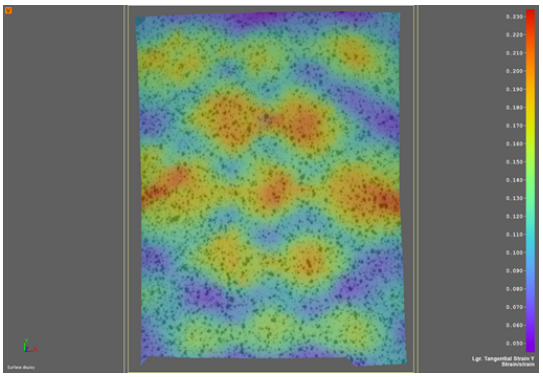


Figure A.8: DIC results TM/1

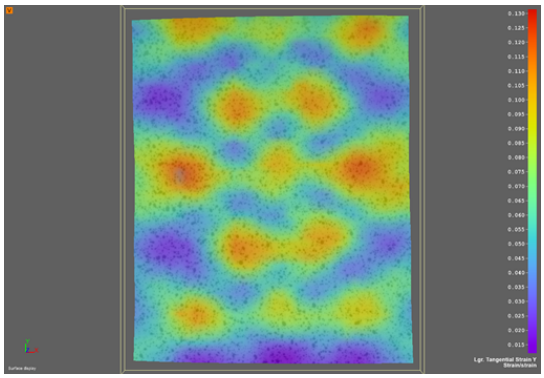


Figure A.9: DIC results TM/2

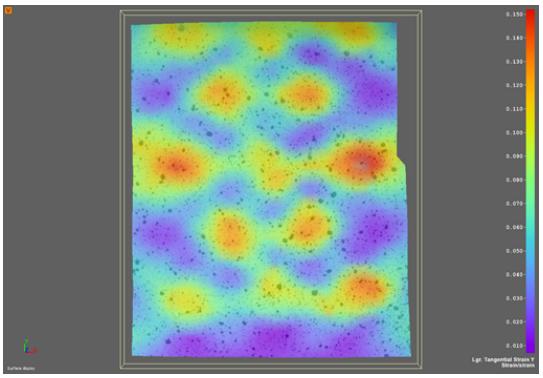


Figure A.10: DIC results TM/3

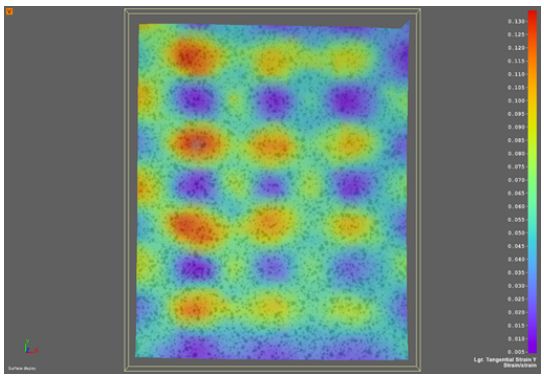


Figure A.11: DIC results TM-1

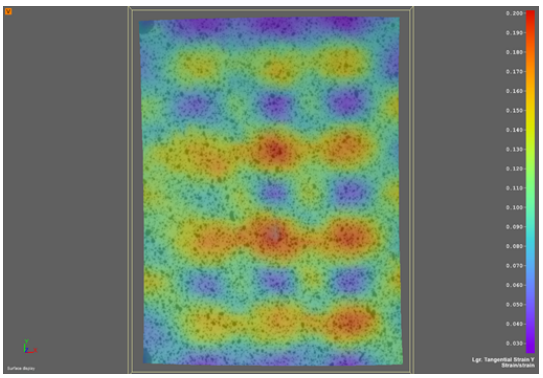


Figure A.12: DIC results TM-2

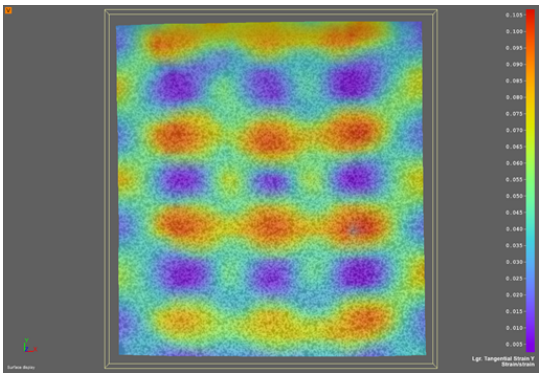


Figure A.13: DIC results TM-3

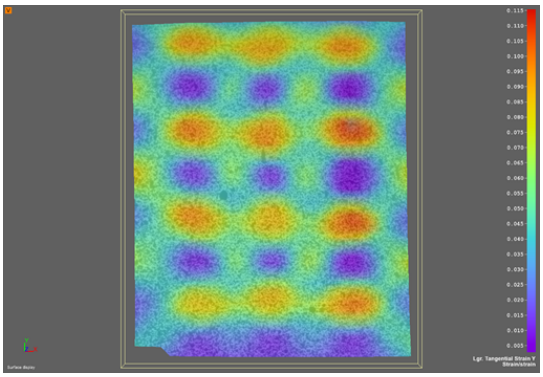


Figure A.14: DIC results TM-4

B. Tensile test results of the specimens

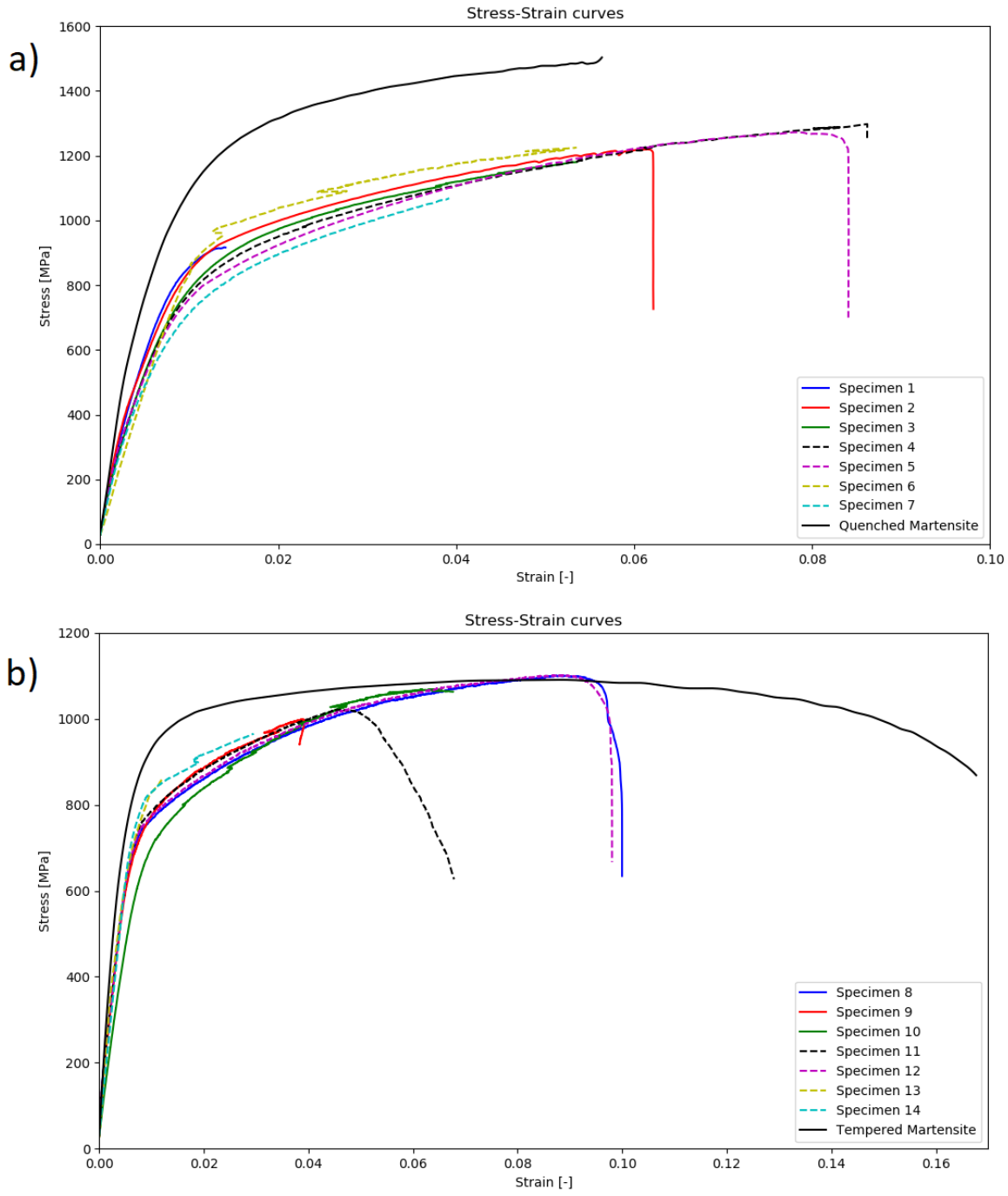


Figure B.1: Tensile curves of all specimens